



Virginia Commonwealth University  
VCU Scholars Compass

---

Theses and Dissertations

Graduate School


---

2015

## Electronic Principles Governing the Stability and Reactivity of Ligated Metal and Silicon Encapsulated Transition Metal Clusters

Marissa B. Abreu  
*Virginia Commonwealth University*

Follow this and additional works at: <https://scholarscompass.vcu.edu/etd>

 Part of the [Other Chemistry Commons](#)

© The Author

---

Downloaded from

<https://scholarscompass.vcu.edu/etd/3732>

This Dissertation is brought to you for free and open access by the Graduate School at VCU Scholars Compass. It has been accepted for inclusion in Theses and Dissertations by an authorized administrator of VCU Scholars Compass. For more information, please contact [libcompass@vcu.edu](mailto:libcompass@vcu.edu).

© Marissa Baddick Abreu 2015  
All Rights Reserved

# **Electronic Principles Governing the Stability and Reactivity of Ligated Metal and Silicon Encapsulated Transition Metal Clusters**

A dissertation submitted in partial fulfillment of the requirements for the  
degree of Doctor of Philosophy in Chemistry  
at Virginia Commonwealth University

by

Marissa Baddick Abreu

B.A. in Mathematics, Minor in Chemistry  
East Stroudsburg University of Pennsylvania, 2010

Director: Shiv N. Khanna  
Commonwealth Professor, Department of Physics

Virginia Commonwealth University  
Richmond, Virginia  
January, 2015

# Table of Contents

**List of Figures** **v**

**List of Tables** **viii**

**Abstract** **ix**

## **1 Introduction**

**1.1 The Journey to Cluster-Assembled Materials** ..... **1**

**1.2 Ligated Metal Clusters: Iodine-Protected Aluminum**..... **6**

1.2.1 Motivation ..... 6

1.2.2 The CNFEG Model ..... 7

1.2.3 Superatoms ..... 12

1.2.4 Extension of the CNFEG Model to Ligand-Protected Systems ..... 15

1.2.5 Reactivity of CNFEG Clusters ..... 16

1.2.6 Purpose of the Present Study ..... 20

**1.3 Silicon Encapsulated Transition Metal Clusters** ..... **21**

1.3.1 Motivation ..... 21

1.3.2 Is CrSi<sub>12</sub> a Magic Cluster? ..... 23

1.3.3	The 18-Electron Rule.....	27
1.3.4	Application of the CNFEG Model .....	30
1.3.5	Crystal-Field Splitting and Jahn-Teller Distortion.....	31
1.3.6	Purpose of the Present Study.....	33
<b>1.4</b>	<b>Organization of This Thesis .....</b>	<b>35</b>
 <b>2 Methods</b>		
<b>2.1</b>	<b>Overview.....</b>	<b>36</b>
<b>2.2</b>	<b>Density Functional Theory.....</b>	<b>36</b>
2.2.1	The Electron Density .....	36
2.2.2	The Hohenberg-Kohn Theorems.....	37
2.2.3	The Kohn-Sham Equations.....	39
2.2.4	Exchange-Correlation Functionals .....	41
<b>2.3</b>	<b>Computational Methods .....</b>	<b>42</b>
2.3.1	Ligated Metal Clusters: $Al_nI_m^-$ .....	42
2.3.2	Silicon Encapsulated Transition Metal Clusters: $CrSi_n$ and $WSi_n$ .....	43
 <b>3 Ligated Metal Clusters</b>		
<b>3.1</b>	<b>Overview.....</b>	<b>44</b>
<b>3.2</b>	<b>Determining the Reaction Pathways of <math>Al_nI_m^-</math> with Methanol.....</b>	<b>45</b>
<b>3.3</b>	<b>The <math>Al_{13}I_x^-</math> (<math>x=0 - 4</math>) Series .....</b>	<b>49</b>

3.4	The $\text{Al}_{14}\text{I}_y^-$ ( $y=0-5$ ) Series.....	57
3.5	Discussion .....	64
3.6	Experimental Confirmation .....	65
<b>4</b>	<b>Silicon Encapsulated Transition Metal Clusters</b>	
4.1	Overview.....	67
4.2	Choosing a Functional .....	67
4.3	Calculating Cluster Properties .....	75
4.4	$\text{CrSi}_n$ ( $n=6-16$ ) .....	77
4.4.1	Energetics.....	77
4.4.2	Molecular Orbital Analysis.....	81
4.5	$\text{WSi}_n$ ( $n=6-16$ ).....	87
4.5.1	Energetics.....	87
4.5.2	Molecular Orbital Analysis.....	92
4.6	Discussion .....	93
<b>5</b>	<b>Conclusions</b>	<b>95</b>
	<b>Appendix A</b>	<b>100</b>
	<b>Appendix B</b>	<b>103</b>
	<b>References</b>	<b>120</b>

## List of Figures

Figure 1.1.1: Band Gap Tuning in $As_7$ -Alkali Cluster-Assembled Materials.....	3
Figure 1.2.1: Mass Spectra of Sodium Clusters.....	7
Figure 1.2.2: Electron Filling Order in Atoms and Clusters .....	9
Figure 1.2.3: Electronic energy levels and corresponding molecular orbitals of $Al_{13}^-$ .....	13
Figure 1.2.4: Mass Spectra of $Al_nI_m^-$ Clusters and Reaction with Oxygen.....	18
Figure 1.2.5: Complementary Active Sites on $Al_{12}^-$ Break the O-H Bond in Water.....	20
Figure 1.3.1: Time-resolved mass spectra of $WSi_nH_x^+$ .....	23
Figure 1.3.2: Relative Abundances of $WSi_nH_x^-$ ( $n=1-12$ ; $x=0, 2, 4$ ).....	24
Figure 1.3.3: Geometry of $WSi_{12}$ .....	25
Figure 1.3.4: The Energy Levels and Molecular Orbitals of $Cr(CO)_6$ .....	27
Figure 1.3.5: Crystal-Field Splitting of d-orbitals for Several Symmetries.....	31
Figure 1.3.6: Crystal-Field Splitting in $Al_{22}Cu^-$ .....	32
Figure 1.3.7: Lowest Unoccupied Molecular Orbital of $CrSi_{12}$ .....	34
Figure 3.3.1: Ground State Structures and Frontier Orbital Charge Densities of the $Al_{13}I_x^-$ ( $x=0-4$ ) Series.....	50
Figure 3.3.2: Lowest Energy Reaction Pathways of $Al_{13}^-$ and $Al_{13}I^-$ with Methanol .....	54
Figure 3.3.3: Lowest Energy Reaction Pathways of Two Isomers of $Al_{13}I_2^-$ with Methanol .	55
Figure 3.4.1: Ground State Structures and Frontier Orbital Charge Densities of $Al_{14}I_y^-$ .....	57
Figure 3.4.2: Reaction Pathways of $Al_{14}I_3^-$ with Methanol.....	61
Figure 3.4.3: Selected Reaction Pathways of $Al_{14}^-$ and $Al_{14}I^-$ .....	63

Figure 3.6.1: Mass spectra of $Al_nI_x^-$ before and after reaction with methanol .....	66
Figure 4.2.1: Photoelectron Spectra of $CrSi_n^-$ (n=3-12) .....	69
Figure 4.2.2: PBE Ground States and Low-Lying Isomers of $CrSi_n^-$ .....	70
Figure 4.2.3: B3LYP Ground States and Low-Lying Isomers of $CrSi_n^-$ .....	71
Figure 4.2.4: PBE Simulated Photoelectron Spectra for $CrSi_n^-$ (n=6-12).....	73
Figure 4.2.5: B3LYP Simulated Photoelectron Spectra for $CrSi_n^-$ (n=6-12) .....	74
Figure 4.4.1: Ground State Geometries of Neutral $CrSi_n$ (n=6-16) Clusters.....	78
Figure 4.4.2: Energetic Properties of Ground State $CrSi_n$ (n=6-16) Clusters .....	79
Figure 4.4.3: $CrSi_{12}$ Orbital Energy Levels and Selected Orbitals .....	82
Figure 4.4.4: $CrSi_{14}$ Orbital Energy Levels and Selected Orbitals .....	84
Figure 4.4.5: The 3d-Bands of $CrSi_n$ .....	86
Figure 4.5.1: Ground State Structures of $WSi_n$ (n=6-16) .....	88
Figure 4.5.2: Energetic Properties of $WSi_n$ (n=6-16) Ground States.....	89
Figure 4.5.3: The 5d-Bands of $WSi_n$ .....	93
Figure A-1: Lowest Energy Reaction Pathways of $Al_{13}I_3^-$ and $Al_{13}I_4^-$ with Methanol.....	100
Figure A-2: Lowest Energy Reaction Pathways of $Al_{14}I_2^-$ , $Al_{14}I_4^-$ , and $Al_{14}I_5^-$ with Methanol .....	102
Figure B-1: Higher Energy Isomers of $CrSi_n$ (n=6-9) .....	103
Figure B-2: Higher Energy Isomers of $CrSi_n$ (n=10-12) .....	104
Figure B-3: Higher Energy Isomers of $CrSi_{13}$ and $CrSi_{14}$ .....	105
Figure B-4: Higher Energy Isomers of $CrSi_{15}$ and $CrSi_{16}$ .....	106
Figure B-5: Ground State Geometries of Pure Silicon Clusters .....	107
Figure B-6: $CrSi_n$ Cation Ground States .....	107



Figure B-7: Hydrogen Bound $\text{CrSi}_n$ Ground States .....	108
Figure B-8: Occupied Molecular Orbitals of $\text{CrSi}_{12}$ (1) .....	109
Figure B-9: Occupied Molecular Orbitals of $\text{CrSi}_{12}$ (2) .....	110
Figure B-10: Unoccupied Molecular Orbitals of $\text{CrSi}_{12}$ .....	111
Figure B-11: Occupied Molecular Orbitals of $\text{CrSi}_{14}$ (1) .....	112
Figure B-12: Occupied Molecular Orbitals of $\text{CrSi}_{14}$ (2) .....	113
Figure B-13: Unoccupied Molecular Orbitals of $\text{CrSi}_{14}$ .....	114
Figure B-14: Higher Energy Isomers of $\text{WSi}_n$ (n=6-11) .....	115
Figure B-15: Higher Energy Isomers of $\text{WSi}_n$ (n=12, 13) .....	116
Figure B-16: Higher Energy Isomers of $\text{WSi}_n$ (n=14-16) .....	117
Figure B-17: Anionic Ground States of $\text{WSi}_n$ (n=6-16) .....	118
Figure B-18: Ground State Structures of $\text{WSi}_n$ (n=6-16) Cations .....	118
Figure B-19: Lowest-Energy Hydrogen-Bound $\text{WSi}_n$ (n=6-16) Clusters .....	119

## List of Tables

Table 3.3-1: Reaction Sites and Corresponding Binding Energies for $\text{Al}_{13}\text{I}_x^-$ .....	51
Table 3.3-2: Relative Energies for Reaction Pathways of $\text{Al}_{13}\text{I}_x^-$ with Methanol.....	53
Table 3.4-1: Reaction Sites and Corresponding Binding Energies for $\text{Al}_{14}\text{I}_y^-$ .....	59
Table 3.4-2: Relative Energies for Reaction Pathways of $\text{Al}_{14}\text{I}_y^-$ with Methanol.....	60
Table 4.2-1: VDE, ADE, and Relative Position of the 2 <sup>nd</sup> Peak of Theoretical and Experimental Photoelectron Spectra for $\text{CrSi}_n^-$ (6-12).....	75
Table A-1: Orbitals Used in Plotting the Frontier Orbital Density of $\text{Al}_{13}\text{I}_x^-$ (x=0-4).....	100
Table A-2: Orbitals used in Plotting the Frontier Orbital Density of $\text{Al}_{14}\text{I}_y^-$ (y=0-5).....	101
Table B-1: Calculated Properties of $\text{CrSi}_n$ (n=6-16).....	108
Table B-2: Calculated Properties of $\text{WSi}_n$ (n=6-16).....	119

# Abstract

## ELECTRONIC PRINCIPLES GOVERNING THE STABILITY AND REACTIVITY OF LIGATED METAL AND SILICON ENCAPSULATED TRANSITION METAL CLUSTERS

By Marissa Baddick Abreu, Ph.D.

A dissertation submitted in partial fulfillment of the requirements for the degree of Doctor of Philosophy in Chemistry at Virginia Commonwealth University.

Virginia Commonwealth University, 2015

Major Director: Dr. Shiv N. Khanna, Commonwealth Professor, Department of Physics

A thorough understanding of the underlying electronic principles guiding the stability and reactivity of clusters has direct implications for the identification of stable clusters for incorporation into clusters-assembled materials with tunable properties. This work explores the electronic principles governing the stability and reactivity of two types of clusters: ligated metal clusters and silicon encapsulated transition metal clusters. In the first case, the reactivity of iodine-protected aluminum clusters,  $Al_{13}I_x^-$  ( $x=0-4$ ) and  $Al_{14}I_y^-$  ( $y=0-5$ ), with the protic species methanol was studied. The symmetrical ground states of  $Al_{13}I_x^-$  showed no reactivity with methanol but reactivity was achieved in a higher energy isomer of  $Al_{13}I_2^-$  with iodines on adjacent aluminum atoms – complementary Lewis acid-base active sites were induced on the opposite side of the cluster capable of breaking the O-H bond in methanol.  $Al_{14}I_y^-$  ( $y=2-5$ ) react with methanol, but only at the ligated adatom site. Reaction of methanol with  $Al_{14}^-$  and  $Al_{14}I^-$  showed that ligation of the adatom was necessary for the reaction to occur there – revealing the concept of a ligand-activated adatom. In the second case, the study focused heavily on  $CrSi_{12}$ , a silicon encapsulated transition metal cluster whose stability and the reason for that stability has been debated heavily in the literature. Calculations of the energetic properties of  $CrSi_n$  ( $n=6-16$ )

revealed both  $\text{CrSi}_{12}$  and  $\text{CrSi}_{14}$  to have enhanced stability relative to other clusters; however  $\text{CrSi}_{12}$  lacks all the traditional markers of a magic cluster. Molecular orbital analysis of each of these clusters showed the CNFEG model to be inadequate in describing their stability. Because the  $3d_{z^2}$  orbital of Cr is unfilled in  $\text{CrSi}_{12}$ , this cluster has only 16 effective valence electrons, meaning that the 18-electron rule is not applicable. The moderate stability of  $\text{CrSi}_{12}$  can be accounted for by the crystal-field splitting of the 3d orbitals, which pushes the  $3d_{z^2}$  orbital up in energy.  $\text{CrSi}_{14}$ , on the other hand, has 18 effective valence electrons on Cr, minimal 3d-orbital splitting, and does follow the 18-electron rule. A repetition of these calculations with  $\text{WSi}_n$  ( $n=6-16$ ) showed similar results, except  $\text{WSi}_{12}$  shows all the markers of a magic cluster, due to the greater crystal-field splitting of 5d orbitals.

# 1 Introduction

## 1.1 The Journey to Cluster-Assembled Materials

Well-designed studies of clusters consisting of a few to a few thousand atoms offer the practical opportunity to model complex phenomena, such as catalytic activity, doping in semiconductors, and behavior at surfaces. Within this small size regime, however, something even more interesting occurs: electronic, magnetic, and chemical properties can be fundamentally different from those of the bulk phase of the comprising element. Aluminum behaves as a monovalent atom in homogeneous clusters containing less than seven atoms, while it is trivalent in the bulk.<sup>1</sup> Large magnetic moments have been theoretically predicted and experimentally confirmed in clusters of the 4d transition metal rhodium, which is non-magnetic on a macroscopic scale.<sup>2,3</sup> The type of magnetism can also change; manganese, which has two antiferromagnetic bulk phases, becomes ferromagnetic on the size scale of two to eight atoms.<sup>4,5</sup> Clusters of the noble metal gold have been shown to catalyze the combustion of carbon monoxide,<sup>6</sup> while, on the other hand, clusters of readily oxidized aluminum show stability to oxygen at certain cluster sizes.<sup>7-9</sup>

Unique properties arise in clusters due to the phenomenon of quantum confinement.<sup>10</sup> Because of the small size of clusters, the potential well confining the electrons has a much smaller volume than in macroscopic solids. As a consequence of this, the electronic states are grouped into shells, similar to atoms, rather than in continuous bands as in an extended system. Another, more physical, way of accounting for the difference between clusters and their bulk counterparts is considering that because of their small size, a greater fraction of the atoms of a cluster are exposed to the surface than in a macroscopic species.<sup>11</sup> This argument has, for

example, been used to predict and explain the aforementioned giant magnetic moments in rhodium, and magnetic properties in other clusters.<sup>2,12</sup>

Another important difference in the behavior of clusters when compared to bulk systems is that the properties can vary dramatically with size. Adding or removing even a single atom from a cluster can significantly change its electronic, magnetic, or reactive properties. Returning to our previous examples, we can see how a cluster's properties depend heavily on the number of atoms comprising it. The valency of aluminum changes from one to three on going from six atoms to seven atoms.<sup>1</sup> Certain rhodium clusters, notably Rh<sub>12</sub>, Rh<sub>13</sub>, Rh<sub>15</sub>, Rh<sub>16</sub>, and Rh<sub>19</sub>, have higher magnetic moments than their neighbors.<sup>2</sup> Catalytic activity of size-selected gold clusters begins at Au<sub>8</sub>.<sup>6</sup> Al<sub>13</sub><sup>-</sup> is stable to reaction with oxygen, while Al<sub>12</sub><sup>-</sup>, just one atom smaller, reacts away.<sup>7-9</sup> Because of the unique and size-selective characteristics of clusters, and the ability to control their size and composition one atom at a time, there exists the exciting potential of synthesizing new materials with tailored properties if clusters, instead of atoms, can serve as their building blocks.<sup>10,13-17</sup>

The realization of cluster-assembled materials (CAMs) has been a major motivation in the study of clusters for the past two decades. Many such materials have already been theoretically predicted and/or experimentally made. The famous buckminsterfullerene, C<sub>60</sub>, a very stable cluster due to aromaticity, has been doped with alkali metal atoms to form alkali fullerides, many with superconducting properties.<sup>18-23</sup> Gadolinium-doped fullerenes have been developed that are useful in magnetic resonance imaging (MRI) technology.<sup>24</sup> In addition to metal doping, C<sub>60</sub> lends itself to easy external functionalization, allowing its chemistry to be modified.<sup>22</sup> The success of fullerene-based materials serves as a model for CAMs – proof that it can be done. Metallic clusters also have their place in the world of cluster-assembled materials. Ionic compounds of

$\text{Al}_{13}$ , which has halogen-like properties, and alkali atoms have been a topic of much theoretical study.<sup>16,17,25–31</sup> For example, it has been theorized that in combination with  $\text{Na}_3\text{O}$  or  $\text{K}_3\text{O}$ , which behave as alkali metals,  $\text{Al}_{13}$  forms ionic compounds,  $(\text{Na}_3\text{OAl}_{13})_n$  and  $(\text{K}_3\text{OAl}_{13})_n$ , with very high binding energies.<sup>31</sup>

Another pair of clusters,  $\text{As}_7$  and  $\text{As}_{11}$ , has been found to form stable complexes with alkali atoms as well, and various alkali compounds of  $\text{As}_7$  have been successfully experimentally synthesized into extended materials.<sup>32,33</sup> These clusters also serve as an example of the ways in which the properties of a cluster-assembled material can be modified by changing its composition; in this case the band gap varies depending on the alkali atom choice. In Figure 1.1.1, three observed structures of alkali metal and  $\text{As}_7$  cluster assemblies are shown.

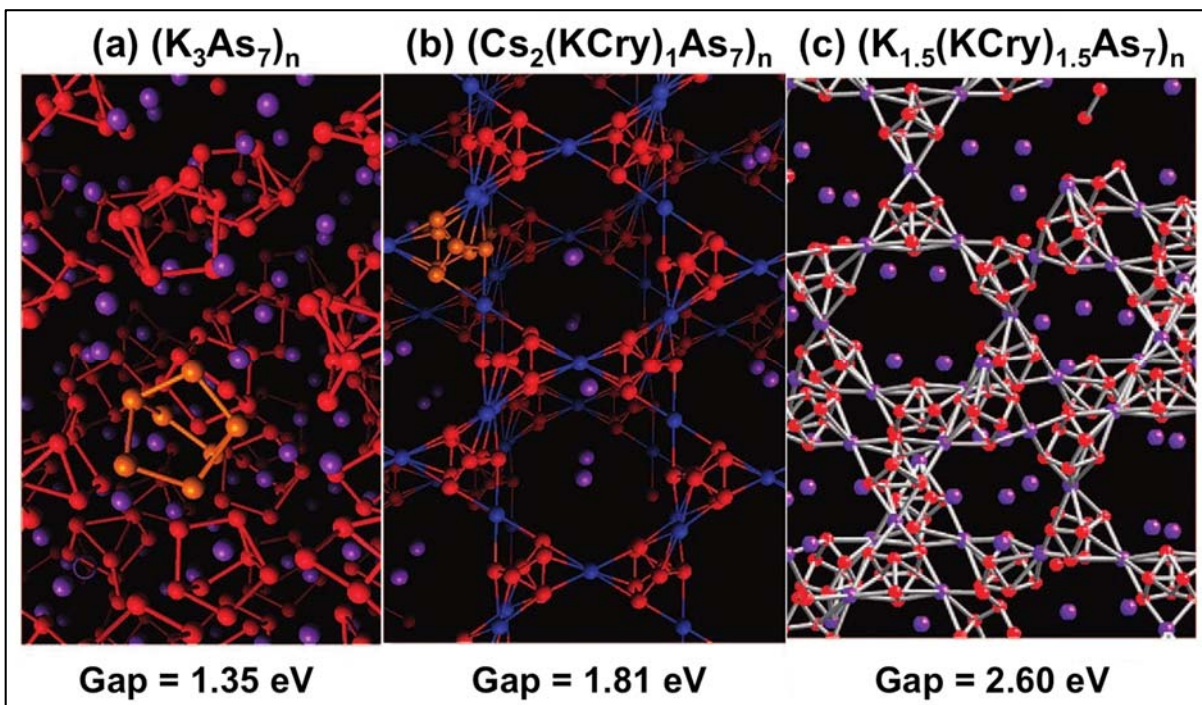


**Figure 1.1.1: Band Gap Tuning in  $\text{As}_7$ -Alkali Cluster-Assembled Materials.** Changes in the alkali metal bonding with  $\text{As}_7$ <sup>3-</sup> results in changes in the band gap of the solid. Shown above are CAMs made of  $\text{As}_7$  and (a) potassium and cryptated potassium, (b) cesium and potassium, and (c) all potassium. Arsenic is shown in red, with one cluster highlighted in orange in (b) and (c), potassium is shown in purple, and cesium is shown in dark blue. The cryptand in (a) is not shown for clarity. Figure taken from Castleman, Jr. and Khanna.<sup>34</sup>

In these ionic compounds, the  $As_7$  cluster will gain three electrons to become  $As_7^{3-}$ , so each cluster-assembled material requires a ratio of three alkali atoms to every one  $As_7$  cluster. Note that cryptated potassium, abbreviated KCry in Figure 1.1.1, is potassium chelated by a large polydentate organic ligand. Crypt-222, the common name for 4,7,13,16,21,24-Hexaoxa-1,10-diazabicyclo[8.8.8]hexacosane, is often used. Cryptation of the alkali metal reduces the ionization potential of the metal, making electron transfer from the metal atom to the cluster easier, and thereby facilitating cluster assembly. In Figure 1.1.1(a), no cryptated potassium atoms are used, and the band gap is 1.35 eV. Substituting two cesium atoms for two of the potassium atoms, and a cryptated-potassium for the remaining potassium atom, gives a cluster assembly shown in Figure 1.1.1(b) with a higher band gap of 1.81 eV. The highest band gap, 2.60 eV, results using a 1:1 mixture of potassium and cryptated-potassium, as shown in Figure 1.1.1(c). This family of materials serves as a powerful example of the ways in which materials with tunable properties are achievable through the use of clusters as building blocks.

As the first step towards the goal of CAMs, identifying clusters with unique and potentially useful properties has been a priority. Interesting properties, however, are not the only requirement for a cluster to eventually become a part of a cluster-assembled material. On the whole, clusters are metastable; when brought into close proximity with each other they will coalesce, and the sought after unique properties will vanish.<sup>35</sup> The use of clusters so stable they do not interact is, of course, one method of tackling this issue –  $C_{60}$  is such a cluster. Individually stable clusters will have low cohesive energies, so the task of using them involves not only identifying clusters with great stability, but ways of combining or linking them that will hold the clusters together without eliminating the individual clusters' properties. The incorporation of  $Al_{13}$  and  $As_7$  into alkali complexes is an example. Other methods involve passivating the cluster



in some way: embedding of clusters in zeolite cages, adsorbing clusters on surfaces, or adding ligands to stabilize clusters. This raises the need to understand the chemistry of interaction between the cluster and the stabilizing agents, and the ways in which that will affect the properties of the material.<sup>34</sup> Whether using inherently stable clusters, or adjusting clusters with stabilizing agents, a thorough understanding of the underlying electronic and chemical principles guiding the stability and reactivity of interesting clusters is required for the accurate prediction of stable and appropriate clusters and the rational design and synthesis of cluster-assembled materials.

Just as in conventional chemistry, several models have been developed to explain the stability and reactivity of cluster systems. A complete coverage of all the electronic structure and other guiding principles currently used in cluster science is beyond the scope of this thesis. Rather, I will explore these concepts by considering those theories relevant to the two example systems of study: aluminum clusters with iodine ligands and silicon encapsulated transition metal clusters. The confined nearly free electron gas (CNFEG) model (also known as the jellium model), a centerpiece of cluster science, describes the electronic structure of simple metal clusters well and has been successfully extended to some ligated systems. Aluminum clusters in particular exemplify the CNFEG model, being simple metallic clusters with relatively spherical geometries. Reactivity with protic species in these clusters depends on Lewis acid and base active sites, and for ligated clusters such as  $Al_nI_m^-$ , the interaction of ligands with the cluster is important. On the other hand, the electronic principles governing the stability of silicon encapsulated transition metal clusters are not fully understood or agreed upon. Due to the presence of a metal atom, the CNFEG model has sometimes been invoked, either for the entire cluster, or only for the metal atom, with the silicon atoms considered to be ligands simply

donating charge. The presence of a transition metal atom implies concepts familiar from traditional coordination chemistry, such as the 18-electron rule and crystal-field splitting. In the following two sections, I will review the electronic principles currently used to describe these two types of clusters and relevant previous work, both theoretical and experimental.

## **1.2 Ligated Metal Clusters: Iodine-Protected Aluminum**

### **1.2.1 Motivation**

Aluminum is of interest as a high energy density material. Other elements with higher energy densities include beryllium, which is toxic, and boron, which is also well studied in pure and mixed clusters, but exhibits unusual bonding patterns due to having only three electrons. Clusters of aluminum, on the other hand, were quickly found to adhere to predictions based on the CNFEG model, which will be discussed in detail in the next section. The small size of aluminum atoms has also made it incredibly amenable to theoretical treatment; clusters of larger metals are generally more computationally expensive to study due to the number of electrons and the possible necessity of adding spin-orbit coupling and relativistic effects. As a result, there is a wide body of literature, both experimental and theoretical, discussing the stability and reactivity of aluminum clusters.<sup>7–9,36–40</sup>

As mentioned above, the addition of ligands to metal clusters has served as a means of stabilizing clusters by protecting the metal atoms from reaction with surrounding species. The ligand can also exchange charge with the cluster, making it more stable and promoting formation of assemblies. An understanding of ligand-metal bonding is thus imperative to the design of materials using ligand-protected clusters. Synthesis of such CAMs also requires knowledge of the effects ligands have on metal cluster reactivity in different environments – this is not only important in developing experimental protocols for making CAMs, but also has implications for

the utility of such a material. Studying the reactivity of ligated metal clusters also has significance in catalysis, as active sites can be isolated and the mechanisms of reaction revealed. The addition of halogen atoms to aluminum clusters has been previously studied, and iodine was found to form the most stable halogenated aluminum complexes, making iodine a logical choice for the exploration of ligand effects on aluminum cluster reactivity.

### 1.2.2 The Confined Nearly Free Electron Gas Model

Much of the early work in cluster science sought to explain the abundance spectra of various clusters. Of these early studies, the experimental observation of “magic” numbers - cluster sizes with relatively intense peaks - in the mass spectra of sodium clusters by Knight et al., and the subsequent analysis, shaped the future of the field.<sup>41</sup>

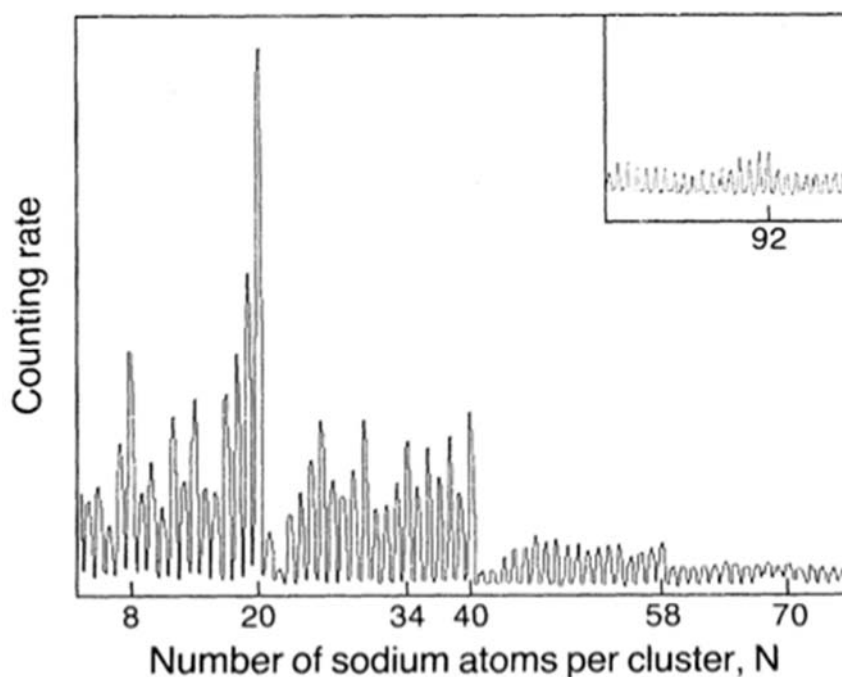


**Figure 1.2.1: Mass Spectra of Sodium Clusters.** The above figure shows the abundance spectra taken from Knight et al.<sup>41</sup> Counting rate, or intensity, is in arbitrary units. The inset figure shows the mass spectra of higher clusters. The magic numbers of atoms are indicated on the x-axis.

As shown in Figure 1.2.1 above, sodium clusters with 2, 8, 20, 40, 58, and 92 sodium atoms exhibited relatively larger peaks in the mass spectra than other cluster sizes, and an abrupt decrease in intensity followed. Both factors indicated enhanced stability for these cluster sizes, which Knight et al. viewed as a reflection of the electronic structure. Applying the nearly free electron concept of bulk metallic bonding, the lone 3s valence electrons were considered to form a nearly free electron gas against a background potential - the spherical jellium background potential as proposed by Ekardt.<sup>42</sup> The ionic cores of each atom in the cluster, which include the nuclei and non-valence electrons, contribute to the jellium potential, with their positive charge smeared uniformly across the cluster. This led to the “jellium” or confined nearly free electron gas (CNFEG) model applied to metallic clusters.

Solving the Schrödinger equation under the conditions described above yields discrete energy levels,  $N=1, 2, 3\dots$  with angular momentum  $L=0, 1, 2, 3\dots$ . The electron filling order is given by  $1S^2, 1P^6, 1D^{10}, 2S^2, 1F^{14}, 2P^6, 1G^{18}, 2D^{10}, 3S^2, 1H^{22}$ , etc. Note that the potential in a cluster is considered constant throughout the entire cluster, and only begins to drop off at the surface of the cluster, in contrast to an atom, for which the potential immediately begins to drop off as one leaves the nucleus. There are three possible radial potentials to describe a confined nearly free electron gas: a 3D harmonic potential, a 3D square well potential, and the Woods-Saxon potential. The last of these is the most commonly used for the empirical CNFEG model. Because of the differing potentials, clusters and atoms yield different results for the radial portion of the solution to the Schrödinger equation, and thus the solution for clusters generally follows the nuclear convention rather than the atomic convention.<sup>41-43</sup> The orbital levels and electron configurations are shown for several atoms and clusters in Figure 1.2.2 below.

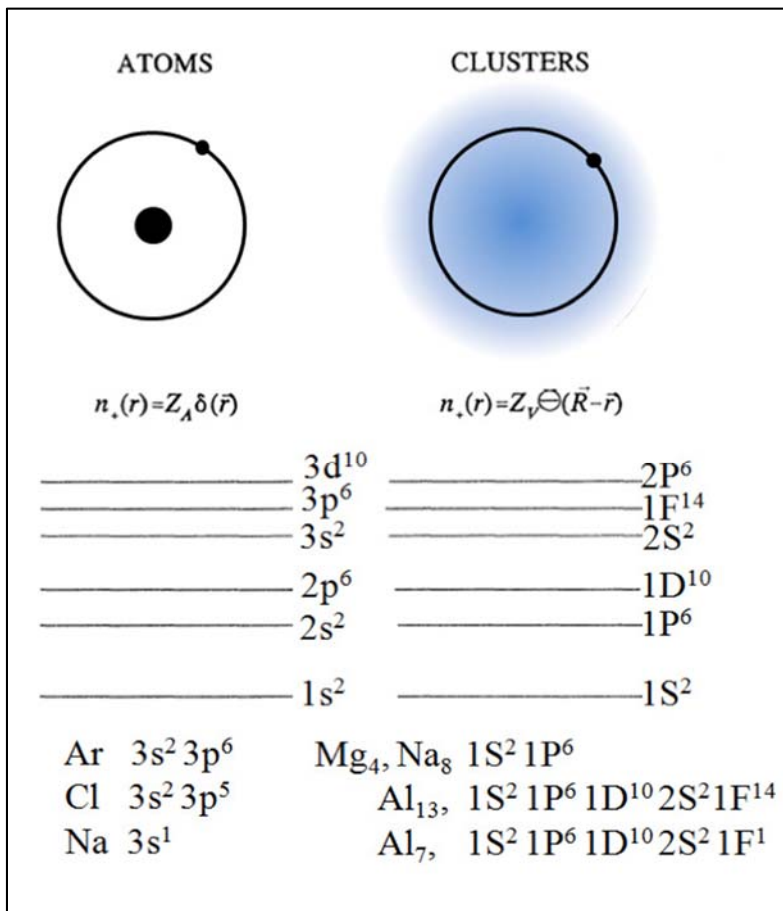


**Figure 1.2.2: Electron Filling Order in Atoms and Clusters.** The first six energy levels and their designations are shown for an atom and a cluster. Electron configurations are also given for the atoms Argon, Chlorine, and Sodium, and their isovalent cluster respective counterparts  $Mg_4$  and  $Na_8$ ,  $Al_{13}$ , and  $Al_7$ .

While not consistently done in the literature, CNFEG orbital letters will be capitalized within this thesis to distinguish them from atomic orbitals. In this shell closure model, frequently referred to as the spherical CNFEG model, magic clusters have a number of valence electrons corresponding to a major electronic shell closing, just as in atoms and in nuclei.<sup>41,43</sup>

While the spherical CNFEG model helped to explain the major peaks in the abundance spectra of sodium clusters, it did not adequately explain the weaker peaks at theoretically predicted magic numbers 18, 34, 68, and 70, nor the fine structure of the mass spectrum - the moderately intense peaks at 12, 14, 26, 30, 36, 38, 50, and 54.<sup>41</sup> The Jahn-Teller effect,<sup>44</sup> which

states that the geometry of molecules with spatially degenerate ground states will distort, offered a reasonable explanation for both inadequacies. Clusters with valence electron counts that do not correspond to a major shell closing will not be spherically symmetric. Rather, these clusters will have an oblate or prolate geometry, that is, a geometry compressed or elongated along the z-axis, respectively. To account for this, Clemenger introduced the ellipsoidal CNFEG model<sup>45</sup> by adapting a similar concept by Nilsson<sup>46</sup> for nuclei, in which the potential is allowed to relax away from spherical symmetry. This modification correctly predicted the small peaks observed in the sodium cluster mass spectrum, and the weaker intensity of the peaks 18, 34, 68, and 70 compared to the prediction of the spherical model.<sup>43,45,47</sup> The spheroidal CNFEG model combines the spherical and ellipsoidal models, allowing the background CNFEG potential to take the shape of the cluster, whether that be perfectly spherical or distorted.<sup>47</sup>

The CNFEG model provided a theoretical and conceptual explanation for the abundance spectra of not only sodium clusters, but also potassium,<sup>48</sup> aluminum,<sup>7</sup> copper, silver, and gold<sup>49</sup> clusters, and has since been expanded to include most metallic clusters in which the electrons are delocalized. Aside from mass spectral data, the CNFEG model helped to explain discontinuities in other experimentally measured properties such as ionization potential (IP), electron affinity (EA), and polarizability. The IP and EA can take on two forms: vertical and adiabatic. The adiabatic ionization potential (AIP) is equal to the difference in energy of the neutral and cationic species in their respective ground states, while the vertical ionization potential (VIP) is equal to the difference in energy between the neutral species in its ground state and the cationic species in the geometry of the neutral. Similarly, the adiabatic electron affinity (AEA) is the difference in energy of the neutral and anionic species in their respective ground states, and the vertical electron affinity (VEA) is the difference in energy between the neutral species in its ground state

and the anionic species in the geometry of the neutral. Related to the electron affinities are the electron detachment energies. The adiabatic detachment energy (ADE) is identical to the AEA, while the vertical detachment energy is the difference in energy between the anion in its ground state and the neutral species in the anionic geometry. The ADE and VDE are measured experimentally using photoelectron spectroscopy, a method often employed in cluster studies. In the resulting spectra, the VDE shows up as the first peak, indicating the energy it takes to remove an electron from the cluster with no geometry change, and the ADE shows up as the initial rise in the photoelectron spectra. Finally, polarizability is the ease of distorting a cluster's electron cloud.

In general, cluster sizes corresponding to magic numbers of valence electrons show higher ionization potentials and lower electron affinities, detachment energies, and polarizabilities than open-shelled neighbors.<sup>47</sup> This provided further evidence supporting the idea that these cluster sizes were stable due to electronic shell closures; it takes a greater amount of energy to remove an electron from a closed-shell species than from an open-shell species. Similarly, there is a smaller gain in energy in adding an electron to a closed-shell species than to an open-shell species. Likewise, dipoles are more easily induced in open-shell species compared to closed-shell species. In addition to high IPs, low VDEs and ADEs, and low polarizabilities, magic clusters usually have large gaps between the highest occupied and lowest unoccupied molecular orbitals, HOMO-LUMO gaps, resulting from electronic shell closure. Lastly, magic clusters often have greater incremental binding energies, the energy necessary to remove one atom from the cluster, than their less magic neighbors.

### 1.2.3 Superatoms

The observation of properties dependent on cluster shell structure was reminiscent of atomic behavior and led to a very important outgrowth of the CNFEG model – the superatom concept. At its most fundamental, a superatom is a cluster that mimics the chemical properties of an atom on the periodic table and can be assigned an effective valence. As the field of cluster science grew, the idea of a superatom was refined so that currently only those clusters that exhibit energetic and chemical stability are considered; a superatomic cluster must maintain its chemical identity upon interaction with other species or incorporation into cluster assemblies.<sup>34</sup>

Superatoms have been identified consisting of atoms from across the periodic table, although we will only be concerned with those based on aluminum. A notable example of a superatom, and one of the first to be observed,<sup>7,17</sup> is  $\text{Al}_{13}^-$ , an icosahedron with a closed electronic shell of 40 valence electrons. As shown in Figure 1.2.3, the electronic level ordering is  $1\text{S}^2$ ,  $1\text{P}^6$ ,  $1\text{D}^{10}$ ,  $2\text{S}^2$ ,  $1\text{F}^{14}$ ,  $2\text{P}^6$ . The 1F orbitals split due to the icosahedral geometry, but overall the electronic structure corresponds with the spherical CNFEG model. The four 1F orbitals raised in energy are about degenerate with the 2P orbitals, so the cluster has a P subshell closing, similar to a noble gas atom. As a result of its closed shell,  $\text{Al}_{13}^-$  has a HOMO-LUMO gap of about 1.8 eV, uncharacteristic of metals which have no band gap. The cluster also displays decidedly unmetallic chemical behavior; it survives reaction with oxygen, water, and alcohols, and usually results as a product of the etching reactions of larger sized aluminum clusters with these species.<sup>9,37,38</sup> With its noble gas-like configuration and robust chemical inertness,  $\text{Al}_{13}^-$  enjoys status as a noble gas superatom.



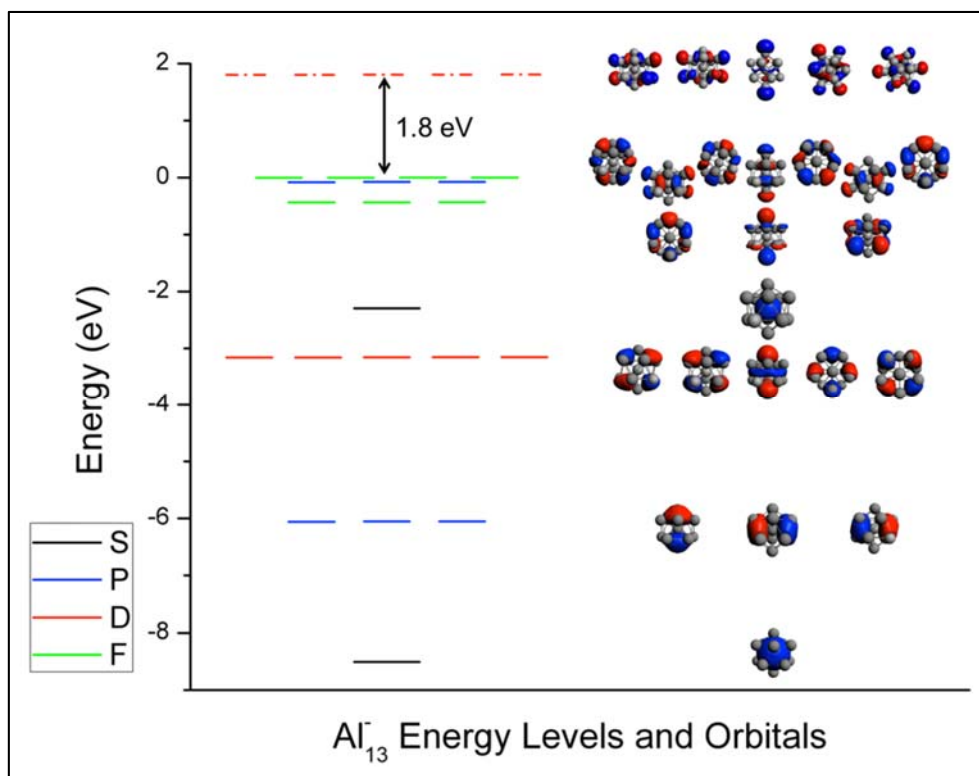


**Figure 1.2.3: Electronic energy levels and corresponding molecular orbitals of  $\text{Al}_{13}^-$ .** The electron levels and corresponding molecular orbitals are shown with the highest occupied orbital set to 0 eV. The CNFEG orbital type, S, P, D, or F, is indicated. Dashed lines indicate unoccupied orbitals, and the HOMO-LUMO gap is indicated.

Supratatomic behavior is not limited to electronically closed-shell species such as  $\text{Al}_{13}^-$ . Its neutral counterpart with 39 valence electrons,  $\text{Al}_{13}$ , has been the subject of much study. Only one electron shy of filling its 2P subshell,  $\text{Al}_{13}$  has an electron affinity of 3.4 eV, on par with the chlorine atom at 3.6 eV, leading to the early proposal by Khanna and Jena that it may be a supratatomic analogue of a halogen atom – a superhalogen. Further study of the bonding of  $\text{Al}_{13}$  with alkali metals and with other halogen atoms revealed that it does indeed exhibit chemical behavior similar to halogens. When  $\text{Al}_{13}$  combines with potassium, there is an electron transfer from K to  $\text{Al}_{13}$ .<sup>25</sup>  $\text{Al}_{13}\text{K}$ 's ionic character has been confirmed experimentally,<sup>50</sup> and its discovery served as a starting point for the design of cluster-assembled materials in the form of ionic salts. In combination with halogens,  $\text{Al}_{13}$  forms anionic complexes stable to reaction with  $\text{O}_2$  when the

number of iodine atoms is even –  $\text{Al}_{13}\text{I}_{2x}^-$ . In these clusters,  $\text{Al}_{13}$  withdraws charge from the I atoms, due to its greater electron affinity. These clusters are very similar to polyhalides of the form  $\text{X}_{2x+1}^-$ , where X is a halogen, except that the iodine bonds to  $\text{Al}_{13}$  as individual I atoms, rather than as  $\text{I}_2$ , owing to the greater strength of Al-I bonds compared to I-I bonds. With the I atoms decorating the larger  $\text{Al}_{13}$  core, these clusters resemble fluorohalides such as  $\text{BrF}_6^-$ .<sup>40,51</sup> Owing to electronic structure, electron affinity, and chemical bonding patterns analogous to a halogen atom,  $\text{Al}_{13}$  was confirmed as a superhalogen.

While  $\text{Al}_{13}^-$  displays properties of a noble gas and  $\text{Al}_{13}$  exhibits those of a halogen atom, aluminum-based superatoms showing metallic properties have also been identified. Much as  $\text{Al}_{13}$  forms stable anions with even numbers of iodine atoms,  $\text{Al}_{14}$  forms anions resistant to oxygen with odd numbers of iodine atoms,  $\text{Al}_{14}\text{I}_{2x+1}^-$ , for greater than three iodine atoms. In this case, the iodine atoms withdraw electrons from the  $\text{Al}_{14}$  core, until the core achieves a dication state,  $\text{Al}_{14}^{2+}$ , which takes the addition of at least three iodine atoms since the clusters are anionic. As a dication,  $\text{Al}_{14}$  has 40 valence electrons – a closed electronic shell as predicted by the CNFEG model. By losing the charge of two electrons through its bonds with iodine,  $\text{Al}_{14}$  becomes electronically stable. The loss of two electrons to achieve a closed shell state is characteristic of alkaline earth metals, and so  $\text{Al}_{14}$  is dubbed an alkaline earth metal superatom.<sup>40</sup> In some transition and post-transition metals, more than one valence or oxidation state is possible; for example, lead can exist as  $\text{Pb}^{+2}$  or  $\text{Pb}^{+4}$ . A similar multivalent cluster,  $\text{Al}_7^-$ , acts as a tetravalent element when it forms  $\text{Al}_7\text{C}^-$ , a cluster whose peak on mass spectra rivals that of  $\text{Al}_{13}^-$ , and acts as a divalent element when bonding with oxygen or sulfur. With its 22 valence electrons,  $\text{Al}_7^-$  can bond with either two or four electrons to gain a closed shell of 18 or 20 electrons,

respectively. Because of this,  $\text{Al}_7^-$  is known as a multivalent superatom akin to a post-transition metal such as lead or tin.<sup>52</sup>

#### 1.2.4 Extension of the CNFEG Model to Ligand-Protected Systems

As previously mentioned, the addition of ligands is one method of passivating and controlling the electronic structure of metallic clusters. Ligands such as thiols,<sup>53–61</sup> phosphines,<sup>53,62–64</sup> and halogens<sup>39,50,64,65</sup> have been successfully used to stabilize clusters. Essentially, a ligand can form an ionic or covalent bond with a metallic cluster which withdraws electrons from the core to the surface of the cluster, leaving the core with a stable, closed electronic shell.<sup>60</sup> The metallic core is treated separately from the ligands as a CNFEG described by the CNFEG model; this view has led to the term split-CNFEG when dealing with ligated metal clusters. There are many ligand-protected clusters whose stability has been rationalized within the CNFEG model. A popular class of such compounds is thiolated gold clusters.<sup>54–57,60,61</sup> For example, the cluster  $\text{Au}_{25}(\text{SR})_{18}^-$ , where SR is a thiol-containing organic group, is composed of an icosahedral  $\text{Au}_{13}^-$  metallic core of 14 electrons protected by six  $-\text{S}-\text{Au}-\text{S}-\text{Au}-\text{S}-$  staples. Each of these protective staples withdraws one electron from the core, leaving a closed-shell configuration on the gold cluster of  $1\text{S}^21\text{P}^6$ .

The extension of the CNFEG model to ligand-protected metal clusters also applies to our system of interest, iodized aluminum clusters. As discussed in the previous section,  $\text{Al}_{14}\text{I}_{2x+1}^-$  clusters show great stability because the iodine ligands withdraw charge from the metallic core, enabling the core to reach a +2 charge and become closed-shell  $\text{Al}_{14}^{+2}$ . For this reason, the stability of these clusters begins only when three iodine ligands are attached. If we think of it as a ligand-protected system, we can say that the  $\text{Al}_{14}^-$  metallic core has 43 valence electrons – three from each aluminum atom, and one to make the cluster anionic. Each iodine atom bonds with the

core, withdrawing one electron each, and leaving a stable closed-shell electronic configuration of 40 valence electrons. It should be noted, however, that not all cluster-ligand interactions are electron precise. Within the same series,  $\text{Al}_{14}\text{I}_5^-$  shows similar stability to oxygen etching and has a nearly identical HOMO-LUMO gap to  $\text{Al}_{14}\text{I}_3^-$  (1.31 eV compared to 1.34 eV), but 38 is not a magic number in the CNFEG model.<sup>40,51</sup>

### 1.2.5 Reactivity of CNFEG Clusters

Oxygen etching has long been a method of identifying stable clusters, as previously mentioned in the discussion of superatoms. For aluminum cluster anions, those clusters with odd numbers of electrons react with oxygen, while those clusters with even numbers of electrons show variable reactivity – some clusters, like  $\text{Al}_{13}^-$ ,  $\text{Al}_{23}^-$ , and  $\text{Al}_{37}^-$ , are incredibly stable, but others react away.<sup>7,8</sup> Addition of a hydrogen atom, and hence a single electron, to the clusters preserves the even/odd electron reaction behavior, indicating that the spin state of the cluster may be a key to its reactivity with oxygen.<sup>9</sup> The spin state of molecular oxygen is triplet, while anionic aluminum clusters are either spin singlet or doublet, for even and odd electron species, respectively. As per the Wigner-Witmer spin conservation rules, the reaction between an aluminum cluster and an oxygen molecule must conserve the overall spin of the system. Clusters with odd numbers of electrons react easily with oxygen because the unpaired electron on the cluster acts to fill one of the half-filled orbitals on  $\text{O}_2$ , so that the cluster-oxygen complex and the bare cluster have the same multiplicity. Clusters with even numbers of electrons show variable reactivity because some clusters can more easily accommodate triplet oxygen. With no unpaired electrons, even electron systems must promote a paired electron to a higher energy orbital, putting the cluster in a triplet state. The energy needed to do this is known as the spin excitation energy. Clusters with large HOMO-LUMO gaps, like  $\text{Al}_{13}^-$ , have correspondingly high spin

excitation energies, and are marked by a large barrier to accommodation of the spin on the oxygen atom; clusters with small HOMO-LUMO gaps do not require as much energy to promote an electron to the LUMO, and so will have small excitation energies, allowing reaction with  $O_2$  to occur more readily. The idea of spin accommodation can be adapted to any cluster system, including the system of interest,  $Al_nI_m^-$ . Shown in Figure 1.2.4 is the reaction of iodized aluminum clusters with oxygen. The even/odd electron behavior is clearly visible in panel (c), in which clusters with even numbers of electrons,  $Al_{13}I_{2x}^-$  and  $Al_{14}I_{2x+1}^-$ , resist oxygen etching.

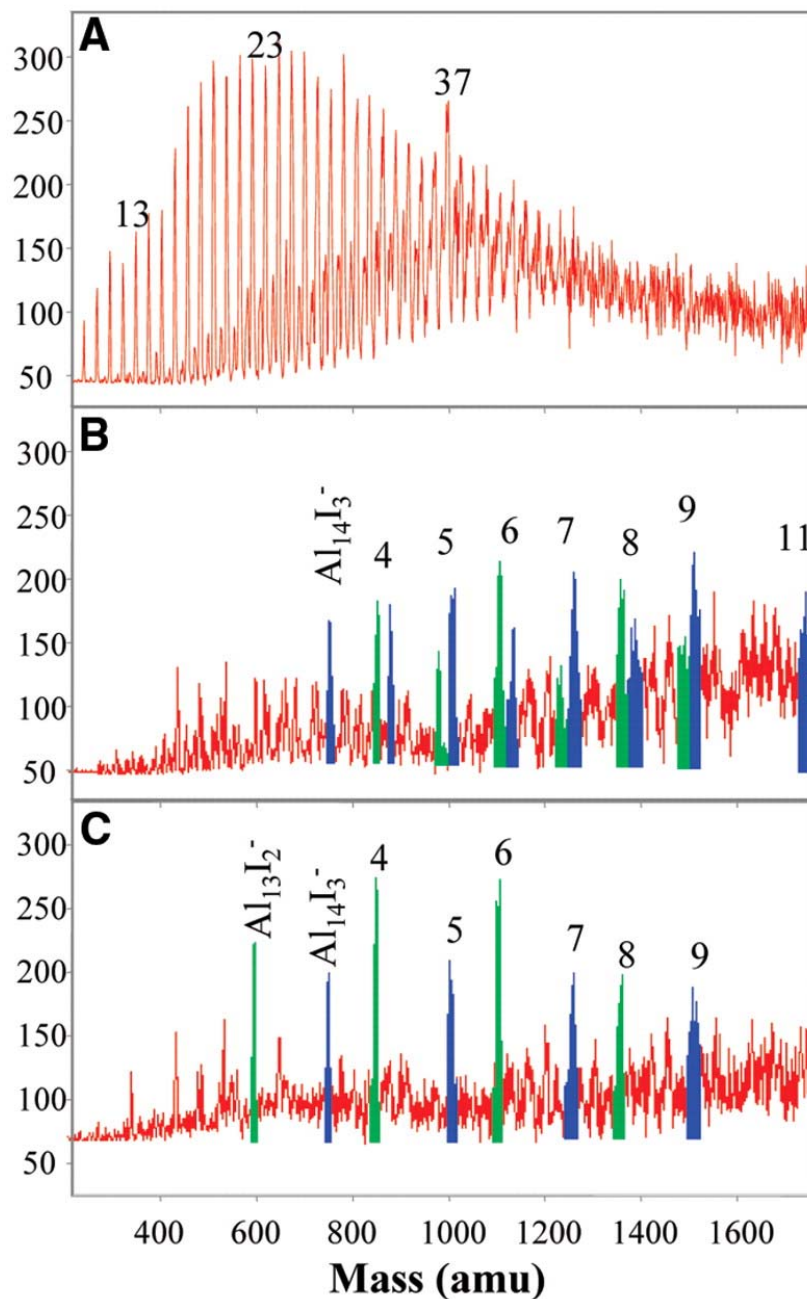


**Figure 1.2.4: Mass Spectra of  $Al_nI_m^-$  Clusters and Reaction with Oxygen.** Taken from Jones et al.<sup>40</sup> the above mass spectra show (a) the abundance of pure aluminum clusters, (b) the abundance of aluminum clusters of reaction with  $I_2$  gas, and (c) the abundance of iodized aluminum clusters after etching by  $O_2$ . Intensities are given in arbitrary units.  $Al_{13}I_x^-$  cluster peaks are highlighted in green, while  $Al_{14}I_y^-$  cluster peaks are highlighted in blue.

While cluster reactivity with  $O_2$  depends on electronic shell closure, the reactivity of aluminum-based clusters with alcohols and water appears to rely on a different mechanism. For

example,  $\text{Al}_{23}^-$  and  $\text{Al}_{37}^-$ , both stable to oxygen etching because of their rare gas-like electronic configurations, adsorb water molecules, while the open-shell cluster  $\text{Al}_{20}^-$  does not. To explain this reactivity, we turn to a familiar concept from traditional chemistry – Lewis acid-base theory. Within a molecule, lone pairs of electrons and differences in electronegativity between atoms result in sites capable of accepting or donating a pair of electrons, Lewis acid and base sites, respectively. Governed by the CNFEG model, the valence electrons in bare aluminum clusters are delocalized across the cluster, and no electronegativity differences exist between atoms. Geometric effects, however, can perturb the charge density of the cluster, causing more localized sites of HOMO or LUMO charge density to emerge. Concentrations of HOMO and LUMO density act as Lewis base and Lewis acid sites, respectively. These active sites enable the cluster's reaction with other acidic or basic species, such as water or alcohols. The acid and base sites must also be close to each other in the cluster, as they work in concert to break the O-H bond in the protic species; one Al atom acts as a Lewis acid and accepts an electron pair from the oxygen of water or alcohol, while a second, neighboring Al atom acts as a Lewis base and bonds with the hydrogen. In this way, two Al atoms on the cluster work as complementary active sites.<sup>36</sup> For example, as shown below in Figure 1.2.5,  $\text{Al}_{12}^-$  is a geometrically distorted cluster with an uneven charge distribution resulting in adjacent Lewis acid and Lewis base sites capable of breaking the O-H bond in water.

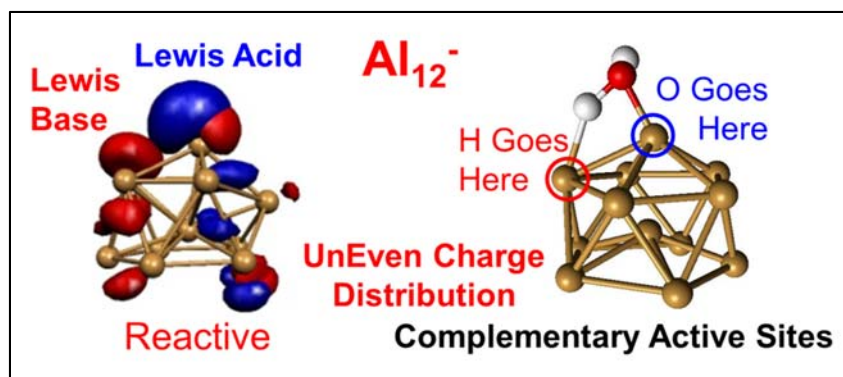


**Figure 1.2.5: Complementary Active Sites on  $\text{Al}_{12}^-$  Break the O-H Bond in Water.** On the left, the HOMO (red) and LUMO (blue) charge density of  $\text{Al}_{12}^-$  is shown, corresponding to Lewis base and Lewis acid sites respectively. On the right, a water molecule is shown with hydrogen (white) bonding to the Lewis base site and oxygen (red) bonding to the Lewis acid site. Figure courtesy of Dr. Arthur Reber.

More spherical clusters with an even charge distribution are less reactive toward water and alcohols than clusters with an uneven charge distribution resulting from geometric edges and defects. Complementary active sites have also been shown to enable aluminum clusters to break carbonyl bonds.<sup>67</sup>

### 1.2.6 Purpose of the Present Study

The present study seeks to build on previous theoretical and experimental reactivity work done on aluminum clusters by exploring the reactivity of  $\text{Al}_{13}\text{I}_x^-$  and  $\text{Al}_{14}\text{I}_y^-$  clusters with methanol. While the addition of electronegative ligands such as iodine can act to stabilize a cluster, it also distorts the electronic charge density of the cluster, just like geometric defects or edges. The disturbance of the metallic core's charge density can create active sites on the cluster's surface at which a protic species such as methanol may react. It is the hypothesis of this study that, in the same manner as edges and defects, the addition of electron-withdrawing iodine ligands to aluminum clusters will create a non-uniform charge density and, consequently, complementary Lewis acid-base active sites capable of breaking the O-H bond in methanol.



## 1.3 Silicon Encapsulated Transition Metal Clusters

### 1.3.1 Motivation

Clusters of silicon, the most widely used semiconductor in the electronics industry, doped with various transition metals (TM) have attracted attention for several reasons. At its most fundamental, the study of TM-doped silicon clusters offers the opportunity to study the metal-silicon bond in great detail, leading to a greater understanding of bulk systems; but just like other clusters, TM-doped silicon clusters exhibit properties different from the bulk, motivating the pursuit of stable clusters that can be used in cluster-assembled materials. Furthermore, it is difficult to dope bulk silicon with transition metal atoms. Using small clusters of silicon doped with TM atoms to build cluster-based materials from the bottom up would overcome this current limitation. Additionally, the use of magnetic transition metals could result in magnetic TM-doped silicon clusters, and, eventually, a magnetic silicon-based material.

The inherent structure of TM-doped silicon clusters provides additional impetus for their study. In contrast to carbon, which forms the fullerene structures previously discussed, pure silicon clusters tend to form prolate structures due to silicon's preference for  $sp^3$  bonding. These clusters also tend to be very reactive due to the dangling bonds of silicon.<sup>68</sup> When doped with a TM atom, however, silicon atoms will surround the metal to form clusters with cage-like or fullerene-like geometries. Beck first proposed the idea of silicon encapsulated TM clusters after producing  $TMSi_n^+$  (TM=Cr, Mo, W) clusters with laser vaporization of silicon and metal hexacarbonyls.<sup>69,70</sup> Beck found that  $TMSi_{13}$  through  $TMSi_{17}$  appeared in subsequent mass spectra, but that the highest peaks appeared at  $TMSi_{15}$  and  $TMSi_{16}$  for all metals studied, and postulated that these were endohedrally-doped silicon clusters wherein the metal atom acted as a seed around which the silicon atoms bonded. Subsequent theoretical work on TM-doped clusters

of this size regime confirmed the encapsulation of the transition metal atom by silicon, by showing that structures with an external TM atom are much higher in energy.<sup>71-73</sup> Experimental findings using X-ray fine structure also revealed that  $WSi_n$  clusters ( $n=8-12$ ) are indeed cage structures, verifying theoretical results.<sup>74</sup> The structure of silicon encapsulated TM clusters affords the opportunity to design CAMs from silicon in the same manner as from carbon fullerene clusters.

Further experimental and theoretical work revealed stable silicon encapsulated TM clusters for a variety of transition metal atoms. For example, Kumar et al. found numerous structures for early transition metals, including  $TMSi_{14}$ ,  $TMSi_{15}$ , and  $TMSi_{16}$ , for Ti, Hf, and Zr.<sup>68,73</sup> In particular,  $TiSi_{16}$  shows promise as a stable motif out of which to assemble a new material – it has a HOMO-LUMO gap of 2.36 eV and has been theoretically predicted to interact similarly to  $C_{60}$  clusters in a cluster-assembled material. Clusters of the same size range using Cr, Mo, and W were also theoretically studied, and  $TMSi_{14}$  was found to have the highest HOMO-LUMO gap in these clusters, despite its small abundance peak in Beck's original experiments.<sup>72</sup> More recent experimental work by Janssens et al., however, found  $CrSi_{14}^+$  to be similarly abundant to  $CrSi_{15}^+$  and  $CrSi_{16}^+$ .<sup>75</sup> Further, Hiura et al. found  $WSi_{12}^+$  clusters to be particularly stable in experiment, inspiring numerous studies on the  $WSi_{12}$  and congener cluster  $CrSi_{12}$ .<sup>76</sup> The wealth of studies concerning silicon encapsulated TM clusters cannot be reasonably covered within this thesis. The main focus will be on  $CrSi_{12}$ , a cluster which has attracted a great amount of theoretical attention. In fact, the stability of this cluster and the reason for that stability has been debated in the literature for years. In the remainder of this section, I will review the experimental and theoretical work lending support to the stability of  $CrSi_{12}$  and the electronic principles that have

been used to rationalize that stability, and hence the stability of TM-doped silicon clusters in general.

### 1.3.2 Is CrSi<sub>12</sub> a Magic Cluster?

Interest in the structure and stability of CrSi<sub>12</sub> began when Hiura et al. generated a variety of mixed transition metal-silicon clusters by reacting silane, SiH<sub>4</sub>, with pure transition metal vapor in an ion trap.<sup>76</sup> Time-resolved mass spectra of the reaction showed the sequential growth of the clusters formed with tungsten, isovalent with Cr, from W<sup>+</sup> through WSi<sub>12</sub>H<sub>x</sub><sup>+</sup>, as shown in Figure 1.3.1.

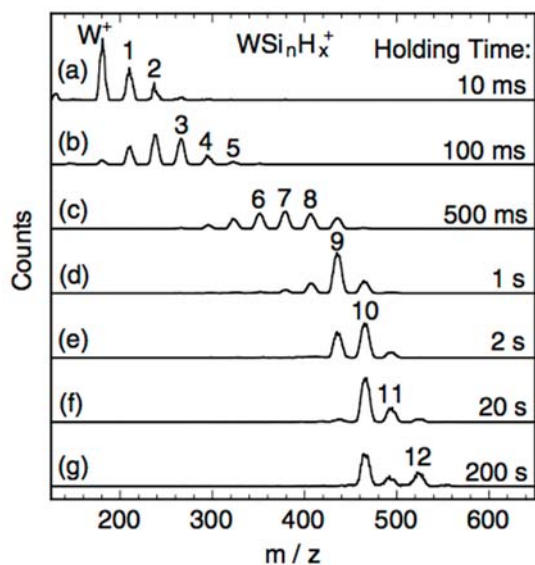


**Figure 1.3.1: Time-resolved mass spectra of WSi<sub>n</sub>H<sub>x</sub><sup>+</sup>.** Taken from Figure 1 of Hiura et al.<sup>76</sup> the above shows the time-resolved mass spectra of WSi<sub>n</sub>H<sub>x</sub><sup>+</sup> clusters formed in an ion trap using silane. Counts, or intensity, are shown in arbitrary units. The mass to charge ratio is shown on the x-axis. Holding times from (a) 10ms through (g) 200s are marked.

Clusters possessing more than twelve silicon atoms were not observed, even at the longest holding times, giving the first indications that WSi<sub>12</sub> might exhibit enhanced stability. Hiura et al. also examined the number of H atoms predominantly present on the cluster for each size using high resolution mass spectrometry. They found that the peak corresponding to WSi<sub>12</sub>H<sub>x</sub><sup>+</sup> was composed of about 70% pure WSi<sub>12</sub><sup>+</sup>, the greatest proportion of dehydrogenated clusters

present in the range of one to twelve silicon atoms. The remaining portion was mostly  $\text{WSi}_{12}\text{H}_2^+$ , with less than 5%  $\text{WSi}_{12}\text{H}_4^+$ . To see this more clearly, the histogram of the hydrogen analysis is given in Figure 1.3.2.

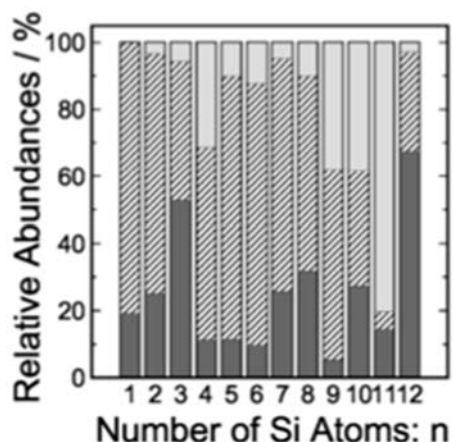


**Figure 1.3.2: Relative Abundances of  $\text{WSi}_n\text{H}_x^+$  ( $n=1-12$ ;  $x=0, 2, 4$ ).** Taken from Hiura et al.<sup>76</sup> the percentage of clusters containing zero, two, and four hydrogens are shown in dark gray, shaded gray, and white, respectively, for each cluster.

Comparison to  $\text{WSi}_{10}\text{H}_x^+$  and  $\text{WSi}_{11}\text{H}_x^+$ , the only other remaining peaks in the time-resolved mass spectra at the longest holding time, gives further evidence to the stability of  $\text{WSi}_{12}$ .

$\text{WSi}_{10}\text{H}_x^+$  was comprised of about 30% each  $\text{WSi}_{10}^+$  and  $\text{WSi}_{10}\text{H}_2^+$ , with the remaining 40%  $\text{WSi}_{10}\text{H}_4^+$ , while  $\text{WSi}_{11}\text{H}_x^+$  was comprised of almost entirely all  $\text{WSi}_{11}\text{H}_4^+$ , with only about 15% pure  $\text{WSi}_{11}^+$  and 5%  $\text{WSi}_{11}\text{H}_2^+$ . Overall, the absence of larger cluster sizes, and the preponderance of bare  $\text{WSi}_{12}^+$  clusters, led Hiura et al. to propose enhanced stability for  $\text{WSi}_{12}$ , citing different production methods as explanation of the different results obtained by Beck, in which  $\text{TMSi}_{12}$  ( $\text{TM}=\text{Cr}, \text{Mo}, \text{W}$ ) did not prominently appear.

Theorists quickly found that the favored structure of  $\text{WSi}_{12}$ , shown in Figure 1.3.3, is a hexagonal prism of silicon containing the metal atom,<sup>77</sup> similar to previously found clusters of  $\text{Cr}(\text{C}_6\text{H}_6)_2$ , in which the metal atom is sandwiched between two benzene molecules.<sup>78</sup>

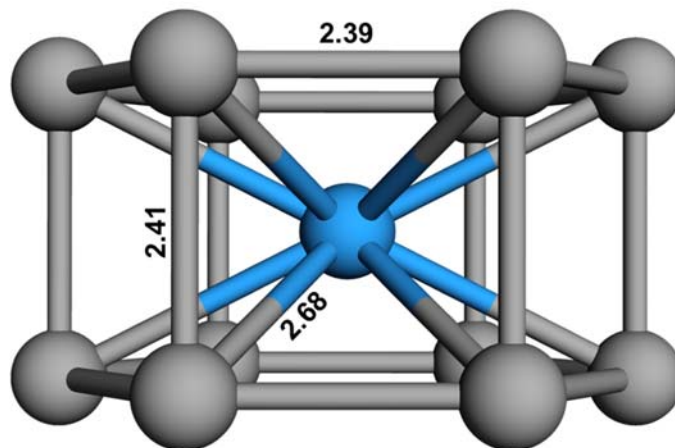


**Figure 1.3.3: Geometry of WSi<sub>12</sub>.** The hexagonal prism geometry with D<sub>6h</sub> symmetry of WSi<sub>12</sub> is shown above, with silicon atoms in gray and tungsten in light blue. Bond lengths are indicated in Angstroms.

While the work of Hiura et al. stimulated interest in WSi<sub>12</sub>, many theorists focused their attention on the congener cluster CrSi<sub>12</sub>. While the number of valence electrons remains the same, the smaller size of 3d chromium compared to 5d tungsten makes the CrSi<sub>12</sub> cluster more amenable to calculations. An early study of CrSi<sub>n</sub> (n=11-14) explored the notion of CrSi<sub>12</sub> magicity by calculating various properties associated with magic behavior in metal clusters.<sup>79</sup> The HOMO-LUMO gap does not indicate any special stability, being moderate at 0.94 eV. The cluster has identical VDE and ADE, calculated by Khanna et al. at 3.11 eV, and confirmed by experiment at 3.10 eV.<sup>80</sup> This is higher than the VDE and ADE of neighboring clusters. The ionization potential of CrSi<sub>12</sub> is higher than that of CrSi<sub>13</sub>, but not that of CrSi<sub>11</sub>. Finally, the incremental binding energy (BE) of silicon is largest for CrSi<sub>12</sub> in the range of n=11-14. While the IP and incremental BE indicate enhanced stability for CrSi<sub>12</sub>, the moderate HOMO-LUMO gap and high VDE and ADE do not.

The binary nature of these clusters provides the opportunity to calculate another useful stability criterion – the embedding energy. Sometimes called the dissociation, formation, or TM-removal energy, the embedding energy is the energy gained upon addition of the transition metal

atom. A larger embedding energy indicates greater stability. Sen and Mitas calculated the embedding energies of all the 3d transition metals, as well as some 4d and 5d metals, to gauge the stability of the TM in the hexagonal Si<sub>12</sub> cage.<sup>81</sup> They found that CrSi<sub>12</sub> did not have the highest embedding energy of the 3d metals; VSi<sub>12</sub>, TiSi<sub>12</sub>, FeSi<sub>12</sub>, and NiSi<sub>12</sub> all yielded larger values. WSi<sub>12</sub>, however, had the highest embedding energy of the 5d metals tested. In a similar study, Khanna and Reveles applied Wigner-Witmer spin conservation rules to the calculation of the embedding energy for the 3d metals.<sup>82</sup> By calculating the embedding energy with the energy of the metal atom in the same spin state as the cluster, usually singlet and doublet for even and odd electron clusters respectively, they found CrSi<sub>12</sub> and FeSi<sub>12</sub> to have enhanced stability. The application of Wigner-Witmer spin conservation to these clusters has not been uncontroversial. While Khanna and Reveles cite the previously miscalculated embedding energy of chromium in Cr-benzene complexes and the correct recalculation using Wigner-Witmer rules,<sup>78</sup> and He et al. used polarizability and chemical hardness to justify the use of the Wigner-Witmer rules in TMSi<sub>14</sub> clusters,<sup>83</sup> others view the use of spin conservation as unnecessary.<sup>84</sup> Despite the disagreement, the embedding energy remains a useful signpost of stability in these clusters.

As shown, the evidence for CrSi<sub>12</sub> magicity is mixed. The cluster appears in some experiments, but not intensely in others. The high ionization potential and large incremental binding energy indicate stability, but other values, such as the VDE, ADE, and HOMO-LUMO gap, give no indication of special stability compared to other clusters in the size range. That not all of the markers for enhanced stability found in magic metallic clusters are present could mean, as Khanna put forth, that covalent clusters such as these operate under different stability criteria;<sup>79</sup> there are of course other cluster types, even metal clusters, whose electronic structure follows different rules such as aromaticity or Wade-Mingos rules.<sup>34</sup> The inconsistency in

experiment and in the calculated numbers could also indicate a more complicated mechanism of stability. In regards to this, what principles may play a role?

### 1.3.3 The 18-Electron Rule

Within the 18-electron rule, a mainstay of transition metal chemistry, the stability of a transition metal complex depends on the filling of the d and p orbitals on the metal center.<sup>85</sup> The goal, similar to the octet rule for elements in the first two rows of the periodic table, is to achieve a noble-gas configuration,  $ns^2(n-1)d^{10}np^6$ . An example of a complex which follows the 18-electron rule is  $\text{Cr}(\text{CO})_6$ . Chromium has a valence electron configuration of  $4s^13d^5$ , for a total of six valence electrons. Each carbon monoxide ligand donates two electrons to the chromium atom, giving it a total of 18 electrons. As shown in Figure 1.3.4, the 4s, 3d, and 4p orbitals of chromium are occupied through bonding with the CO ligands.

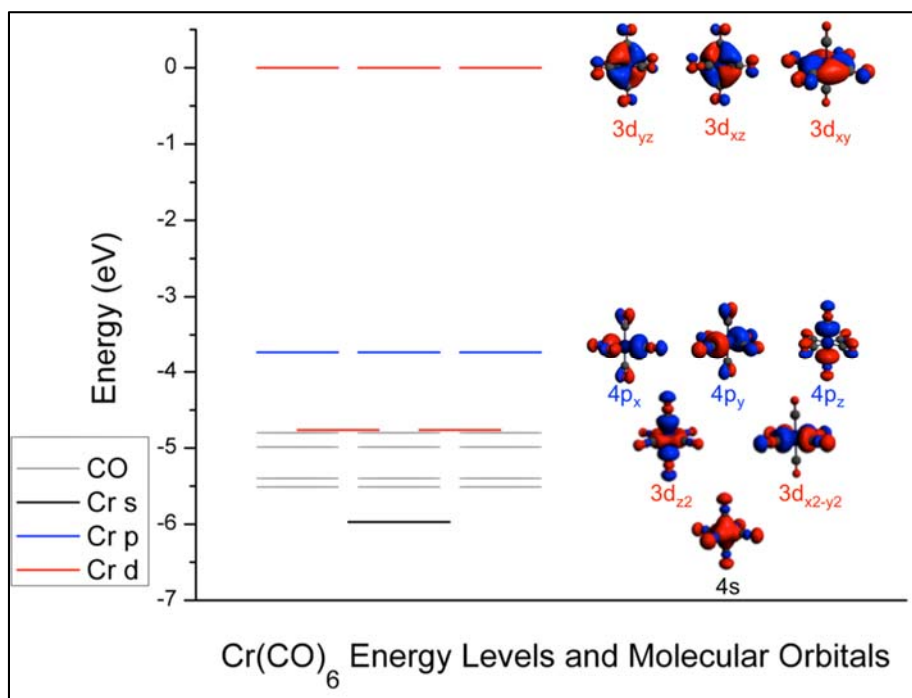


**Figure 1.3.4: The Energy Levels and Molecular Orbitals of  $\text{Cr}(\text{CO})_6$ .** To show the 18-electron rule, levels with chromium 4s, 3d, and 4p character are shown in black, blue, and red, respectively, on the left, and the corresponding orbital is pictured on the right. Levels with mostly or all CO character are shown in gray.

Note that often the p orbitals of the metal do not bond as strongly as the d orbitals. For example, fragment analysis of  $\text{Cr}(\text{CO})_6$  reveals that the molecular orbitals labeled as 4p in Figure 1.3.4 contain only 6% chromium 4p orbital character, while the  $3d_{z^2}$  and  $3d_{x^2-y^2}$  molecular orbitals contain about 31% chromium character, and the remaining 3d orbitals contain 59% chromium character. That the filling of the d states seems more important to the molecule's stability, whether or not the p-states are filled, has led some to reduce the 18-electron rule to the 12-electron rule. This has not, however, been widely accepted.<sup>86</sup> Within this thesis, the view of Pyykkö will be used; the 18-electron rule involves the filling of both the d and p orbitals on the transition metal, although the d orbital character in resulting molecular orbitals is expected to be more prominent.<sup>87</sup>

While the 18-electron rule has been found to accurately predict stable complexes for most transition metals with a variety of ligands, such as carbon monoxide (CO), phosphines ( $\text{PR}_3$ ), halogens (X), amines ( $\text{NH}_3$ ), etc., it does, like all rules in chemistry, have exceptions.<sup>85</sup> Some early transition metals will form stable complexes with less than 18 electrons, due to the larger size of the TM atom, the lower number of electrons the TM atom starts with, or steric hindrance of the binding ligands.  $\text{V}(\text{CO})_6$  with 17 electrons and  $\text{W}(\text{CH}_3)_6$  with 12 electrons are examples of stable complexes with less than 18 electrons. The most major exception to the 18-electron rule earns its own designation as the 16-electron rule. Many square-planar complexes are stable with an electron count on the metal atom of only 16; in the square-planar complex  $\text{PtCl}_4^{2-}$ , the platinum atom already has 10 electrons and receives 4 more, one from each of the chlorine atoms, and the overall -2 charge gives platinum a total of 16 electrons. The 16-electron rule is not limited to square-planar complexes. In the tetrahedral complex  $\text{Ni}(\text{CO})_4$ , the CO ligands contribute 8 electrons to nickel, which already has 8 valence electrons, for a stable 16-electron



center. Complexes following the 16-electron rule usually have TM centers that already possess a large complement of d-electrons; Ni, Rh, Ir, Pt, and Pd commonly form complexes with 16 electrons.

Hiura et al. proposed that  $\text{WSi}_{12}$  is stable due to the 18-electron rule, assuming that each silicon atom donates one electron through covalent bonding to the chromium atom; the addition of 12 electrons from the silicon cage to chromium's six valence electrons gives a total of 18 electrons.<sup>76</sup> The structure of  $\text{WSi}_{12}$  and  $\text{CrSi}_{12}$  seems to support this argument as well - each silicon atom is bonded to three other silicon atoms, as well as to the chromium atom, ostensibly indicating electron-precise  $\text{sp}^3$  bonding. Note that we have already seen that electron-precise bonding is not necessarily the norm for clusters – recall  $\text{Al}_{14}\text{I}_5^-$ , which obtained a 40-electron closed-shell core through ligation with five, rather than three, iodine ligands. To provide further evidence for the 18-electron rule, Khanna et al. carried out studies on other 3d metal clusters in the same size range.<sup>88</sup> If this counting rule were true, then  $\text{FeSi}_{10}$  should also be magic, since iron has two more electrons than chromium to begin with, and each silicon atom would donate one electron to give a total of 18. A study of  $\text{FeSi}_n$  from  $n=9-11$  did show that  $\text{FeSi}_{10}$  had a higher incremental binding energy than its neighbors, with an energy gain of 4.71 eV from  $\text{FeSi}_9$ . The ionization potential and HOMO-LUMO gap are also larger than  $\text{FeSi}_9$  and  $\text{FeSi}_{11}$ , although the gap is still moderate at only 1.10 eV. The 18-electron rule has not been readily accepted by everyone as a guiding principle for  $\text{TMSi}_n$  clusters; studies cite the stability of  $\text{MSi}_{16}$  clusters, which cannot be explained as 18-electron systems within an electron-precise bonding scheme, as well as the mixed results establishing the stability of  $\text{CrSi}_{12}$ , as evidence that the 18-electron rule may be too simple a description.<sup>81,84,89</sup>

### 1.3.4 Application of the CNFEG Model

A full treatment of  $\text{CrSi}_{12}$  with the CNFEG model has not been suggested by many researchers; however, Kumar proposed that it is magic under a “cylindrical” CNFEG model,<sup>68</sup> which is another way of referring to the ellipsoidal CNFEG model discussed in Section 1.2.2. With four electrons from each silicon atom and six electrons from the metal atom, the total valence electron count for  $\text{CrSi}_{12}$  is 54, a magic number predicted by the ellipsoidal CNFEG model. More commonly, a split-CNFEG model has been used.<sup>82,90,91</sup> Within this model, the metal atom is treated as a CNFEG, while the silicon atoms are treated as ligands contributing electrons to the metal center. Again, it is assumed that each silicon atom donates one electron to the metal atom through covalent bonding. For  $\text{CrSi}_{12}$ , then, the chromium atom attains a CNFEG closed shell of 18 electrons.

The application of a split-CNFEG model to  $\text{CrSi}_{12}$  does not seem to differ from the 18-electron rule at first glance, as the metal atom still obtains 18 electrons; an 18-electron atomic shell closure ( $4s^23d^{10}4p^6$ ) corresponds rather identically to an 18-electron CNFEG shell closure ( $1S^21P^61D^{10}$ ) on a single atom. To test the split-CNFEG model, Khanna and Reveles attempted to extend it to 20-electron clusters. The first of these is  $\text{FeSi}_{12}$ , which showed the second highest embedding energy of all  $\text{TMSi}_{12}$ , with TM being a 3d metal.<sup>82</sup> This number resulted from calculations using the Wigner-Witmer spin conservation rules. Another study that did not apply spin conservation found the embedding energy of  $\text{FeSi}_{12}$  to be greater than that of  $\text{CrSi}_{12}$ , again indicating the stability of  $\text{FeSi}_{12}$ .<sup>81</sup> The idea of a CNFEG shell closure was further applied to clusters containing more than 12 silicon atoms, notably  $\text{TMSi}_{16}$  where TM = Sc, Ti, and V. Khanna and Reveles found that  $\text{ScSi}_{16}^-$ ,  $\text{TiSi}_{16}$ , and  $\text{VSi}_{16}^+$ , all 20-electron systems, showed enhanced stability based on embedding energies with spin conservation.<sup>90</sup> These clusters have

also shown stability in experiments; all three are found with great intensity in mass spectra and are resistant to binding water.<sup>92</sup> A 20-electron shell closure has also been considered for CrSi<sub>14</sub>.<sup>83</sup> In the literature, the CNFEG shell closure at 20 electrons is sometimes referred to as the 20-electron rule.

### 1.3.5 Crystal-Field Splitting

Another consideration that must be taken into account when dealing with transition metals is that of crystal-field splitting.<sup>85,93</sup> In crystal-field theory, ligands are considered to be negative point charges that interact via electron repulsion with the d-orbitals of the transition metal. In the spherically symmetric case, all d-orbitals are degenerate, that is, at the same energy. When surrounded by ligands in a non-spherical arrangement, the d-orbitals of the transition metal will split into non-degenerate groups. Generally, orbitals that interact more strongly with ligands, so that repulsion between electrons is greater, will be pushed up in energy compared to those orbitals that do not interact as strongly.

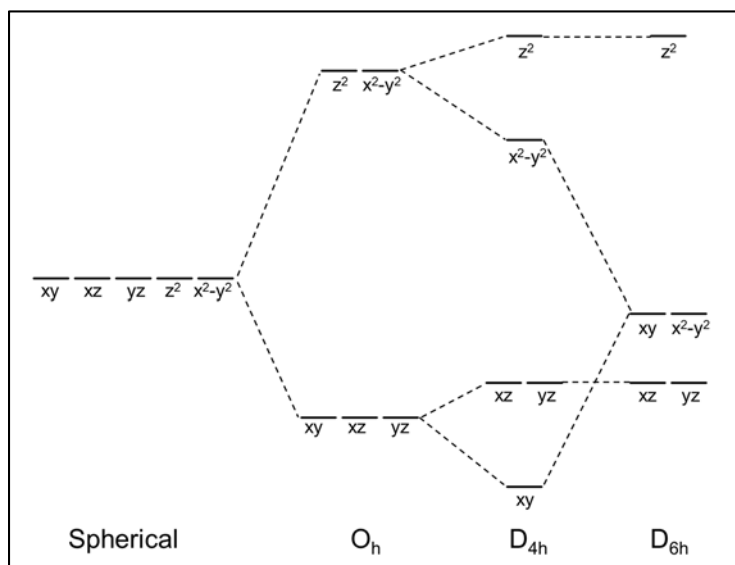


**Figure 1.3.5: Crystal-Field Splitting of d-orbitals for Several Symmetries.** The splitting of the d-orbitals is shown from the spherical case to the octahedral ( $O_h$ ), square-planar ( $D_{4h}$ ), and  $D_{6h}$  symmetry case. Each d-orbital is indicated as  $xy$ ,  $xz$ ,  $yz$ ,  $z^2$ , or  $x^2-y^2$ . Splitting distances are qualitative only. In the  $D_{4h}$  case, the splitting reflects compression along the z-axis.

Figure 1.3.5 shows the splitting arrangement for the octahedral ( $O_h$ ),  $D_{4h}$ , and  $D_{6h}$  symmetry point groups. For an octahedral complex, the d orbitals of the metal will split into two sets:  $d_{z^2}$  and  $d_{x^2-y^2}$ , pushed up in energy compared to the spherical case, and  $d_{xy}$ ,  $d_{yz}$ , and  $d_{xz}$ , lowered in energy compared to the spherical case. Upon compression of the z-axis, leading to  $D_{4h}$  symmetry, the d-orbitals with a z-component will be raised in energy relative to the  $O_h$  case, while the other orbitals will be lowered in energy. In a  $D_{6h}$  molecule, such as  $CrSi_{12}$ , the  $d_{xy}$  and  $d_{x^2-y^2}$  orbitals and the  $d_{xz}$  and  $d_{yz}$  orbitals are degenerate, while the  $d_{z^2}$  orbital is raised highest in energy.<sup>78</sup> Recall that crystal-field theory models the ligands as point charges and the splitting of the orbitals as a result of purely electrostatic effects, but the type of ligand will also affect the extent of d-orbital splitting.<sup>85,93</sup>

Crystal-field splitting has been found to play roles in the stability of clusters, including those governed by the CNFEG model. For example, in the cluster  $Al_{22}Cu^-$ , the 2D orbitals, with  $A_1$  symmetry, split similarly to the  $D_{6h}$  case shown in Figure 1.3.5, due to the oblate geometry of the cluster.

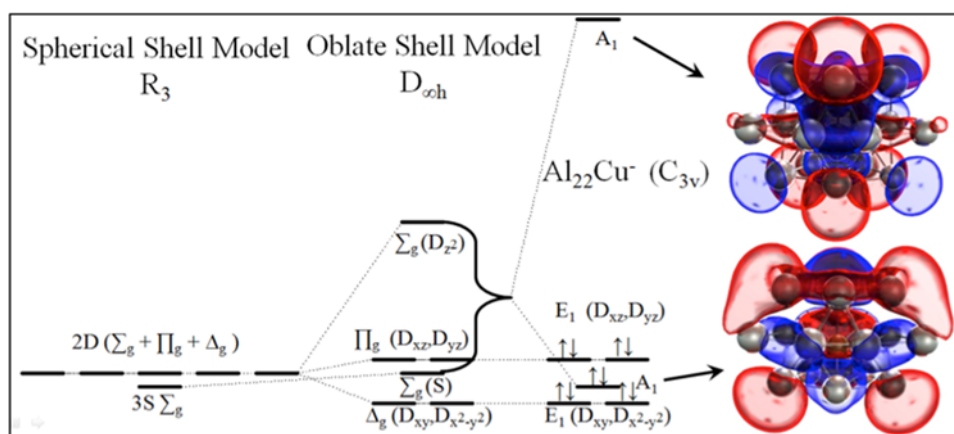


**Figure 1.3.6: Crystal-Field Splitting in  $Al_{22}Cu^-$ .** The splitting of the 2D orbitals are shown for a spherical shell model (left), an oblate shell model (middle), and for  $Al_{22}Cu^-$  (right) with accompanying  $A_1$  orbital images for the cluster.

As Figure 1.3.6 shows, the  $2D_{z^2}$  orbital is raised high in energy, and is empty, while the remaining 2D orbitals are lowered in energy, lending overall stability to the cluster.<sup>94</sup> Another

example is  $\text{Ag}_{13}^-$ , which despite having 14 valence electrons (not a magic number), has a large HOMO-LUMO gap and is stable to reaction with  $\text{O}_2$ . Unlike  $\text{Al}_{13}^-$ ,  $\text{Ag}_{13}^-$  does not form an icosahedron, but rather a bilayer structure. Due to this geometric distortion, the 1D subshells split – two are filled while the remaining three are unfilled and raised in energy-leading to the large HOMO-LUMO gap that lends  $\text{Ag}_{13}^-$  its stability.<sup>95</sup> Other subshells can show crystal-field-like splitting as well;  $\text{Al}_{11}\text{Mg}_2^-$  and  $\text{Al}_{11}\text{Mg}^-$ , both having oblate geometries, gain stability through splitting of the 2P and 1F subshells, respectively.<sup>96</sup> The  $D_{6h}$  symmetry of the cluster of interest,  $\text{CrSi}_{12}$ , implies a crystal-field splitting as shown in Figure 1.3.5, with the  $3d_{z^2}$  orbital of Cr being pushed up in energy. This was pointed out by Kumar,<sup>68</sup> however no molecular orbital analysis has been done to explore the orbital splitting and its possible effects on the cluster's stability.

### 1.3.6 Purpose of the Present Study

As demonstrated in the preceding sections, the stability, and what mechanisms are responsible for that stability, of  $\text{WSi}_{12}$  and congener  $\text{CrSi}_{12}$  has been a matter of intense debate in the literature. Both the 18-electron rule from inorganic chemistry and an 18-electron CNFEG shell closure, extendable to a 20-electron shell closure for other species, have been suggested, and crystal-field splitting may also contribute. It is important to note that all of the counting rules that have so far been applied have assumed that the bonding in the cluster is electron-precise, that is, each silicon atom contributes exactly one electron to the chromium or tungsten atom through a covalent bond. Studies have focused on proving that  $\text{CrSi}_{12}$  and  $\text{WSi}_{12}$  do exhibit signs of enhanced stability, on showing that neighboring clusters that also presumably have 18 electrons on the TM atom, such as  $\text{FeSi}_{10}$ , are also relatively stable, and, in the case of a split-CNFEF model, on extending the counting rule to 20-electron systems such as  $\text{TiSi}_{16}$ . No studies, however, have ever called into question whether  $\text{CrSi}_{12}$  and  $\text{WSi}_{12}$  are indeed 18-electron

systems. Interestingly, preliminary calculations show that the LUMO of  $\text{CrSi}_{12}$ , shown in Figure 1.3.7, is the  $3d_{z^2}$  orbital of chromium.

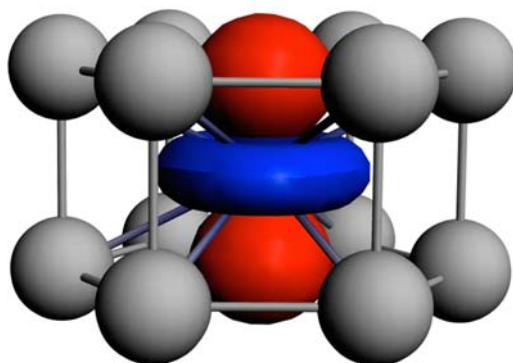


**Figure 1.3.7: Lowest Unoccupied Molecular Orbital of  $\text{CrSi}_{12}$ .** The LUMO of  $\text{CrSi}_{12}$  is shown to be the  $3d_{z^2}$  atomic orbital of the chromium atom.

With an empty  $3d_{z^2}$  orbital, it seems clear that not all the d and p orbitals of the chromium atom are filled by bonding with the silicon ligands – the 18-electron rule is not satisfied. This empty  $D_{z^2}$  orbital also has significance for a CNFEG or split-CNFEG description of the electronic structure, as the split-CNFEG model predicts the LUMO to be a 2S orbital, following shell closure at  $1D^{10}$ .

The present study seeks to determine if the 18-electron rule or 18-electron CNFEG shell closure applies – that is, are  $\text{CrSi}_{12}$  and  $\text{WSi}_{12}$  actually 18-electron systems? This will be done using an extensive molecular orbital (MO) analysis of  $\text{CrSi}_{12}$ . Such a MO analysis has not been done previously for either  $\text{CrSi}_{12}$  or  $\text{WSi}_{12}$ , although some researchers have looked at the frontier orbitals of select  $\text{TMSi}_n$  clusters. Fragment analysis of the MOs will provide information on the composition of each orbital, which can cast light on whether the 3d and 4p orbitals of chromium are filled. (This was done for  $\text{Cr}(\text{CO})_6$  as an example in Figure 1.3.4). To further reexamine the stability of  $\text{CrSi}_{12}$  and as a search for other relatively stable clusters, energetic properties will be calculated for  $\text{CrSi}_n$  ( $n=6-16$ ). It has also been assumed that in these clusters, chromium and tungsten would act identically, but due to their different sizes and to the fact that tungsten

possesses f electrons while chromium does not, this may not be the case. Thus, the same energetic analysis will be applied to  $WSi_n$  ( $n=6-16$ ) in order to show any differences in the behavior between W-doped and Cr-doped clusters. Through the recalculation of energetic properties in a wide size range and the careful examination of the MOs of selected clusters, the goal of this study is to contribute to a better conceptual understanding of the electronic principles governing the stability of silicon encapsulated TM clusters.

## 1.4 Organization of This Thesis

In Chapter 2, I will discuss the theoretical basis of density functional theory, the formalism used for the calculations in this thesis, as well as the computational methodologies used in each study to implement it. Chapter 3 will cover the results for the ligated metal cluster example, reactivity of  $Al_{13}I_x^-$  and  $Al_{14}I_y^-$  with methanol, including experimental results. Chapter 4 will cover the silicon encapsulated transition metal clusters  $CrSi_n$  and  $WSi_n$  in three portions: the first, a comparative study of  $CrSi_n^-$  to establish the appropriate functional to use for these clusters (functionals will be discussed in detail in Chapter 2); the second, the energetic properties and molecular orbital analysis of  $CrSi_n$ ; and the third, the energetics and a brief molecular orbital analysis of  $WSi_n$ . The concluding chapter will relate the results found in the two example studies to the overall process of finding and using electronic principles to describe and predict the properties of clusters.

## 2 Methods

### 2.1 Overview

Within this thesis, the electronic structure calculations are performed using density functional theory (DFT), a framework in which the electron density rather than the wavefunction is the primary variable. This chapter will briefly cover the development and theoretical background of DFT, focusing on the Hohenberg-Kohn theorems and the Kohn-Sham equations. The computational methodology used to implement the DFT calculations will also be described for both the ligated metal clusters study and the silicon encapsulated transition metal clusters study, as different software was used in each case.

### 2.2 Density Functional Theory

#### 2.2.1 The Electron Density

The goal of electronic structure calculations is to find the solution, a wavefunction, to the time-independent Schrödinger equation, from which one can glean all the information concerning the electronic structure of a system. Unfortunately, an analytical solution is only possible for a one-electron system, and approximations need to be made in order to find a solution for larger systems. For example, the Born-Oppenheimer approximation<sup>97</sup> uses the fact that nuclei are much heavier than electrons to consider the electrons in a system as moving against a field of fixed nuclei. This allows the dropping of the nuclear kinetic energy term and converts the nucleus-nucleus interaction term to a constant. While this simplifies the Hamiltonian to a certain degree, actually finding the wavefunction still requires searching through all possible wavefunctions to minimize the energy as per the variational principle – still an insurmountable task. Most approximation methods based on the variational principle search



only a subset of the possible wavefunctions. For example, the Hartree-Fock (HF) method considers the many-electron wavefunction to be an antisymmetrized product of  $N$  single-electron wavefunctions, known as a Slater determinant. Rather than from the total wavefunction, the energy is found from the expectation value of the Hamiltonian written in terms of this Slater determinant.<sup>98</sup>

The HF method serves as the groundwork for many wavefunction-based quantum mechanical methods, however these methods tend to be computationally expensive. The wavefunction remains a complicated quantity that depends on  $4N$  variables, where  $N$  is the number of electrons, and systems of interest in chemistry and materials science tend to have many electrons. As an alternative, DFT employs the electron density as the principle variable, rather than the wavefunction. The electron density,  $\rho(\vec{r})$ , displays several important properties that make its use as a variable advantageous. Depending only on the three spatial coordinates, the electron density, unlike the wavefunction, is an experimentally measurable quantity (by, for example, X-ray diffraction). It also only exhibits maxima at the positions of the nuclei, and the value of the density at these positions provides information about the atoms of the system, specifically their nuclear charge. Finally, the electron density integrates over all space to give the total number of electrons in the system. Thus, the electron density provides all the information on which the Hamiltonian depends: the number of electrons, and the positions and charges of the nuclei. For this reason, it is plausible that the electron density could be used as the variable for approximately solving the Schrödinger equation.

### **2.2.2 The Hohenberg-Kohn Theorems**

While the previous section showed that the use of the electron density might be reasonable, proof that the electron density does uniquely determine the Hamiltonian and thereby

all the properties of the system, came with the work of Hohenberg and Kohn.<sup>99</sup> In the first of two theorems, they stated:

The external potential  $V_{\text{ext}}(\vec{r})$  is (to within a constant) a unique functional of  $\rho(\vec{r})$ ; since, in turn  $V_{\text{ext}}(\vec{r})$  fixes  $\hat{H}$ , we see that the full many particle ground state is a unique functional of  $\rho(\vec{r})$ .

Their proof showed that two different potentials,  $V_{\text{ext}}(\vec{r})$  and  $V'_{\text{ext}}(\vec{r})$ , cannot produce the same electron density,  $\rho(\vec{r})$ , which means that the true ground state density,  $\rho(\vec{r})$ , uniquely defines the external potential,  $V_{\text{ext}}(\vec{r})$ , (to within a constant). The key here is that the electron density is now justified as a physically sound parameter in determining the external potential, which for a chemical system would consist of the electron-nuclear potential. The Hamiltonian also contains an electron kinetic energy term and an electron-electron repulsion term, which Hohenberg and Kohn proposed are, like  $V_{\text{ext}}(\vec{r})$ , functionals of the electron density. That is,

$$F_{\text{HK}}[\rho] = T[\rho] + V_{\text{ee}}[\rho] = \langle \Psi | \hat{T} + \hat{V}_{\text{ee}} | \Psi \rangle, \quad (2.2-1)$$

where  $F_{\text{HK}}$  is a functional that produces the expectation values of the kinetic,  $\hat{T}$ , and electron-electron repulsion,  $\hat{V}_{\text{ee}}$ , operators in the ground state wavefunction when it operates on the electron density.

In their second theorem, Hohenberg and Kohn applied the variational principle to the their functional  $F_{\text{HK}}$ . It states:

A universal functional for the energy  $E[\rho]$  in terms of the density  $\rho(\vec{r})$  can be defined, valid for any external potential  $V_{\text{ext}}(\vec{r})$ . For any particular potential, the exact ground state energy of the system is the global minimum value of this functional, and the density that minimizes the functional is the exact ground state density  $\rho_0(\vec{r})$ .

Essentially, the functional will deliver the ground state energy of the system only if the input electron density is the true ground state density.

The two theorems of Hohenberg and Kohn provide proof that the previously discussed plausible arguments concerning the use of the electron density as a parameter rather than the wavefunction and arrive at the ground state energy of a system. These prove in principle that a unique mapping exists between the ground state electron density,  $\rho(\vec{r})$ , and the ground state energy; that is, the energy is a functional of the electron density. It is important to note, however, that the theorems do not explain how to construct the functional  $F_{\text{HK}}$  or how to come to a solution using it. Still, the proof of these principles laid the foundation for the development of practical density functional theory.

### **2.2.3 The Kohn-Sham Equations**

The work of Kohn and Sham<sup>100</sup> built upon the proofs discussed in Section 2.2.2 to give a practical method for actually approaching the functional defined by Hohenberg and Kohn. They used the idea that the exact calculation of many-body properties can, in principle, be determined by independent particle methods. The approach takes the many-body, interacting-particle system, which is difficult to solve, and replaces it with an auxiliary system of non-interacting particles. The auxiliary system is made up of single electron orbitals used to construct a Slater determinant, similar to how single electron wavefunctions were used to construct a Slater determinant in the Hartree-Fock approach. Within this method, the kinetic energy is split into two terms: one in which the exact kinetic energy of non-interacting electrons is computed - the main contribution to the kinetic energy - and another in which the electron correlation contribution to the kinetic energy is approximated - a relatively small contribution to the kinetic energy. This non-

interacting, auxiliary system is fictitious, but provides a reasonably accurate method to calculate the kinetic energy.

To actually represent this auxiliary system, a set of single electron orbitals, or Kohn-Sham orbitals, as they are commonly referred to, are used. These single electron orbitals are used to construct the auxiliary electron density,

$$\rho = \sum_{i=1}^{N_{\text{elec}}} |\phi_i|^2, \quad (2.2-2)$$

which is then operated on by the kinetic energy operator,

$$T[\rho] = \sum_{i=1}^{N_{\text{elec}}} \left\langle \phi_i \left| -\frac{1}{2} \nabla^2 \right| \phi_i \right\rangle, \quad (2.2-3)$$

to give the exact kinetic energy of a system of non-interacting electrons. The total energy within the Kohn-Sham approach becomes a functional of the electron density,  $\rho$ , and is written as

$$E_{\text{KS}} = T[\rho] + J[\rho] + E_{\text{Ne}}[\rho] + E_{\text{XC}}[\rho], \quad (2.2-4)$$

where  $T[\rho]$  is the exact kinetic energy of the non-interacting system,  $J[\rho]$  is the Coulomb repulsion between electrons, and  $E_{\text{Ne}}[\rho]$  is the Coulomb nuclear-electron repulsion. Each of these terms has an explicit functional form dependent only on the electron density, which is the sum of the single electron orbitals of Equation (2.2-2). These three terms make up the effective potential,  $V_{\text{eff}}$ , felt by the single electrons. Together with the kinetic energy operator,  $V_{\text{eff}}$  operates on the single electron orbitals, creating an eigenvalue problem:

$$\left( -\frac{1}{2} \nabla^2 + V_{\text{eff}}(\mathbf{r}_1) \right) \phi_i = \epsilon_i \phi_i. \quad (2.2-5)$$

Solving the Kohn-Sham orbitals can be done using the self-consistent field (SCF) method.

Within this method, one initially guesses a set of orbitals. Using these trial orbitals, a  $V_{\text{eff}}$  is constructed and used to solve the Kohn-Sham equations, which, in turn, gives rise to a new set of

orbitals. This iterative approach is continued until the input orbitals match the output orbitals, within a certain precision, at which point self-consistency is achieved. The Kohn-Sham approach is at the core of modern density functional theory.

#### **2.2.4 Exchange-Correlation Functionals**

The Kohn-Sham approach is useful because it turns a many-body problem into an independent-particle problem, by separating the exact kinetic energy for a system of non-interacting particles, and then putting the remaining contribution to the kinetic energy, as well as contributions to the potential energy, in the  $E_{XC}$  term. The exchange-correlation energy,  $E_{XC}$ , is the only remaining term in the Kohn-Sham energy for which there exists no explicit functional form. Much progress has been made to yield an approximate form, but modern research efforts are still aimed at improving  $E_{XC}$ . A popularly implemented treatment of  $E_{XC}$  is called the Local Density Approximation (LDA), which treats the local electron density as a slowly varying function that is essentially a homogeneous electron gas. Improving the accuracy of the LDA method, the Generalized Gradient Approximation (GGA) formalism is introduced. The GGA method includes not only information about the electron density,  $\rho(r)$ , at a particular point in space, but also the gradient of the electron density between two points,  $\nabla\rho(r)$ . The purpose is to account for the realistic nature of the true electron density, which is not the homogeneous electron gas as approximated by the LDA method. Perhaps the most commonly used variation of the GGA method is that implemented by Perdew, Burke, and Ernzerhof.<sup>101,102</sup> Even with this correction, GGA functionals are known to underestimate the HOMO-LUMO gap of a molecule or band gap of a solid. Another type of functional is a hybrid, which seeks to correct the underestimated band gap by incorporating some exact exchange, calculated using the Hartree-

Fock method. There are many examples of hybrid functionals, but the most commonly used is B3LYP, which usually includes 20% exact HF exchange.<sup>103,104</sup>

## 2.3 Computational Methods

### 2.3.1 Ligated Metal Clusters: $Al_nI_m^-$

For this project, the calculations were performed using a first-principles molecular orbital approach within a density functional theory framework, in which the molecular orbitals were represented as a linear combination of atomic orbitals centered on the atomic sites. In previous studies on aluminum cluster reactivity,<sup>9,36–38</sup> calculations were carried out using the Naval Research Laboratory Molecular Orbital Library (NRLMOL) set of codes,<sup>105–107</sup> and so the current study will also be done using NRLMOL. Similarly, the generalized-gradient approximation proposed by Perdew, Burke, and Ernzerhof (PBE)<sup>101,102</sup> was used to incorporate exchange and correlation in previous work with results consistent with experiment,<sup>36–38</sup> so PBE was used here as well. By using NRLMOL with the PBE functional in this current work, consistency across all of the aluminum cluster reactivity studies is achieved.

Within NRLMOL, the atomic orbitals were expressed as a linear combination of Gaussian orbitals located at the atomic sites. The basis set consisted of 6s, 5p, and 3d functions for aluminum; 8s, 7p, and 5d functions for iodine; 4s, 3p, and 1d functions for hydrogen; and 5s, 4p, and 3d functions for both carbon and oxygen. Optimization of the cluster geometries was done using a conjugate-gradient algorithm. The atoms of the cluster were moved in the direction of forces until those forces dropped below 0.05 eV per Å, at which point the geometry was considered converged. Molekel was used to visualize the geometric coordinate output, as well as to generate charge density isosurfaces of the frontier orbitals of each cluster. The latter was done in order to conduct a frontier orbital analysis and choose possible active sites. An isosurface

value of 0.03 electrons was used throughout. The search for structures along the reaction pathway and calculation of reaction pathway energies will be discussed in conjunction with the presentation of the results in Chapter 3.

### **2.3.2 Silicon Encapsulated Transition Metal Clusters: CrSi<sub>n</sub> and WSi<sub>n</sub>**

First-principles calculations within the DFT framework were carried out using the Amsterdam Density Functional (ADF) software package.<sup>108–110</sup> ADF was chosen because it allows for fragment analysis, which is a powerful tool in understanding the bonding in these clusters. Both the GGA PBE functional<sup>101,102</sup> and the hybrid B3LYP functional<sup>103,104,111</sup> were used to incorporate exchange and correlation, as testing of functionals was necessary in this case. For PBE calculations, a small core was used, meaning that the 1s, 2s, and 2p orbitals of silicon, chromium, and the 1s, 2s, 2p, 3s, 3p, 3d, 4s, 4p, and 4d orbitals of tungsten were frozen during the calculation. B3LYP calculations were all-electron, as the frozen core approximation has not yet been implemented for hybrid functionals within the ADF code. The excitations of the anionic clusters were found using time-dependent density functional theory (TDDFT) using the Tamm-Dancoff Approximation (TDA) within ADF.<sup>112–114</sup>

## 3 Ligated Metal Clusters

### 3.1 Overview

The overall purpose of this study is to explore the ways in which ligation with an electronegative atom such as iodine affects the reactivity of  $Al_n^-$  clusters with methanol. Induction of active sites by geometric defects and subsequent reactivity with  $H_2O$  and alcohols has been observed for bare aluminum clusters. Since ligands perturb the charge density of a cluster in a similar manner as geometric defects, it is hypothesized that the attachment of electronegative ligands to these clusters can induce complementary Lewis acid-base sites capable of breaking an O-H bond. In a broader sense, this study will test whether ligands can serve as activating species as well as protecting species, an important consideration for the design and synthesis of cluster-assembled materials. To this end, theoretical calculations were carried out on  $Al_{13}I_x^-$  ( $x=0-4$ ) and  $Al_{14}I_y^-$  ( $y=0-5$ ) clusters and their reactivity with methanol, as outlined in Chapter 2. In the first case, we explore the effect of ligating a superatom,  $Al_{13}^-$ , with an electronegative atom, iodine. Can reactivity with methanol be induced by such ligation? In the second case, we seek to determine the effect of adding an adatom defect to the  $Al_{13}I_x^-$  series. Does an adatom defect alone create a more reactive cluster, or is a ligand also necessary as an activating species? In the remaining sections, I will outline how the reaction pathways for each species were determined and discuss the results, which are published in the Journal of the American Chemical Society.<sup>115</sup> I will also present experimental confirmation of the results, carried out by our collaborators at the Pennsylvania State University.



## 3.2 Determining the Reaction Pathways of $\text{Al}_n\text{I}_m^-$ with Methanol

Determining the reaction pathway of a cluster with methanol involves several steps, the first of which is finding the ground state of the cluster. Because these clusters have been previously studied, the structures of  $\text{Al}_{13}\text{I}_x^-$  ( $x=0-4$ ) and  $\text{Al}_{14}\text{I}_y^-$  ( $y=0-5$ ) were built from the literature<sup>39,40,51,65</sup> and optimized as outlined in Chapter 2. The ground state structures of the  $\text{Al}_{13}\text{I}_x^-$  series have a very symmetrical arrangement of iodine atoms, especially in those clusters with an even number of iodines; therefore, an isomer of  $\text{Al}_{13}\text{I}_2^-$  with two iodine atoms on the same side was also studied. The inclusion of this additional structure allowed for the exploration of reactivity in clusters with unbalanced ligands.

Once all ground state structures had been found, possible active sites were chosen based on a frontier orbital analysis. The charge densities of the HOMO and LUMO of each cluster were examined. In the case of clusters with an odd number of electrons, the HOMO and LUMO are actually a singly-occupied molecular orbital (SOMO) and singly-unoccupied molecular orbital (SUMO), respectively. Since a Lewis acid accepts an electron pair, and a SUMO cannot act as such, the second lowest unoccupied molecular orbital, LUMO+1, was considered for odd-electron species. For the remainder, LUMO will be used to indicate the lowest completely unoccupied molecular orbital, encompassing both of the unoccupied orbitals of interest, the actual LUMO in even-electron species and the LUMO+1 in odd-electron species. The SOMO will simply be referred to as a half-filled HOMO in odd-electron species. Aluminum atoms in the cluster with a large concentration of HOMO or LUMO charge density - that is those with strong Lewis base or Lewis acid character, respectively - were primarily chosen as reaction sites. Other sites, such as those aluminum atoms ligated with an iodine atom and, in the case of  $\text{Al}_{14}\text{I}_y^-$  clusters, the adatom defect, were chosen based on geometric considerations.

To find the methanol-bound state of each cluster, a methanol molecule was attached via the oxygen atom to each of the reaction sites chosen. The geometry of each of the resultant complexes was then optimized. The strength of the methanol-cluster binding was quantified by calculating the binding energy, BE, as shown in Equation (3.2-1).

$$BE = (E(\text{Al}_n\text{I}_m^-) + E(\text{CH}_3\text{OH})) - E(\text{CH}_3\text{OHAl}_n\text{I}_m^-)_{\text{ads}} \quad (3.2-1)$$

The binding energy is the difference between the sum of the total energies of the aluminum cluster and methanol in their separate ground states,  $E(\text{Al}_n\text{I}_m^-)$  and  $E(\text{CH}_3\text{OH})$ , and the total energy of the methanol-bound complex,  $E(\text{CH}_3\text{OHAl}_n\text{I}_m^-)_{\text{ads}}$ . This quantity can be used as a measure of Lewis acidity of each reaction site on a cluster. A larger binding energy indicates that the site is accepting a greater amount of charge from the lone pairs of electrons on methanol's oxygen atom, and thus that the site is a stronger Lewis acid. In principle, sites chosen based on a large concentration of LUMO charge density should be the strongest Lewis acids, and therefore have the largest values of BE. Based on the complementary active sites hypothesis, these Lewis acid sites are also the most probable sites on the cluster for breaking the O-H bond, though this also depends on the presence of a nearby Lewis base site.

The binding energy is related to the first quantity that will be used to describe the reaction pathways of  $\text{Al}_n\text{I}_m^-$  with methanol –  $E_B$ , the relative energy of the methanol-bound complex to the separated reactants. As Equation (3.2-2) below shows,  $E_B$  is essentially the negative of the binding energy, BE, described previously.

$$E_B = E(\text{CH}_3\text{OHAl}_n\text{I}_m^-)_{\text{ads}} - (E(\text{Al}_n\text{I}_m^-) + E(\text{CH}_3\text{OH})) = -BE \quad (3.2-2)$$

Distinction between the binding energy and  $E_B$  is necessary because binding energies are typically reported as positive quantities, while  $E_B$  is a negative quantity. Both BE and the absolute value of  $E_B$  quantify the Lewis acidity of a reaction site, as discussed above. A negative

quantity, however, more appropriately describes the initial methanol-cluster binding state along the reaction pathway, indicating that the methanol-bound complex is lower in energy than methanol and the aluminum cluster when separated.

The transition state structures for each reaction site were found using a linear transit approach, which has been used successfully in past theoretical reactivity studies.<sup>9,36-38</sup> Before beginning the linear transit procedure, the most likely site for hydrogen to bind upon O-H bond breaking was found. Starting with the methanol-bound complexes, the O-H bond was stretched to a length of 1.30 Å toward several neighboring aluminum atoms. This bond length has been found to be near the distance required to break the O-H bond in previous work.<sup>36-38</sup> The O-H bond length was fixed, while the rest of the complex was relaxed. The lowest energy complex resulting from this optimization indicated which aluminum atom is hydrogen's preferred binding site. The linear transit approach was then applied to this lowest energy complex. The O-H bond was stretched and compressed further by 0.01 Å, to 1.31 Å and 1.29 Å, respectively. These two structures were optimized with the O-H bond length again fixed. The path of steepest ascent in energy was chosen for continuation of the linear transit process. The O-H bond was stretched or compressed in 0.01 Å increments and fixed while the complex was optimized, until a saddle-point, or maximum, in the total energy was reached. The structure at this point of maximum energy is the transition state.

To describe the transition state, two relative energies were calculated: the relative transition state energy,  $E_T$ , and the activation energy,  $E_A$ . The first quantity was calculated as follows:

$$E_T = E(\text{CH}_3\text{OHAl}_n\text{I}_m^-)_{\text{TS}} - (E(\text{Al}_n\text{I}_m^-) + E(\text{CH}_3\text{OH})) \quad (3.2-3)$$

Similar to  $E_B$ , the relative transition state energy is the difference between the total energy of the transition state complex,  $E(\text{CH}_3\text{OHA}l_n\text{I}_m^-)_{\text{TS}}$ , and the sum of the total energies of the cluster and methanol in their ground states. Previous studies show that clusters with a transition state energy greater than 0.10 eV above the combined energies of the separated reactants - that is, an  $E_T$  of more than 0.10 eV as calculated above - are only negligibly reactive in a gas-phase reaction chamber on the time scale of flow tube reactions.<sup>36-38</sup> Thus, this quantity was used as the deciding factor when determining whether a cluster is reactive with methanol. Since  $E_T$  is most useful in the prediction of gas-phase reactivity, the  $E_A$  (or potential barrier) was calculated to provide more widely applicable information of the reactivity of these clusters. This value is the difference between the total energy of the transition state and the total energy of the methanol-cluster complex, as shown below:

$$E_A = E(\text{CH}_3\text{OHA}l_n\text{I}_m^-)_{\text{TS}} - E(\text{CH}_3\text{OHA}l_n\text{I}_m^-)_{\text{ads}} \quad (3.2-4)$$

The activation energy is of most interest in liquid-phase reactions, in which the solvent may rapidly dissipate the binding energy. As such, the reactivity will most likely follow the Arrhenius law, with  $E_A$  serving as the activation energy.

For the final or relaxed state geometries, several arrangements were tried for each cluster in which hydrogen was bound to different aluminum atoms neighboring the reaction site, including the preferred site found in the initial step of the transition state search. The entire complex was optimized, and the lowest energy geometry resulting from this was the final state geometry. The total energy of the relaxed geometry was used to calculate the final quantity characterizing these reaction pathways: the relative relaxed state energy,  $E_R$ . Similar to  $E_B$  and  $E_T$ ,  $E_R$  is the difference between the total energy of the final state of the complex,

$E(\text{CH}_3\text{OHA}l_n\text{I}_m^-)_R$ , and the sum of the total energies of the cluster and methanol in their ground states, as seen in the following equation:

$$E_R = E(\text{CH}_3\text{OHA}l_n\text{I}_m^-)_R - (E(\text{Al}_n\text{I}_m^-) + E(\text{CH}_3\text{OH})) \quad (3.2-5)$$

In general, the relative relaxed state energy is the greatest (most negative) of all calculated values for each reaction site. Based on the complementary Lewis acid-base concept,  $E_R$  should be greatest in those cases where the hydrogen atom bonds to a Lewis base site, an aluminum atom with a large concentration of occupied frontier orbital charge density.

### 3.3 The $\text{Al}_{13}\text{I}_x^-$ (x=0 – 4) Series

The ground state structures and one higher energy isomer, as well as the charge densities of the frontier orbitals for  $\text{Al}_{13}\text{I}_x^-$  are shown in Figure 3.3.1. The attachment of ligands does little to disturb the symmetrical geometric structure of  $\text{Al}_{13}^-$ , and each cluster in this series retains an approximately icosahedral core, with iodine bonding externally. Upon examining the electronic structure, it was found that there were a number of degenerate or nearly degenerate states in the regions of the frontier orbitals. To take this into account, the charge density of all occupied orbitals close in energy to the HOMO, which will be referred to as the occupied frontier orbital charge density, was plotted in red. Similarly, the charge density of all unoccupied orbitals close in energy to the LUMO, which will be referred to as the unoccupied frontier orbital charge density, was plotted in blue. Details of which orbitals were included for each cluster are provided in Table A1 in Appendix A.

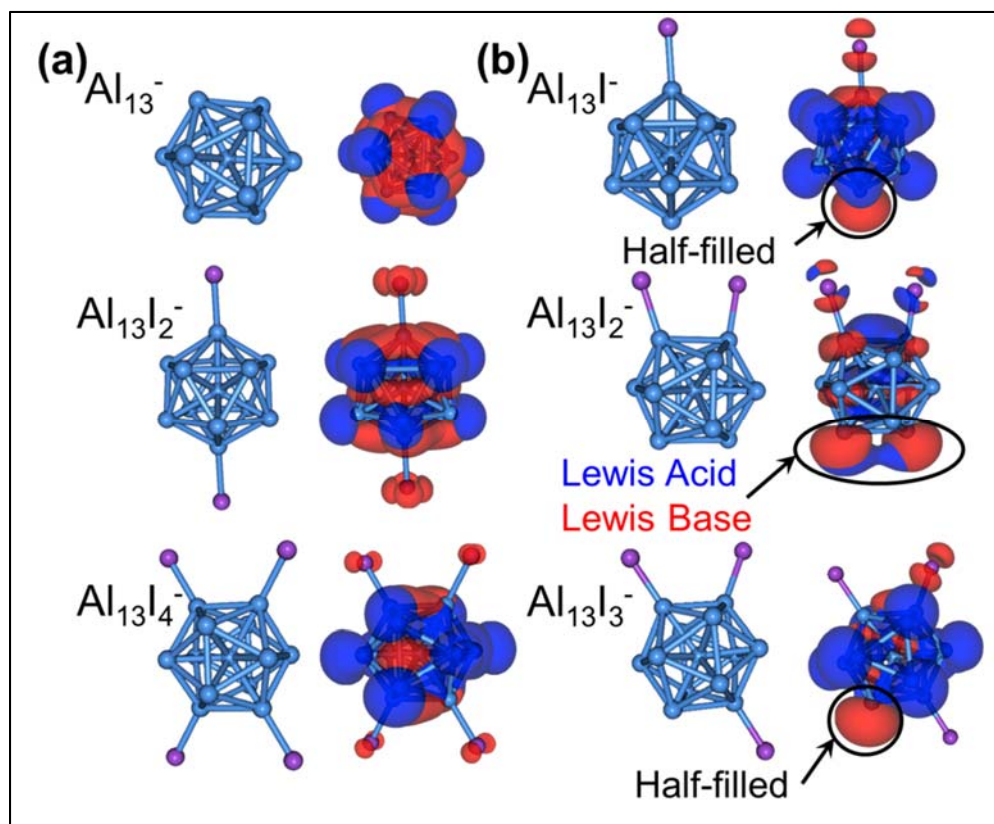


**Figure 3.3.1: Ground State Structures and Frontier Orbital Charge Densities of the  $\text{Al}_{13}\text{I}_x^-$  ( $x=0-4$ ) Series.** The ground state structures and frontier orbital charge densities of (a) the symmetrical species:  $\text{Al}_{13}^-$ ,  $\text{Al}_{13}\text{I}_2^-$ , and  $\text{Al}_{13}\text{I}_4^-$ ; and (b) the asymmetrical species:  $\text{Al}_{13}\text{I}^-$ , a higher energy isomer of  $\text{Al}_{13}\text{I}_2^-$ , and  $\text{Al}_{13}\text{I}_3^-$ . Aluminum atoms are shown in light blue and iodine atoms are shown in purple. HOMO charge density is red, while LUMO charge density is dark blue. All charge densities were generated with an isosurface value of 0.03 electrons. Figure taken from Abreu et al.<sup>115</sup>

The frontier orbital analysis did not reveal any prominent Lewis acid or Lewis base sites in  $\text{Al}_{13}^-$  or in the ground states of  $\text{Al}_{13}\text{I}_2^-$  and  $\text{Al}_{13}\text{I}_4^-$ , shown in Figure 3.3.1(a). Both occupied and unoccupied charge densities are symmetrical and diffuse, owing to the balancing of the iodine ligands. In the odd-iodine species,  $\text{Al}_{13}\text{I}^-$  and  $\text{Al}_{13}\text{I}_3^-$ , shown in Figure 3.3.1(b), one does see a concentration of occupied frontier orbital charge density on the aluminum opposite the unbalanced iodine ligand, which comes from the half-filled HOMO. The unoccupied charge density, however, still appears diffuse and symmetrically distributed about the clusters' centers. The higher energy isomer of  $\text{Al}_{13}\text{I}_2^-$ , in which both iodine atoms are placed on adjacent

aluminum atoms, shows a distinct pair of Lewis acid and Lewis base sites on the opposite side of the cluster – a potential pair of complementary active sites.

For each of the ground state geometries above, several reaction sites were chosen as described in Section 3.2, with the exception of  $\text{Al}_{13}^-$  for which all aluminum atoms are equivalent. Sites chosen included aluminum atoms with Lewis acid and Lewis base character, as well as those ligated with iodine atoms. Table 3.3-1 shows the various sites chosen and their binding energies.

**Table 3.3-1: Reaction Sites and Corresponding Binding Energies for  $\text{Al}_{13}\text{I}_x^-$ .**

Cluster	Site	BE (eV)
$\text{Al}_{13}^-$	any	0.15
$\text{Al}_{13}\text{I}^-$	LA	0.14
	LB	0.15
	I site	0.06
$\text{Al}_{13}\text{I}_2^-$	LA/HB	0.29
	LA	0.17
$\text{Al}_{13}\text{I}_2^-_{\text{adj}}$	LA/LB	0.67
$\text{Al}_{13}\text{I}_3^-$	LB	0.13
	LA/HB	0.29
	I site	0.01
$\text{Al}_{13}\text{I}_4^-$	LA/HB (top)	0.32
	LA/HB (side)	0.27
	I site	0.02

The reaction sites chosen for each cluster and their corresponding binding energies as defined in Equation (3.2-1) are given above. LA (LB) indicates that methanol bonds to a Lewis acid (base) site; HB indicates that methanol forms a hydrogen bond with a nearby iodine atom; and I site indicates that methanol bonds to an aluminum atom that is bonded to an iodine atom.

For the bare cluster, the binding energy of methanol is only 0.15 eV, owing to the diffuse nature of the unoccupied charge density – there is no concentration of LUMO density to act as a strong Lewis acid site. The addition of a single iodine atom does not improve the binding energy; the unoccupied frontier orbital is still symmetrically distributed around the core of the cluster, resulting in a Lewis acid site binding energy of only 0.14 eV. The concentration of HOMO

density that forms opposite the iodine atom has about the same binding energy as the Lewis acid site. Being half-filled, this site acts as a poor Lewis acid. The final site tested for  $\text{Al}_{13}\text{I}^-$  was the aluminum atom directly bonded to the iodine atom, denoted the I site. This site proves to have the lowest binding energy of only 0.06 eV. The second odd-iodine cluster in the series,  $\text{Al}_{13}\text{I}_3^-$ , shows the same pattern of binding energies, with the Lewis base site having a binding energy of 0.13 eV and the I site having a binding energy of 0.01 eV. The Lewis acid site on  $\text{Al}_{13}\text{I}_3^-$ , however, has a binding energy about twice that of the Lewis acid site on  $\text{Al}_{13}\text{I}^-$ , due to the formation of a hydrogen bond between a hydrogen atom on methanol and the iodine atom, which acts to stabilize the binding of methanol to the cluster.

As discussed, the addition of an even number of iodine atoms maintains the diffuse and symmetrically distributed unoccupied charge density seen in the bare and odd-iodine clusters; however, no concentration of HOMO density arises since the iodine atoms are equally balanced. For these clusters, then, only Lewis acid sites and I sites were tested. For  $\text{Al}_{13}\text{I}_2^-$ , one site has about the same Lewis acidity as the bare cluster, with a binding energy of 0.17 eV. A second Lewis acid site has a higher binding energy of 0.29 eV, again owing to a stabilizing hydrogen bond between methanol and iodine. In  $\text{Al}_{13}\text{I}_4^-$ , both Lewis acid sites, one an on-top site and one on the side of the cluster, have hydrogen-bond stabilized binding energies of 0.32 eV and 0.27 eV, respectively. The I site, as in the odd-iodine clusters, is a poor Lewis acid with a binding energy of only 0.02 eV. The binding energy is noticeably increased in the higher energy isomer of  $\text{Al}_{13}\text{I}_2^-$  with iodine atoms attached to adjacent aluminum atoms; the Lewis acid site on the opposite side of the cluster binds methanol with an energy of 0.67 eV, over four times that of the bare cluster.



While examination of occupied and unoccupied frontier orbital charge densities and calculation of the binding energies revealed certain sites as more probable reaction centers for the successful breaking of the O-H bond in methanol, the transition and relaxed states were found for all sites given in Table 3.3-1. The relative methanol-bound state, relative transition state, relative relaxed state, and activation energies were calculated for all sites as described in Section 3.2. Table 3.3-2 gives these four relative energies for the lowest energy reaction pathway, that is, the pathway with the smallest transition state energy, for each cluster.

**Table 3.3-2: Relative Energies for Reaction Pathways of  $\text{Al}_{13}\text{I}_x^-$  with Methanol**

Cluster	$E_B$ (eV)	$E_T$ (eV)	$E_R$ (eV)	$E_A$ (eV)
$\text{Al}_{13}^-$	-0.15	0.25	-0.77	0.40
$\text{Al}_{13}\text{I}^-$	-0.14	0.23	-1.34	0.37
$\text{Al}_{13}\text{I}_2^-$	-0.29	0.20	-0.85	0.49
$\text{Al}_{13}\text{I}_2^-_{\text{adj}}$	-0.67	-0.42	-2.14	0.25
$\text{Al}_{13}\text{I}_3^-$	-0.29	0.21	-1.34	0.50
$\text{Al}_{13}\text{I}_4^-$	-0.27	0.26	-0.72	0.53

The relative methanol-bound state,  $E_B$ , relative transition state,  $E_T$ , relative relaxed state,  $E_R$ , and activation,  $E_A$ , energies of the lowest energy reaction pathways of  $\text{Al}_{13}\text{I}_x^-$  with methanol. Adapted from Table 1 in Abreu et al.<sup>115</sup>

Note again that the relative energy of the methanol-bound state,  $E_B$ , is simply the negative of the binding energy, BE. Comparing the BE values in Table 3.3-1 with the  $E_B$  values in Table 3.3-2, one can see that the lowest energy reaction pathways begin as predicted with the binding of methanol to a Lewis acid site, whether that site is a particularly strong Lewis acid or not.

To first explore the effect of adding a single iodine atom on the reactivity of  $\text{Al}_{13}^-$ , Figure 3.3.2 shows the lowest energy reaction pathways of  $\text{Al}_{13}^-$  and  $\text{Al}_{13}\text{I}^-$  with methanol. As discussed,  $\text{Al}_{13}^-$  is a poor Lewis acid, with binding energy of only 0.15 eV, due to the even charge density distribution of the cluster. In Figure 3.3.2(a), the reaction pathway shows that the reaction of  $\text{Al}_{13}^-$  with methanol has a positive relative transition state energy,  $E_T$ , of 0.25 eV, indicating that this reaction will not occur. Similarly, as shown in Table 3.3-2, the high activation energy,  $E_A$ , of

0.40 eV confirms stability of this cluster toward methanol. This  $E_A$  will be used as the reference for the remaining clusters in the series.

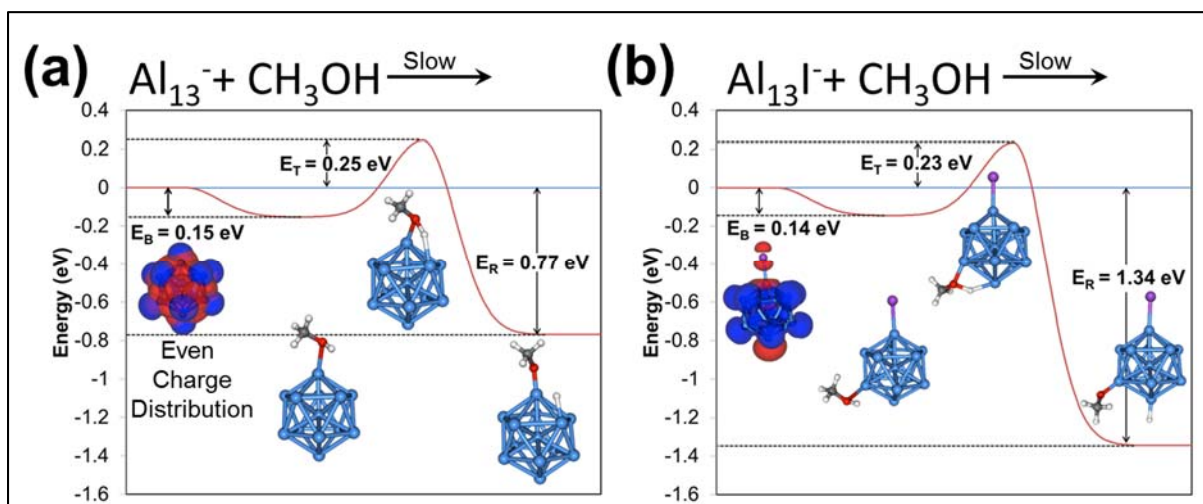


**Figure 3.3.2: Lowest Energy Reaction Pathways of  $\text{Al}_{13}^-$  and  $\text{Al}_{13}\text{I}^-$  with Methanol.** The above figure demonstrates the effect that the addition of a single iodine atom makes to the reactivity of  $\text{Al}_{13}^-$ . The reaction pathways with the lowest transition state energy for (a)  $\text{Al}_{13}^-$  and (b)  $\text{Al}_{13}\text{I}^-$  are shown. The interpolated reaction pathway is shown as a red line, and the absolute values of  $E_B$  (or  $BE$ ),  $E_T$ , and  $E_R$  are indicated. The occupied (red) and unoccupied (blue) frontier orbital charge densities are shown on the ground state structure, and the geometries of the methanol-bound state, transition state, and final state are pictured with aluminum in blue, iodine in purple, oxygen in red, carbon in gray, and hydrogen in white. Adapted from Figure 2 of Abreu et al.<sup>115</sup>

In Figure 3.3.2(b), one can see that the reaction site with the lowest  $E_T$  for  $\text{Al}_{13}\text{I}^-$  is a Lewis acid site on the core, with the hydrogen atom eventually binding to the half-filled HOMO site exactly opposite the iodine ligand. The binding energy at this site is about the same as for the bare  $\text{Al}_{13}^-$  cluster, again due to the diffuse and symmetrical distribution of unoccupied frontier orbital charge density. The  $E_T$  is also similar to the bare cluster, only dropping to 0.23 eV, so this cluster is also unreactive. This is further shown by the  $E_A$  of 0.37 eV, which again shows no significant improvement over that of the bare cluster. The only difference between the reactions of the bare and iodized cluster is the relative relaxed state energy,  $E_R$ . In the case of  $\text{Al}_{13}\text{I}^-$ , it is almost twice as great as it is in the case of  $\text{Al}_{13}^-$ . This could be caused by the concentration of

HOMO density in  $\text{Al}_{13}\text{I}^-$  on the aluminum atom opposite the iodine, which receives the hydrogen atom. Despite only being half-filled, this site acts as a better Lewis base than any site on the  $\text{Al}_{13}^-$  cluster.

The addition of one iodine atom does not act to make the cluster reactive, so we will now look at the addition of two iodine atoms. Figure 3.3.3 shows the lowest energy reaction pathways with methanol of both  $\text{Al}_{13}\text{I}_2^-$  isomers: the ground state with balanced iodine ligands and the higher energy structure with iodine ligands on adjacent aluminum atoms.

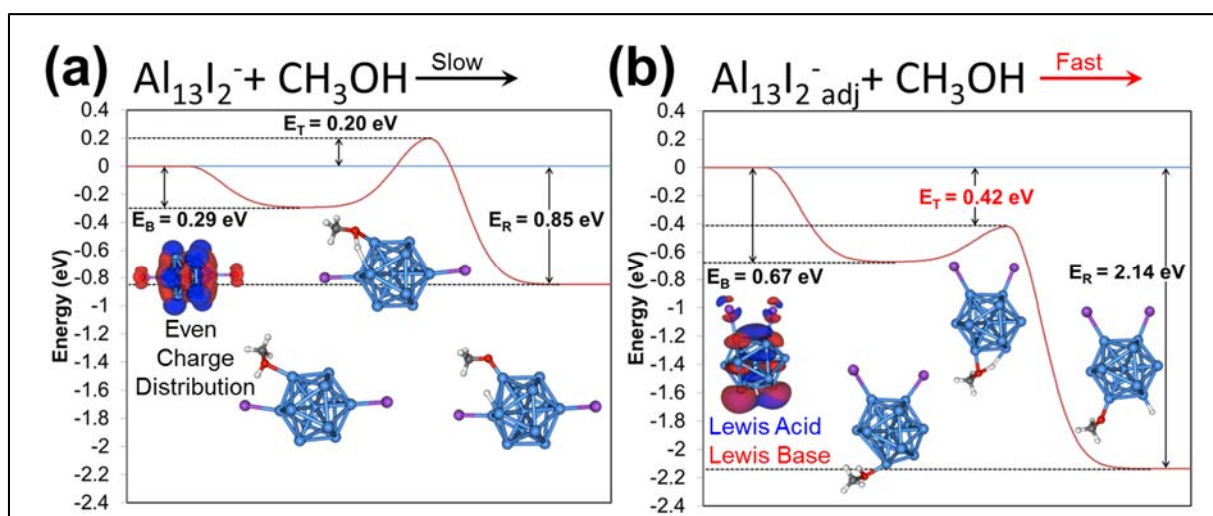


**Figure 3.3.3: Lowest Energy Reaction Pathways of Two Isomers of  $\text{Al}_{13}\text{I}_2^-$  with Methanol.** The above figure demonstrates the effect of ligand placement. The lowest energy reaction pathways are given for (a) the ground state of  $\text{Al}_{13}\text{I}_2^-$  in which the two iodine ligands are opposite each other, and (b) a higher energy isomer of  $\text{Al}_{13}\text{I}_2^-$ , in which the two iodine ligands are placed on adjacent aluminum atoms. The interpolated reaction pathway is shown as a red line, and the absolute values of  $E_B$ ,  $E_T$ , and  $E_R$  are indicated. The occupied (red) and unoccupied (blue) frontier orbital charge densities are shown on the ground state structure, and the geometries of the methanol-bound state, transition state, and final state are pictured with aluminum in blue, iodine in purple, oxygen in red, carbon in gray, and hydrogen in white. Adapted from Figure 2 of Abreu et al.<sup>115</sup>

Despite being a slightly better Lewis acid than both the bare  $\text{Al}_{13}^-$  cluster and  $\text{Al}_{13}\text{I}^-$ , as shown in Figure 3.3.3(a),  $\text{Al}_{13}\text{I}_2^-$  in its ground state is unreactive with methanol, with a positive  $E_T$  of 0.20 eV.  $E_R$  is also low, similar to that of  $\text{Al}_{13}^-$ , indicating that there is no adequate Lewis base site to

which hydrogen can bind. Finally, the  $E_A$  of 0.49 eV is even higher than that of the bare cluster, further evidence that the cluster is unreactive. This can be attributed to the symmetrical distribution of the charge density.

As previously shown, the placement of the two iodine ligands on adjacent aluminum atoms results in the formation of complementary active sites on the opposite side of the cluster. Consequently, one can see in Figure 3.3.3(b) that this cluster does react with methanol. This is indicated by the negative  $E_T$ , -0.42 eV, which shows that the O-H bond can be broken. Finally, the  $E_R$  of -2.14 eV suggests that hydrogen is able to bind strongly to a Lewis base site adjacent to the Lewis acid site. This cluster also has the lowest  $E_A$  in this series, at only 0.25 eV. While  $\text{Al}_{13}\text{I}_2^-_{\text{adj}}$  is a higher energy isomer, its reactivity with methanol is evidence that complementary Lewis acid-base sites can be induced in unreactive clusters, like  $\text{Al}_{13}^-$ , by appropriately attaching electronegative ligands. The higher energy isomer is unlikely to exist in experiment, but the effect of ligand placement uncovered in the theoretical study of  $\text{Al}_{13}\text{I}_2^-_{\text{adj}}$  can be extended to other cluster systems and to the design of cluster-assembled materials.

As the relative energies in Table 3.3-2 show, the lowest energy reaction pathways for  $\text{Al}_{13}\text{I}_3^-$  and  $\text{Al}_{13}\text{I}_4^-$  are very similar to those of  $\text{Al}_{13}\text{I}^-$  and  $\text{Al}_{13}\text{I}_2^-$  in their ground states, respectively. Neither cluster is a particularly good Lewis acid, and the high  $E_T$  and  $E_A$  values for both clusters show that neither will react with methanol. Although  $\text{Al}_{13}\text{I}_3^-$  is a better Lewis acid than its odd-iodine counterpart  $\text{Al}_{13}\text{I}^-$  – perhaps owing to the electron-withdrawing effects of several iodine atoms compared to just one – it shows no enhanced reactivity over  $\text{Al}_{13}\text{I}^-$ ; the unoccupied frontier orbital charge density is still too diffuse, and the concentrated HOMO site cannot act fully as a Lewis base, being only half-filled. Looking to the even-iodine clusters,  $\text{Al}_{13}\text{I}_4^-$  is actually less reactive than  $\text{Al}_{13}\text{I}_2^-$ , and this can again be attributed to the symmetrical

frontier orbital charge densities. No prominent Lewis acid-base pairs are induced by the addition of the iodine ligands, since they add to the cluster in a symmetrical manner. The lowest energy reaction pathways for  $\text{Al}_{13}\text{I}_3^-$  and  $\text{Al}_{13}\text{I}_4^-$  are shown in Figure A1 in Appendix A.

### 3.4 The $\text{Al}_{14}\text{I}_y^-$ ( $y=0-5$ ) Series

Figure 3.4.1 presents the ground state structures of  $\text{Al}_{14}\text{I}_y^-$  ( $y = 0-5$ ) and their corresponding frontier orbital charge densities.

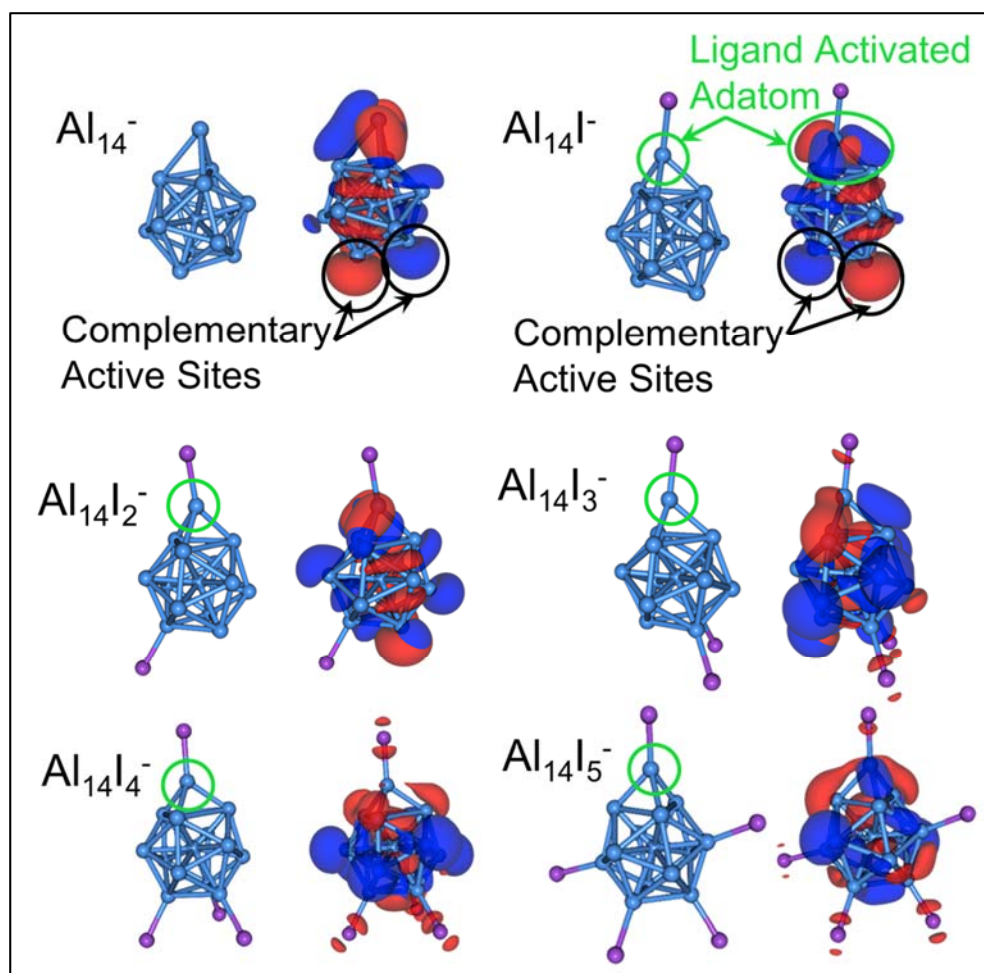


**Figure 3.4.1: Ground State Structures and Frontier Orbital Charge Densities of  $\text{Al}_{14}\text{I}_y^-$ .** The ground state structures of  $\text{Al}_{14}\text{I}_y^-$  ( $y=0-5$ ) are shown with aluminum atoms in light blue and iodine atoms in purple. Occupied frontier orbital charge density is shown in red, while unoccupied frontier orbital charge density is shown in blue. Taken from Figure 3 of Abreu et al.<sup>115</sup>

In the same manner as with  $\text{Al}_{13}\text{I}_x^-$ , the occupied frontier orbital density includes the HOMO and all orbitals lying close in energy and the unoccupied frontier orbital density includes the LUMO and all orbitals lying close in energy. The orbitals used for each cluster are given in Table A2 in Appendix A. The general geometry of the series is that of an icosahedral  $\text{Al}_{13}^-$  cluster with an adatom defect – the fourteenth atom sits atop the  $\text{Al}_{13}^-$  core. The iodine ligands attach at external sites, with the first iodine bonding to the adatom, and any additional iodine atoms bonding to aluminum atoms on the opposite side of the cluster. As shown in Figure 1.4.1, the adatom itself induces sites of concentrated occupied and unoccupied frontier orbital charge density on the opposite side of the  $\text{Al}_{14}^-$  cluster, forming a complementary Lewis acid-base pair. This is also apparent in  $\text{Al}_{14}\text{I}^-$ . The addition of an iodine atom to the adatom creates a concentration of occupied and unoccupied charge density near the adatom, creating another possible reaction site on the remaining clusters in this series.

For each cluster in the  $\text{Al}_{14}\text{I}_y^-$  series, the chosen reaction sites and the calculated binding energies are given in Table 3.4-1. One can immediately see that the binding energies are generally greater than those found in the  $\text{Al}_{13}\text{I}_x^-$  series, meaning the adatom perturbs the charge density enough to create stronger active sites by concentrating the occupied or unoccupied frontier orbital charge density to certain areas on the cluster. In addition to the adatom itself, which has a binding energy of 0.30 eV,  $\text{Al}_{14}^-$  has active sites on the core: a Lewis acid site with a binding energy of 0.36 eV and a Lewis base site with a binding energy of 0.34 eV. All three chosen sites are better Lewis acids than any site on the bare  $\text{Al}_{13}^-$  cluster. The addition of an iodine atom to the  $\text{Al}_{14}^-$  cluster only enhances the Lewis acidity of these sites; the binding energies of the Lewis acid and Lewis base sites increase to 0.43 eV and 0.41 eV, respectively, and the binding energy of the now iodine-ligated adatom site increases to 0.55 eV.

**Table 3.4-1: Reaction Sites and Corresponding Binding Energies for  $\text{Al}_{14}\text{I}_y^-$ .**

Cluster	Site	BE (eV)
$\text{Al}_{14}^-$	adatom	0.30
	LB (core)	0.34
	LA (core)	0.36
$\text{Al}_{14}\text{I}^-$	adatom	0.55
	LA (core)	0.43
	LB (core)	0.41
$\text{Al}_{14}\text{I}_2^-$	adatom	0.41
	I site	0.08
	LA/LB (core)	0.45
$\text{Al}_{14}\text{I}_3^-$	adatom	0.44
	I site	0.16
	LA (core)	0.58
$\text{Al}_{14}\text{I}_4^-$	adatom	0.40
	I site/LA	0.02
	LB (core)	0.33
$\text{Al}_{14}\text{I}_5^-$	adatom	0.38
	LA/HB (core)	0.33
	I site	0.11

The reaction sites chosen for each cluster and their corresponding binding energies as defined in Equation (3.2-1) are given above. LA (LB) indicates that methanol bonds to a Lewis acid (base) site; HB, that methanol forms a hydrogen bond with a nearby iodine atom; adatom, that methanol bonds to the adatom; I site, that methanol bonds to an aluminum atom that is bonded to an iodine atom on the core of the cluster, not the adatom; and core, that whichever site indicated is on the core of the cluster.

The ligated adatom site maintains a high binding energy, hovering around 0.40 eV, in the remaining clusters in the series. For clusters with more than one iodine, the iodine-ligated aluminum atom on the core of the cluster, indicated by I site, shows low Lewis acidity, with binding energies less than 0.20 eV, and in the case of  $\text{Al}_{14}\text{I}_4^-$ , as low as 0.02 eV. This is similar to the I sites tested in  $\text{Al}_{13}\text{I}_x^-$ , which were also poor Lewis acids. The remaining sites tested were Lewis acid or Lewis base sites located on the core, all of which have high binding energies, including the Lewis acid site on the core of  $\text{Al}_{14}\text{I}_3^-$ , which has the highest binding energy, 0.58

eV, of all reaction sites tested in this series. This is due to the formation of a hydrogen bond between methanol and the iodine ligand.

The transition state and relaxed state geometries were found as described in Section 3.2 for all the reaction sites listed in Table 3.4-1. The relative methanol-bound state, relative transition state, relative relaxed state, and activation energies were calculated for each reaction site as described in Section 3.2, and are shown for selected reaction pathways in Table 3.4-2. This table includes the lowest energy reaction pathway for each cluster (shaded) as well as additional reaction pathways that are of interest in understanding the role of the iodine ligand or exploring the differences in reactivity between various active sites.

**Table 3.4-2: Relative Energies for Reaction Pathways of  $Al_{14}I_y^-$  with Methanol**

Cluster	$E_B$ (eV)	$E_T$ (eV)	$E_R$ (eV)	$E_A$ (eV)
$Al_{14}^-$ act	-0.36	-0.12	-1.80	0.24
$Al_{14}I^-$ adatom	-0.30	0.22	-0.69	0.52
$Al_{14}I_2^-$ adatom	-0.55	-0.12	-1.80	0.43
$Al_{14}I_3^-$ act	-0.43	-0.29	-2.30	0.14
$Al_{14}I_3^-$ adatom	-0.44	-0.20	-0.84	0.24
$Al_{14}I_3^-$ site	-0.16	0.36	-0.90	0.52
$Al_{14}I_3^-$ core	-0.58	0.13	-0.78	0.71
$Al_{14}I_2^-$ adatom	-0.41	-0.23	-1.12	0.18
$Al_{14}I_4^-$ adatom	-0.40	-0.17	-0.95	0.23
$Al_{14}I_5^-$ adatom	-0.38	-0.18	-1.35	0.20

The relative methanol-bound state,  $E_B$ , relative transition state,  $E_T$ , relative relaxed state,  $E_R$ , and activation,  $E_A$ , energies of selected reaction pathways of  $Al_{14}I_y^-$  with methanol. Adapted from Table 2 of Abreu et al.<sup>115</sup>

Comparing the binding energies in Table 3.4-1 to the relative methanol-bound energies in Table 3.4-2, one can see that in most cases the lowest energy reaction pathway corresponds to the greatest binding energy, and hence occurs at the site of greatest Lewis acidity. However, this is not true for all clusters in the series, and not all sites that have high binding energies actually succeed in breaking the O-H bond in methanol. This is explored in Figure 3.4.2, which shows the



results of the reaction of  $\text{Al}_{14}\text{I}_3^-$  with methanol at three different active sites: the ligated adatom, a ligated aluminum atom on the core, and an all-metal Lewis acid site on the core.

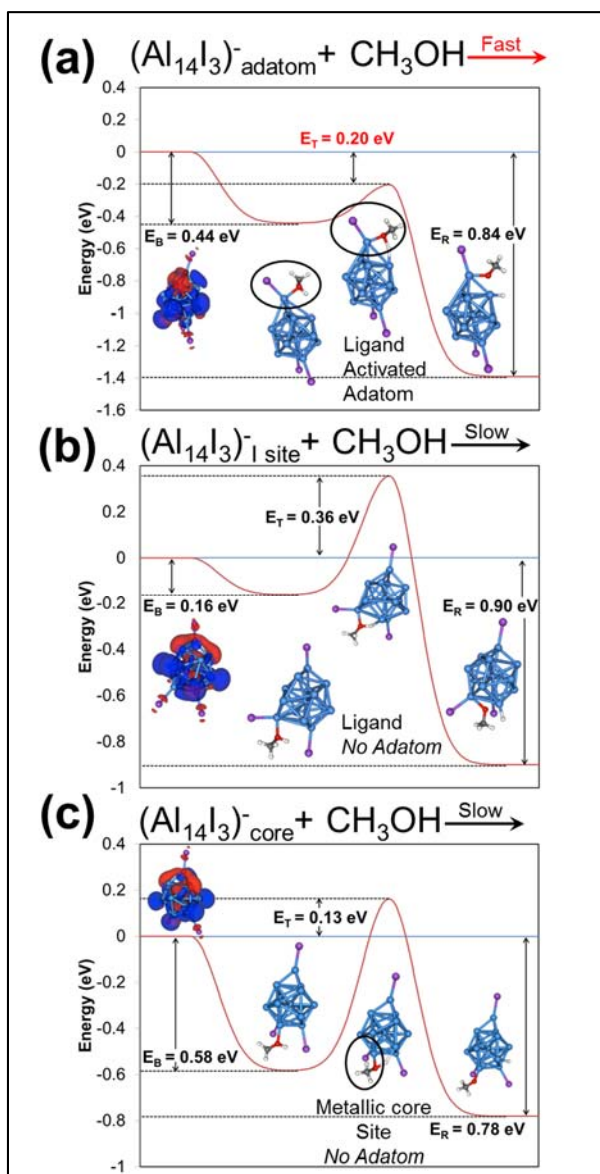


**Figure 3.4.2: Reaction Pathways of  $\text{Al}_{14}\text{I}_3^-$  with Methanol.** This figure shows the variable reactivity found at different reaction sites on the  $\text{Al}_{14}\text{I}_3^-$  cluster. The reaction pathways of  $\text{Al}_{14}\text{I}_3^-$  at (a) the ligated adatom site, (b) a ligated aluminum site on the core, and (c) an all-metal site on the core are shown. The interpolated reaction pathway is shown as a red line, and the absolute values of  $E_B$  (or  $BE$ ),  $E_T$ , and  $E_R$  are indicated. The occupied (red) and unoccupied (blue) frontier orbital charge densities are shown on the ground state structure, and the geometries of the methanol-bound state, transition state, and final state are pictured with aluminum in blue, iodine in purple, oxygen in red, carbon in gray, and hydrogen in white. Adapted from Figure 2 of Abreu et al.<sup>115</sup>

As shown in Figure 3.4.2(a),  $\text{Al}_{14}\text{I}_3^-$  will react with methanol at the ligated adatom site. The ligated adatom is a decent Lewis acid site, and the  $E_T$  of -0.20 eV shows that the O-H bond will be broken. Furthermore, the  $E_A$  is quite low at 0.24 eV, on par with the reactive  $\text{Al}_{13}\text{I}_2^-$  cluster with adjacent iodine ligands. Interestingly, as shown in Figure 3.4.2(b) and (c),  $\text{Al}_{14}\text{I}_3^-$  does not react with methanol at any other site. The ligated aluminum atom on the core, (b), is a poor Lewis acid and has the highest  $E_T$ , 0.36 eV, of all the lowest energy reaction pathways presented in either series. The all-metal site on the core, (c), has the highest binding energy in the series, but is still unreactive with an  $E_T$  of 0.13 eV. These sites on the core, whether ligated or not, may be unreactive due to steric constraints.  $\text{Al}_{14}\text{I}_2^-$ ,  $\text{Al}_{14}\text{I}_4^-$ , and  $\text{Al}_{14}\text{I}_5^-$  all show the same reactivity patterns as  $\text{Al}_{14}\text{I}_3^-$ ; the clusters react with methanol at the ligated adatom site, with negative  $E_T$  and low  $E_A$ , but not at any other site. This is especially remarkable for  $\text{Al}_{14}\text{I}_3^-$  and  $\text{Al}_{14}\text{I}_5^-$ , which as previously discussed, are both closed-shell species stable to  $\text{O}_2$ . The lowest energy reaction pathways of  $\text{Al}_{14}\text{I}_2^-$ ,  $\text{Al}_{14}\text{I}_4^-$ , and  $\text{Al}_{14}\text{I}_5^-$  are given in Figure A2 in Appendix A.

The fact that  $\text{Al}_{14}\text{I}_y^-$  ( $y = 2-5$ ) clusters are only reactive with methanol at the adatom site begs the question: Is the iodine ligand necessary to induce reactivity, or is the bare adatom sufficient for creating the active site? To examine this, the selected reaction pathways of bare  $\text{Al}_{14}^-$  and  $\text{Al}_{14}\text{I}^-$  are shown in Figure 3.4.3.

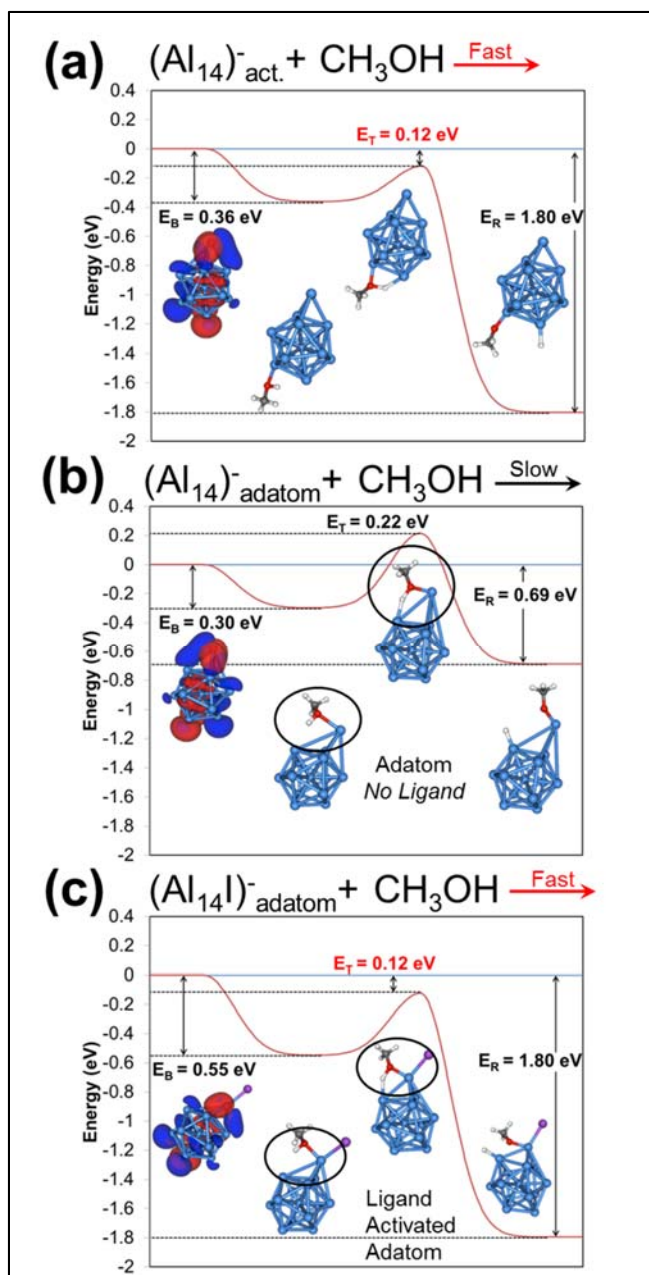


**Figure 3.4.3: Selected Reaction Pathways of  $\text{Al}_{14}^-$  and  $\text{Al}_{14}\text{I}^-$ .** This figure shows the effect of adding a ligand to the adatom of  $\text{Al}_{14}^-$ . The reaction pathways of  $\text{Al}_{14}^-$  with methanol at (a) a Lewis acid site opposite the adatom and (b) the adatom, as well as (c) the reaction pathway of  $\text{Al}_{14}\text{I}^-$  at the ligated adatom site are shown. The interpolated reaction pathway is shown as a red line, and the absolute values of  $E_B$ ,  $E_T$ , and  $E_R$  are indicated. The occupied (red) and unoccupied (blue) frontier orbital charge densities are shown on the ground state structure, and the geometries of the methanol-bound state, transition state, and final state are pictured with aluminum in blue, iodine in purple, oxygen in red, carbon in gray, and hydrogen in white. Adapted from Figure 2 of Abreu et al.<sup>115</sup>

As Figure 3.4.3(a) shows, the bare  $\text{Al}_{14}^-$  cluster reacts with methanol at the aforementioned complementary active sites on the cluster opposite the adatom. Just as in  $\text{Al}_{13}\text{I}_2^-$  with adjacent iodine atoms, the oxygen of methanol bonds to the fairly strong Lewis acid site on the core of the  $\text{Al}_{14}^-$  cluster, the O-H bond breaks with a  $E_T$  of -0.12 eV, and hydrogen binds to the adjacent Lewis base site, with a  $E_R$  of -1.80 eV. The adatom site, shown in (b), is about as strong a Lewis acid as the site on the core, but is unreactive with methanol – the  $E_T$  is 0.22 eV. The  $E_R$  is also quite high at -0.69 eV. While the addition of the adatom to the  $\text{Al}_{13}^-$  cluster makes the resulting  $\text{Al}_{14}^-$  cluster reactive through geometric distortion of the charge density, the adatom itself is not reactive.

Comparison of the binding energies of  $\text{Al}_{14}^-$  and  $\text{Al}_{14}\text{I}^-$  demonstrates that the addition of an iodine ligand to the  $\text{Al}_{14}^-$  cluster at the adatom site nearly doubles its Lewis acidity. Now looking at Figure 3.4.3(c), one can see that the ligated adatom is consequently reactive with methanol, having an  $E_T$  of -0.12 eV. This site also has a lower  $E_R$  of -1.80 eV. By comparing the reactivity of  $\text{Al}_{14}^-$  and  $\text{Al}_{14}\text{I}^-$ , it becomes clear that the adatom only becomes reactive when a ligand is attached; this active site can be referred to as a ligand-activated adatom. It should be noted that the adatom is not the site of the lowest reaction pathway for  $\text{Al}_{14}\text{I}^-$ , which has a lower energy transition state at a Lewis acid site on the opposite side of the cluster, as shown in Table 3.4-2; however, it has already been shown that the remaining clusters react only at this ligand-activated adatom.

### 3.5 Discussion

Through study of the reactivity of the  $\text{Al}_{13}\text{I}_x^-$  and  $\text{Al}_{14}\text{I}_y^-$  series with methanol, it was shown that ligands, usually thought of as protecting groups, can also be used as activating groups. Overall, the ground states of  $\text{Al}_{13}\text{I}_x^-$  are stable to methanol due to the diffuse and

generally symmetrical frontier orbital charge densities. Despite addition of electronegative ligands, the highly symmetrical icosahedral core of this series generally prevents distortion in the charge densities, meaning no prominent complementary Lewis acid-base sites are generated. With the addition of an adatom, the  $\text{Al}_{13}^-$  core does become reactive, as the charge density is distorted on the opposite side of the cluster. The adatom of the  $\text{Al}_{14}^-$  cluster, however, does not react with methanol. It is only by ligation with electronegative iodine that the adatom becomes activated. The adatom site maintains its reactivity with methanol throughout the series tested, even as the sites on the opposite side of the cluster become unreactive with the addition of iodine atoms. Most notably, the closed-shell species  $\text{Al}_{14}\text{I}_3^-$  and  $\text{Al}_{14}\text{I}_5^-$  will react with methanol at the ligand-activated adatom site. Overall, the hypothesis that induction of complementary Lewis acid-base sites capable of breaking the O-H bond in methanol was possible through ligation with electronegative iodine was confirmed, but we also found unexpected behavior in the form of the ligand-activated adatom.

### 3.6 Experimental Confirmation

Our collaborators in the Castleman Group at Pennsylvania State University experimentally produced the  $\text{Al}_n\text{I}_x^-$  clusters and reacted them with methanol in a fast-flow tube apparatus. The experimental setup was similar to that of the oxygen etching experiment previously mentioned,<sup>40</sup> except  $\text{CH}_3\text{OH}$  was used instead of  $\text{O}_2$ . Briefly, aluminum clusters are produced by laser ablation of an aluminum rod, known as a laser vaporization (LaVa) source. These  $\text{Al}_n^-$  clusters are introduced into the fast-flow tube apparatus with the carrier gas helium at 8000 standard cubic centimeters per minute (sccm). The fast-flow tube is equipped with two reaction gas inlets (RGIs) through which reactants can be added to the aluminum clusters. In this case,  $\text{I}_2$  gas produced through sublimation is introduced to generate  $\text{Al}_n\text{I}_m^-$  clusters. Subsequently, methanol

(MeOH) is introduced (in this case at a rate of 20 sccm) to the  $\text{Al}_n\text{I}_m^-$  clusters. The products of this reaction were analyzed via quadrupole mass spectrometry. Figure 3.6.1 shows the mass spectra of  $\text{Al}_n\text{I}_m^-$  before and after reaction with methanol. (Note that the experimental collaborators use the designation  $\text{Al}_n\text{I}_x^-$  instead of  $\text{Al}_n\text{I}_m^-$ ).

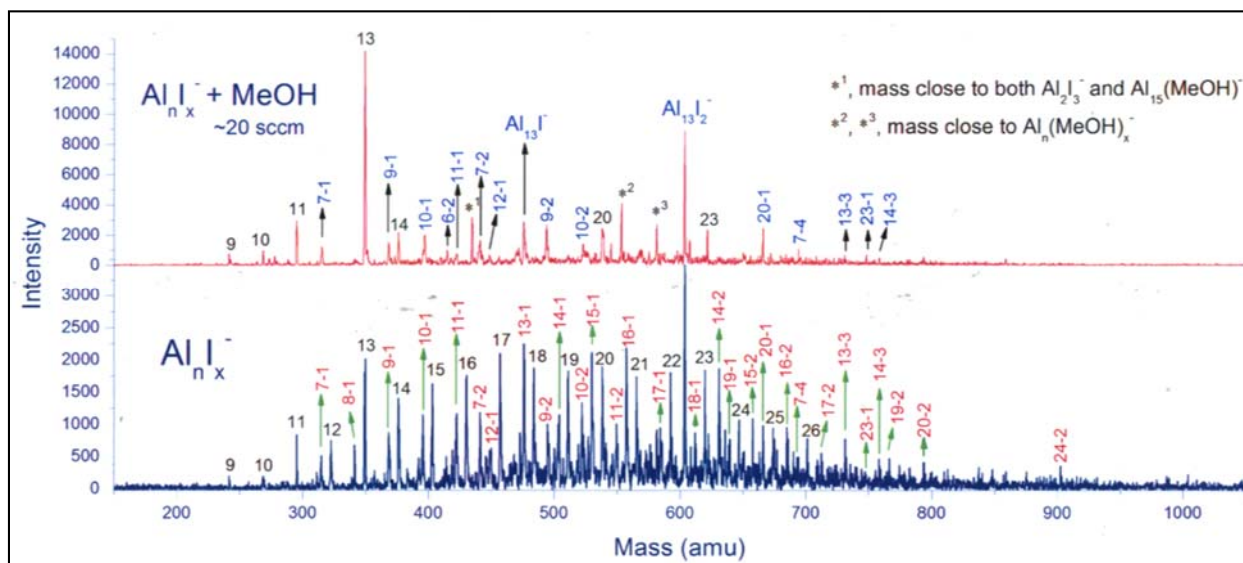


**Figure 3.6.1: Mass spectra of  $\text{Al}_n\text{I}_x^-$  before and after reaction with methanol.** The bottom spectrum shows the intensities of  $\text{Al}_n\text{I}_x^-$  units before reaction with  $\text{CH}_3\text{OH}$ , while the top shows the intensities after the reaction. Peaks are labeled to indicate the number of Al and I atoms present. Intensity is measured in arbitrary units. Note that the scales for each spectrum differ.

From the mass spectra, it is clear that  $\text{Al}_{13}^-$ ,  $\text{Al}_{13}\text{I}^-$ ,  $\text{Al}_{13}\text{I}_2^-$ , and  $\text{Al}_{13}\text{I}_3^-$  survive the reaction with methanol, as predicted by theoretical results. No  $\text{Al}_{13}\text{I}_4^-$  appears to have been initially present. On the other hand, there is no  $\text{Al}_{14}\text{I}^-$  or  $\text{Al}_{14}\text{I}_2^-$  left after the reaction, despite there being appreciable amounts of these clusters present in the first spectrum. Additionally,  $\text{Al}_{14}\text{I}_3^-$  is reduced to a nearly negligible intensity after reaction with methanol. Contrary to our predictions,  $\text{Al}_{14}^-$  did not completely react away during this experiment, however, previous experiments of this type showed that  $\text{Al}_{14}^-$  does react with methanol.<sup>38</sup> Thus, this experiment confirms what we showed theoretically; the  $\text{Al}_{13}\text{I}_x^-$  series is stable to reaction with methanol, while the  $\text{Al}_{14}\text{I}_y^-$  series, even those clusters with closed-shell electronic configurations, is not.

# 4 Silicon Encapsulated Transition Metal Clusters

## 4.1 Overview

The purpose of this study is to revisit the applicability of the electronic principles that have been used to describe the stability of  $\text{TMSi}_n$  clusters – specifically, the CNFEG model and the 18-electron rule. To do this, careful calculations of the ground state geometries and molecular orbital analyses were carried out on  $\text{CrSi}_n$  and  $\text{WSi}_n$  ( $n=6-16$ ). Before doing so, a functional, which approximates the electron exchange and correlation within density functional theory, was chosen for the calculations. The process by which this was done and the results are described in Section 4.2. A brief section describing the calculation of energetic properties used to characterize these clusters follows in Section 4.3. Ground state structures of  $\text{CrSi}_n$  ( $n=6-16$ ) and their properties are presented in Section 4.4.1, and the molecular orbital analyses of select clusters in this series is given in Section 4.4.2. In Section 4.5, the study is extended to  $\text{WSi}_n$  ( $n=6-16$ ) and the energetic and brief molecular orbital analysis results are compared to those obtained for  $\text{CrSi}_n$ . A portion of this work has been published in the Journal of Physical Chemistry Letters.<sup>116</sup>

## 4.2 Choosing a Functional

While aluminum clusters are accurately treated using the PBE functional, as several photoelectron spectroscopy experiments confirm, theoretical studies of silicon encapsulated transition metal clusters have employed a variety of functionals. Some studies used LDA or GGA functionals, especially PBE and PW91, since these are the most computationally inexpensive.<sup>79,81,82,84,90</sup> Other studies used hybrid functionals, especially B3LYP or B3PW91.<sup>81,83,89,91,117,118</sup> One study by Kumar et al. utilized both hybrid B3PW91 and GGA PBE; the hybrid functional was used for geometry optimization, while PBE was used to calculate

HOMO-LUMO gaps, making comparison with previous studies possible. Consequently, this study showed that the properties of these clusters are very sensitive to the functional used in the calculations.<sup>89</sup>

In their study of  $\text{CrSi}_n$  ( $n=11-14$ ), Khanna et al. compared the theoretically calculated VDE and ADE to experimental photoelectron spectroscopy results to validate their theoretical method, which employed the PBE functional for exchange and correlation.<sup>79</sup> The experiment, however, tested only  $\text{CrSi}_n^-$  ( $n=9-12$ ), so only the values for  $\text{CrSi}_{11}$  and  $\text{CrSi}_{12}$  were verifiable. No comprehensive comparison of theoretical and experimental results over a larger size range has been attempted. Recently, Kong et al. have produced photoelectron spectra for chromium-doped silicon clusters,  $\text{CrSi}_n^-$  ( $n=3-12$ ).<sup>119</sup> The results of this work are shown in Figure 4.2.1. To make contact with these experiments, the ground state structures of  $\text{CrSi}_n^-$  ( $n=6-12$ ) were found using two different functionals: the gradient-corrected PBE functional and the hybrid B3LYP functional. These two functionals were chosen because they have been the most used in the literature, and because they are both typical examples of GGA and hybrid functionals. Geometries were built from the literature<sup>71,72,77,79,81-84,89,90,119,120</sup> and optimized with PBE and B3LYP as described in Chapter 2. The ground states and low-lying structures within 0.20 eV of the ground state are shown for PBE and B3LYP in Figure 4.2.2 and Figure 4.2.3, respectively.



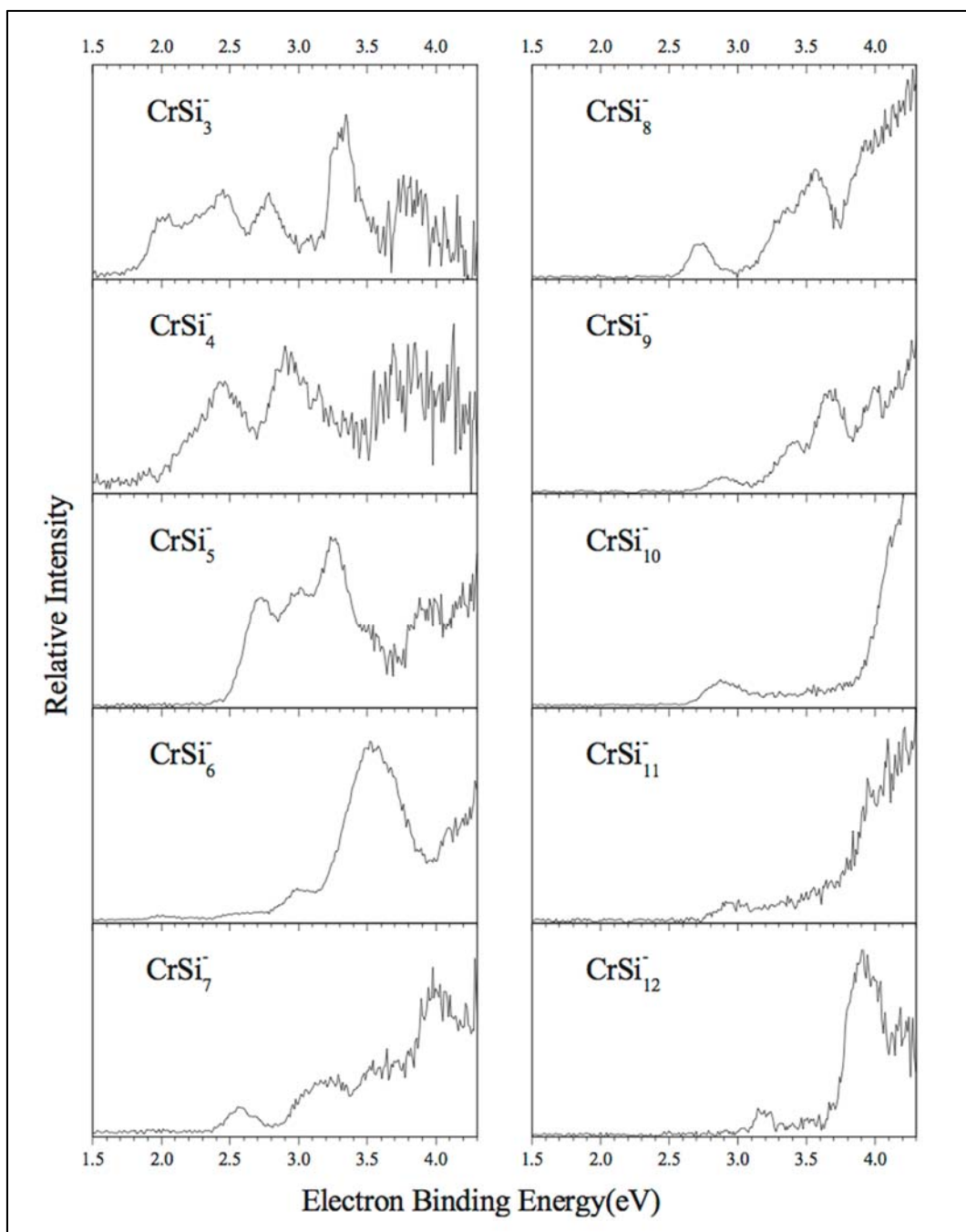


**Figure 4.2.1: Photoelectron Spectra of  $\text{CrSi}_n^-$  ( $n=3-12$ ).** This figure, taken from Kong, et al.,<sup>119</sup> shows the photoelectron spectra for anionic  $\text{CrSi}_n$  clusters with 3 through 12 silicon atoms obtained with 266 nm photons. We provide this figure to compare our theoretical results to these experimental ones, but note that we did not calculate spectra for  $\text{CrSi}_n^-$  ( $n=3-5$ ).

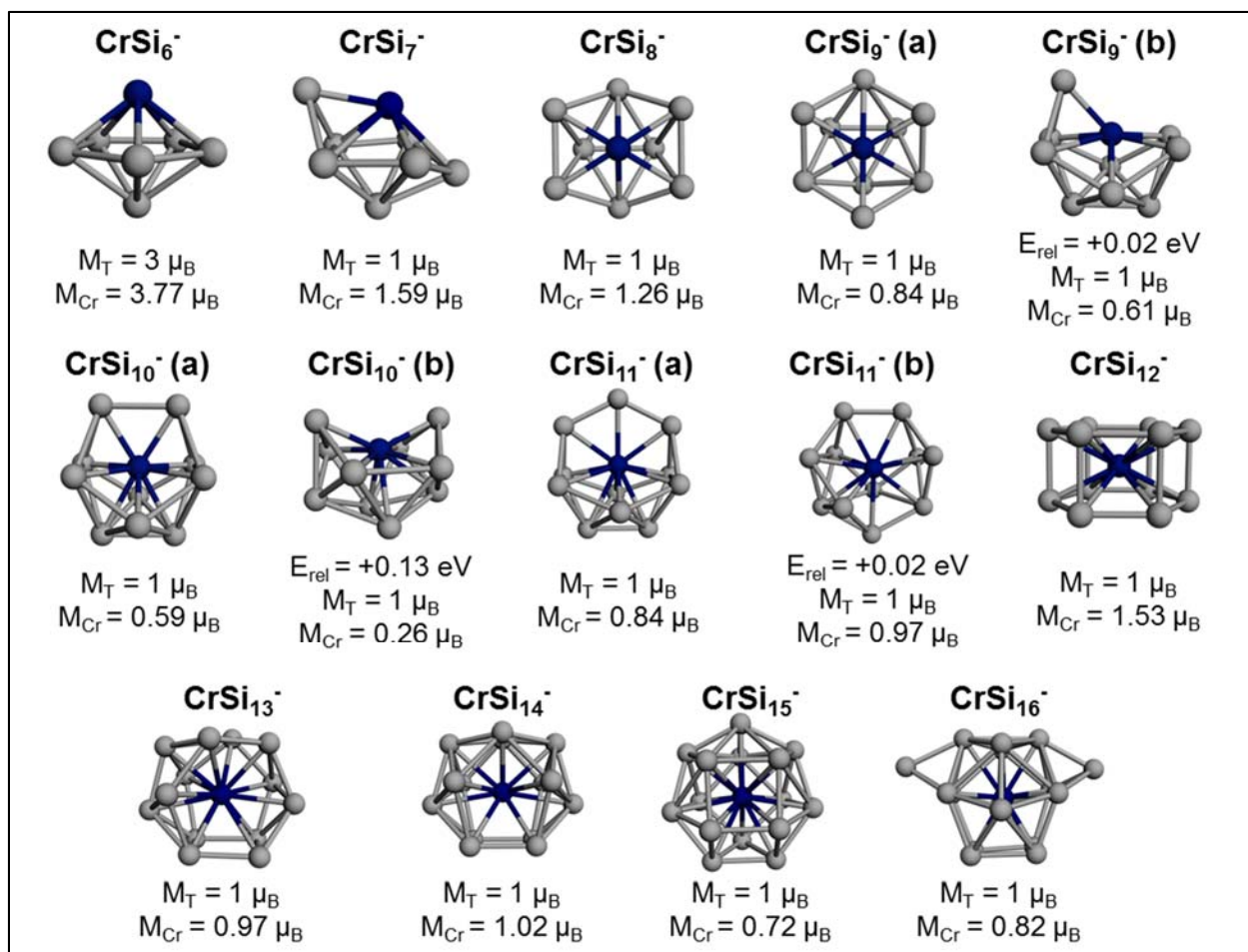


**Figure 4.2.2: PBE Ground States and Low-Lying Isomers of CrSi<sub>n</sub><sup>-</sup>.** The lowest energy geometries and those within 0.20 eV for anionic CrSi<sub>n</sub> (n=6-16) clusters found using the PBE functional are shown above. Silicon atoms are shown in gray and chromium atoms are shown in dark blue. The total magnetic moment ( $M_T$ ) and local magnetic moment on chromium ( $M_{Cr}$ ) are given for each cluster. Adapted from Figure S2 of Abreu et al.<sup>116</sup>

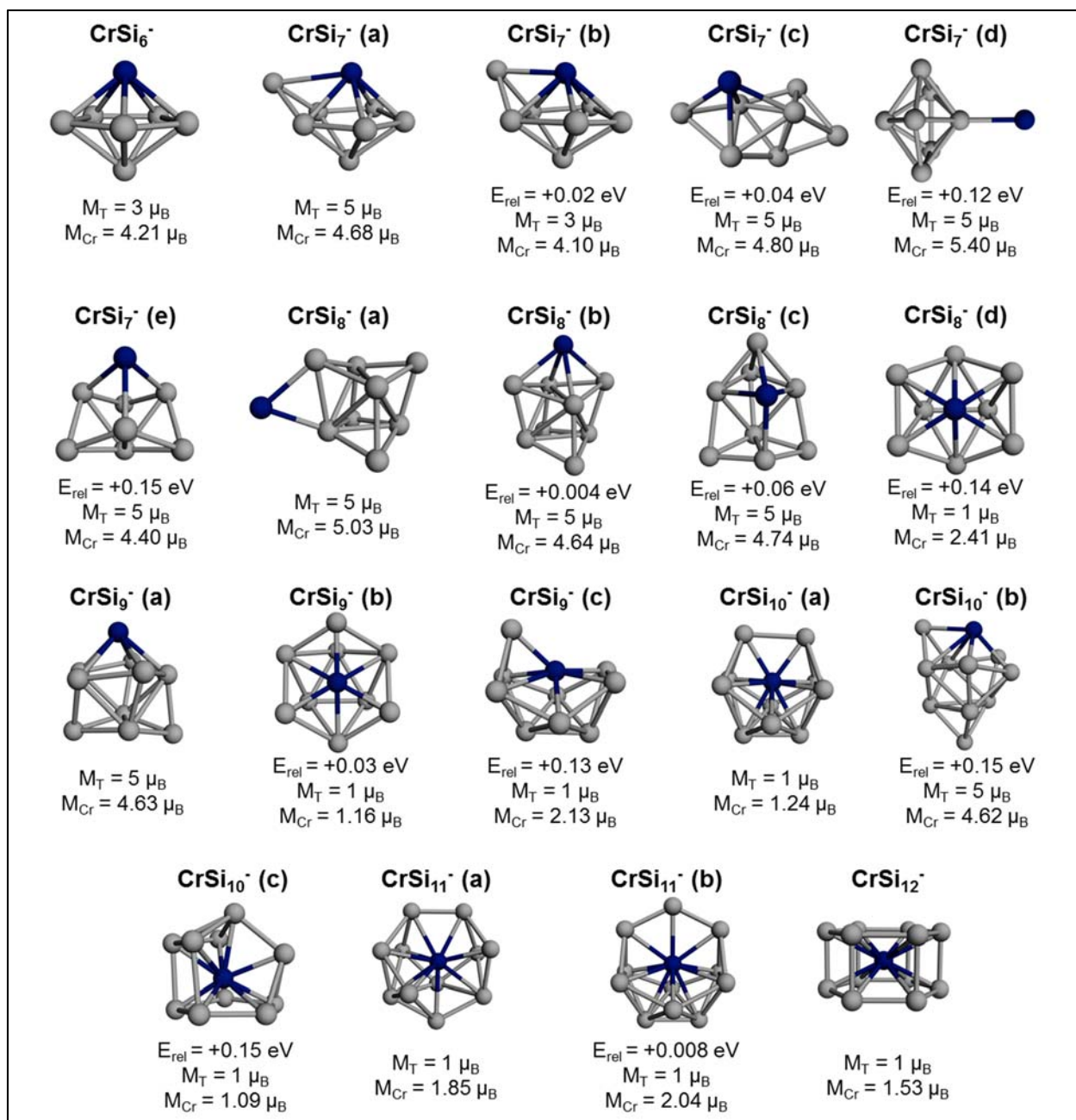


**Figure 4.2.3: B3LYP Ground States and Low-Lying Isomers of CrSi<sub>n</sub><sup>-</sup>.** The lowest energy geometries and those within 0.20 eV found with the B3LYP functional are shown above for the anions of CrSi<sub>n</sub> (n=6-12). Silicon atoms are gray and chromium atoms are dark blue. The total magnetic moment ( $M_T$ ) and the local magnetic moment on chromium ( $M_{Cr}$ ) are given for all geometries.

In comparing the low-lying structures of CrSi<sub>n</sub><sup>-</sup> found using PBE and B3LYP, it is noticeable that the B3LYP functional gives more low-lying isomers close to the ground state; all clusters except CrSi<sub>6</sub><sup>-</sup> and CrSi<sub>12</sub><sup>-</sup> have isomers within 0.20 eV, and most of these clusters have

several isomers in this energy range. On the other hand, the PBE functional yielded only three clusters with just one isomer within 0.20 eV of the ground state. Secondly, the magnetic properties of the clusters differ greatly depending on the functional. In the case of PBE, all the clusters have the lowest possible magnetic moment of 1  $\mu_B$ , except for the smallest,  $\text{CrSi}_6^-$ , which has a magnetic moment of 3  $\mu_B$ . When B3LYP is used, higher magnetic moments of 3  $\mu_B$  and 5  $\mu_B$  are favored for most clusters, even for cluster sizes as large as ten silicon atoms. The geometries themselves are also different; PBE tends to favor basket-like and eventually cage-like structures with an interior chromium atom, while B3LYP favors structures in which the chromium atom occupies an external position.

Using these anionic geometries, the photoelectron spectra were calculated using time-dependent density functional theory as described in Chapter 2. The anion geometry was forced neutral for a single-point calculation, meaning there was no geometry optimization. For each anion, it is necessary to calculate both possible spin states resulting from the removal of an electron – for an anion with a magnetic moment of  $M$ , neutral clusters can have magnetic moments  $M+1$  and  $M-1$ . For each spin state, the VDE was calculated as:

$$\text{VDE} = E(\text{CrSi}_n^-) - E(\text{CrSi}_n)_{\text{anion geom}} \quad (4.2-1)$$

which is the difference between the energy of the anion and the energy of the anion forced neutral. The ADE was also calculated for each cluster as the difference between the anion and the neutral ground state, as in Eq. (4.2-2):

$$\text{ADE} = E(\text{CrSi}_n^-) - E(\text{CrSi}_n)_{\text{GS}} \quad (4.2-2)$$

The lowest 50 excitations were calculated for the two possible spin states of each cluster using the anion clusters forced neutral with no geometry optimization. The VDE was added to the resulting excitations for each spin state to give the excitations of the anionic cluster. The line

spectra, showing individual excitations, and continuous spectra, generated from a Gaussian fitting of the excitation values, are shown for PBE and B3LYP in Figure 4.2.4 and Figure 4.2.5, respectively.

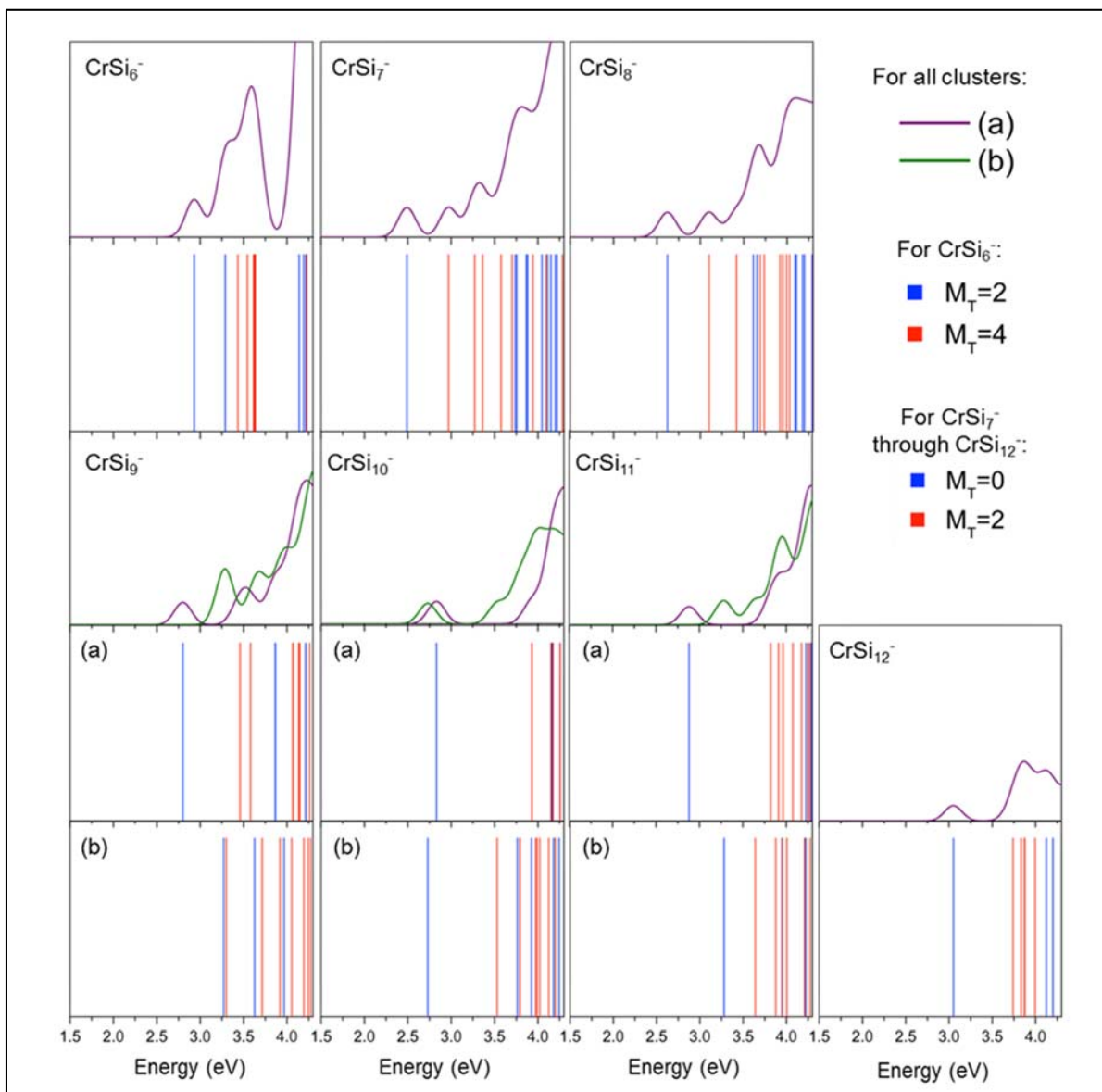


**Figure 4.2.4: PBE Simulated Photoelectron Spectra for CrSi<sub>n</sub><sup>-</sup> (n=6-12).** For each cluster, the bottom graph(s) show the excitations, represented as lines, for each possible spin state. The top graph shows a Gaussian fitting ( $\sigma=0.15$ ) of the excitation values. For clusters with isomers close to the ground state, (a) is the ground state geometry and (b) is the higher energy state. Taken from Figure S3 of Abreu et al.<sup>116</sup>

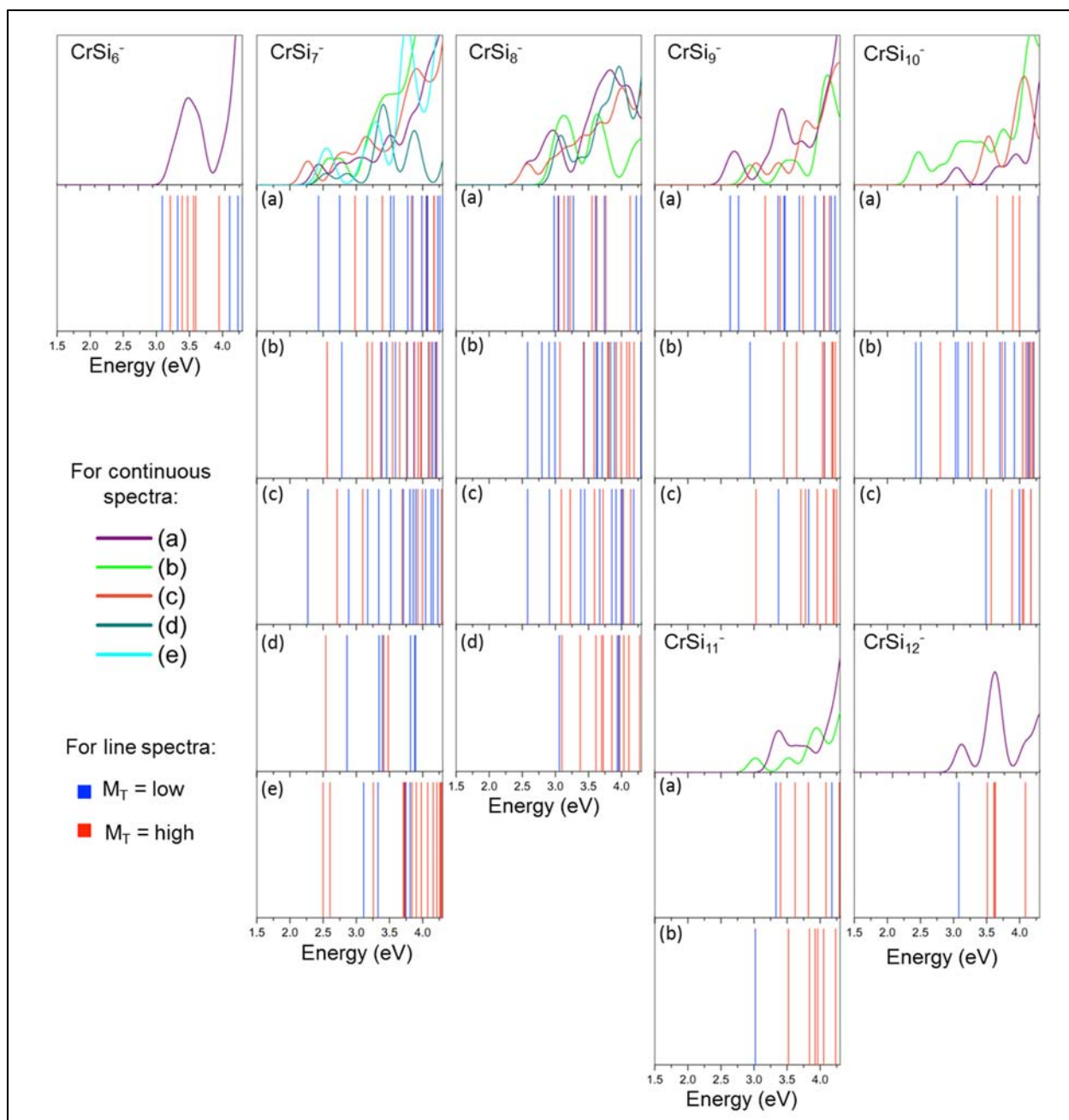


**Figure 4.2.5: B3LYP Simulated Photoelectron Spectra for CrSi<sub>n</sub><sup>-</sup> (n=6-12).** For each cluster, the bottom graph(s) show the excitations, represented as lines, for each possible spin state – the lower spin state is shown in blue and the higher spin state is shown in red. For anions with magnetic moments of 1, 3, and 5  $\mu_B$ , the resulting states are 0 and 2, 2 and 4, and 4 and 6  $\mu_B$ , respectively. (Please refer to Figure 4.2.3 for information about the possible spin states for the various isomers.) The top graph for each cluster shows a Gaussian fitting ( $\sigma=0.15$ ) of the excitation values – a continuous spectra. For clusters with isomers close to the ground state, the labels (a) through (e) are indicated and correspond to the geometries shown in Figure 4.2.3.

Comparing the continuous theoretical spectra to the experimental spectra in Figure 4.2.1, the PBE spectra match the experimental spectra very well, while the B3LYP spectra do not. To further exemplify this, Table 4.2-1 gives the VDE, ADE, and the relative position of the second peak in each spectrum for both PBE and B3LYP. These values are given only for the absolute ground state for clarity.

**Table 4.2-1: VDE, ADE, and Relative Position of the 2<sup>nd</sup> Peak of Theoretical and Experimental Photoelectron Spectra for CrSi<sub>n</sub><sup>-</sup> (6-12).**

Number of Si Atoms	VDE			ADE			Relative Position of 2nd Peak		
	PBE	B3LYP	Exp	PBE	B3LYP	Exp	PBE	B3LYP	Exp
6	2.93	3.09	2.98	2.54	2.22	3.12	0.36	0.12	0.55
7	2.49	2.43	2.56	2.44	2.20	2.42	0.48	0.32	0.64
8	2.62	2.98	2.72	2.54	2.45	2.61	0.48	0.06	0.80
9	2.80	2.64	2.90	2.67	2.49	2.71	0.47	0.12	0.52
10	2.83	3.05	2.88	2.66	2.72	2.68	1.10	0.61	1.22
11	2.88	3.33	2.97	2.77	2.98	2.79	0.76	0.07	0.98
12	3.05	3.09	3.19	3.05	3.06	3.11	0.69	0.43	0.83

The above table gives the theoretically calculated vertical and adiabatic detachment energies for both the PBE and B3LYP functionals and compares them to the experimental VDE and ADE values from Kong, et al.<sup>119</sup>. The relative position of the second peak on the spectra was taken from the theoretically simulated continuous spectra and compared to the experimental spectra. All theoretical values are given only for the ground states, even where isomers close in energy exist. Adapted from Table S1 of Abreu et al.<sup>116</sup>

In general, the PBE values are closer to the experimental values than those of B3LYP. This study confirms that the use of the PBE functional is appropriate for TM-doped silicon clusters, and PBE is used for the remaining calculations.

### 4.3 Calculating Cluster Properties

To characterize the stability of TMSi<sub>n</sub> (TM = Cr, W) clusters, several properties were calculated. The first of these is the incremental silicon binding energy, ΔSi, calculated as:

$$\Delta Si = E(\text{TMSi}_n) - (E(\text{TMSi}_{n-1}) + E(\text{Si})) \quad (4.3-1)$$

where  $E(\text{TMSi}_n)$  is the energy of the ground state of the cluster,  $E(\text{TMSi}_{n-1})$  is the energy of the ground state of the cluster of the preceding size, and  $E(\text{Si})$  is the energy of a free silicon atom. Because the energy of the preceding size is required,  $\Delta\text{Si}$  was calculated only for clusters with seven or more silicon atoms. A similar property, the transition metal embedding energy,  $\Delta\text{TM}$ , was calculated, by Equation (4.3-2):

$$\Delta\text{TM} = E(\text{TMSi}_n) - (E(\text{TM}) + E(\text{Si}_n)) \quad (4.3-2)$$

where  $E(\text{TM})$  is the energy of a free chromium or tungsten atom and  $E(\text{Si}_n)$  is the energy of the pure silicon cluster. For this calculation, the geometries of the pure silicon clusters used for both transition metals are shown in Figure B-5 of Appendix B and agree with structures previously found in theoretical studies of silicon clusters.<sup>121-126</sup> Relatively large values of both  $\Delta\text{Si}$  and  $\Delta\text{Cr}$  or  $\Delta\text{W}$  indicate that a cluster is stable to the removal of a silicon or transition metal atom, respectively. Note that the Wigner-Witmer spin conservation rules were not used.

The stability of these clusters to the addition or removal of an electron was also explored using the VDE, ADE, and the ionization potential, IP. The VDE and ADE were calculated for the remaining Cr-doped clusters ( $n=13-16$ ) using Equations (4.2-1) and (4.2-2), respectively, and for  $\text{WSi}_n$  ( $n=6-16$ ) using the same equations with the corresponding  $\text{WSi}_n$  energies. Low values of ADE and VDE indicate stability of the neutral cluster. The ionization potential for each cluster was calculated as shown below:

$$\text{IP} = E(\text{TMSi}_n) - E(\text{TMSi}_n^+) \quad (4.3-3)$$

where  $E(\text{TMSi}_n)$  is the ground state energy of the cluster, and  $E(\text{TMSi}_n^+)$  is the ground state energy of its cation. Higher values of IP indicate stability of the neutral cluster.

Finally, the hydrogen binding energy was calculated for each cluster because some of the experiments used silane,  $\text{SiH}_4$ , as a precursor to generate  $\text{CrSi}_n$  or  $\text{WSi}_n$  clusters. First, the



preferred hydrogen binding site was found by adding a hydrogen atom to many different sites on the ground state clusters, including both metal and silicon sites, and optimizing each geometry.

The hydrogen binding energy, H BE, was calculated for each ground state by Equation (4.3-4):

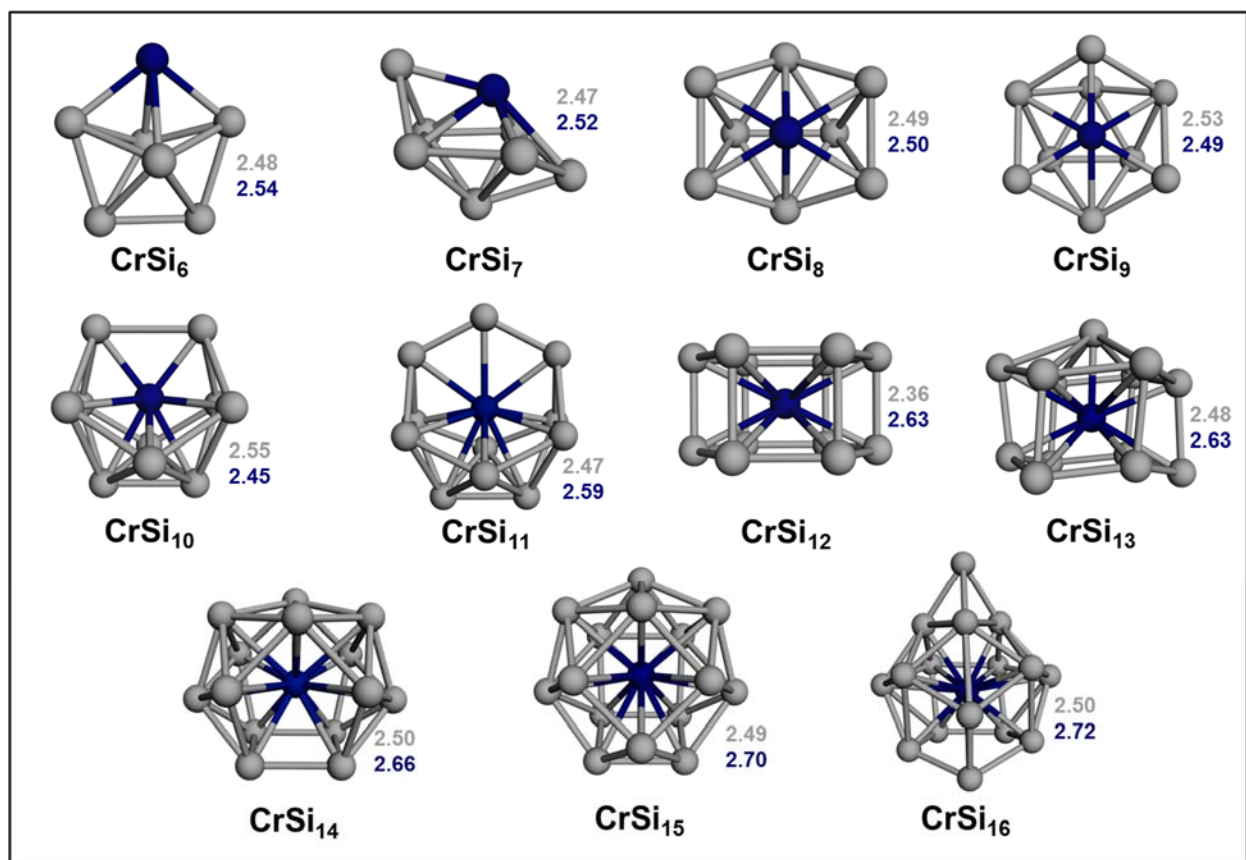
$$\text{H BE} = E(\text{HTMSi}_n) - (E(\text{H}) + E(\text{TMSi}_n)) \quad (4.3-4)$$

where  $E(\text{HTMSi}_n)$  is the energy of the lowest energy hydrogen bound cluster and  $E(\text{H})$  is the energy of a free hydrogen atom. The binding energy of a single hydrogen atom in a  $\text{H}_2$  molecule was calculated to be 2.26 eV and an H BE value lower than this indicates stability of the bare  $\text{TMSi}_n$  cluster.

## 4.4 $\text{CrSi}_n$ (n=6-16)

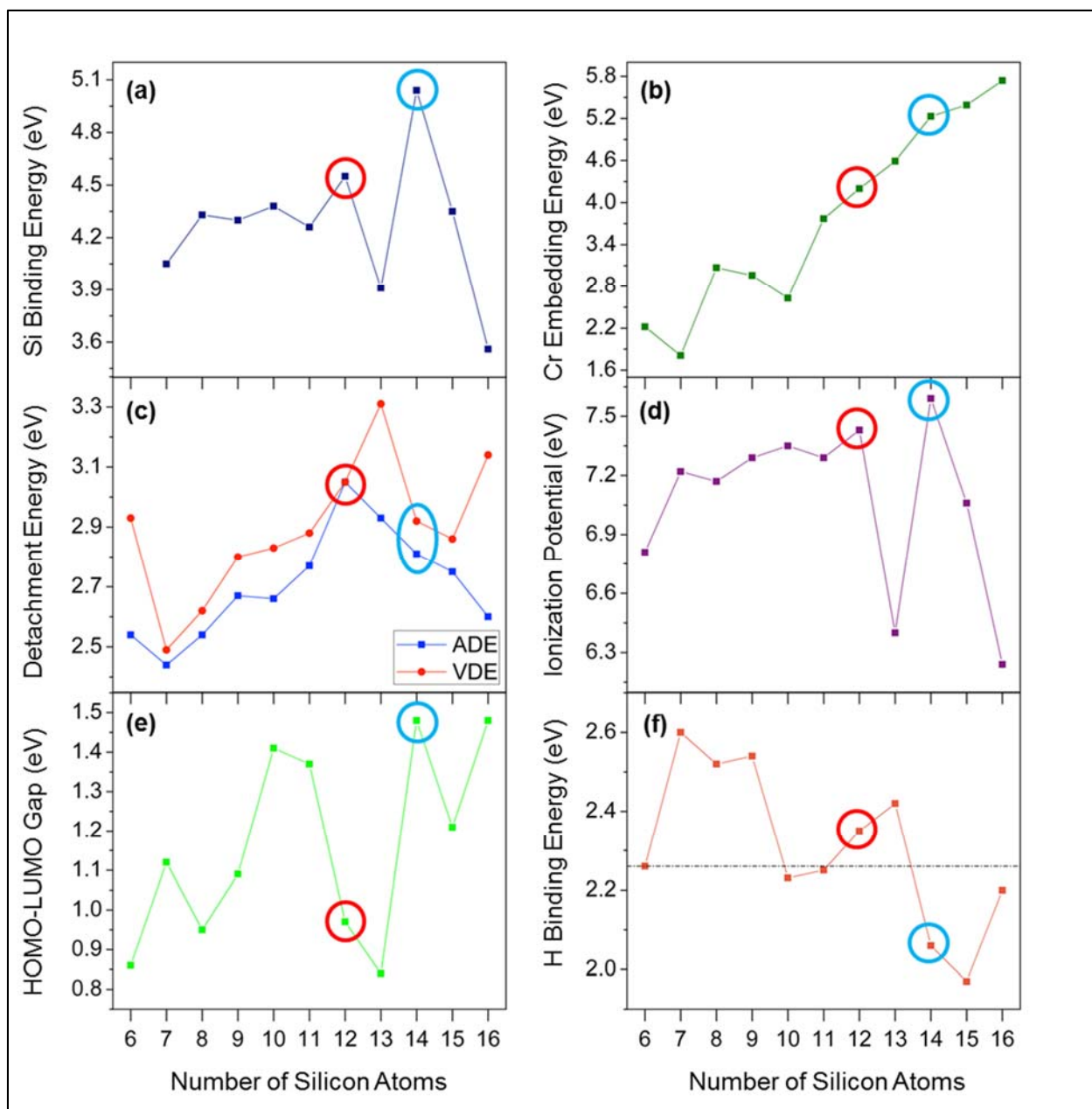
### 4.4.1 Energetics

Figure 4.4.1 shows the ground state geometries of  $\text{CrSi}_n$  (n=6-16) found using the PBE functional for exchange and correlation. Many structures were tried, and higher energy isomers are shown in Figure B-1 through Figure B-4 in Appendix B. The structures for neutral species are similar to the ones obtained in previous theoretical studies.<sup>71,72,77,79,81–84,89,90,118,119</sup> The magnetic moments of all the clusters are quenched, except for  $\text{CrSi}_6$ , which has a total magnetic moment of  $4 \mu_B$  and a local magnetic moment on the chromium atom of  $4.21 \mu_B$ . As shown in Figure 4.4.1, the chromium atom occupies an external site for clusters with six to nine silicon atoms. In  $\text{CrSi}_{10}$  and  $\text{CrSi}_{11}$ , the Cr is mostly embedded in the silicon cage, but is still partially exposed. For  $\text{CrSi}_{12}$  and larger clusters, the Cr atom is completely encapsulated. Thus,  $\text{CrSi}_{12}$  is the smallest cluster with a completely interior Cr atom.



**Figure 4.4.1: Ground State Geometries of Neutral CrSi<sub>n</sub> (n=6-16) Clusters.** The lowest energy isomers found using the PBE functional for CrSi<sub>n</sub> clusters are shown. Silicon atoms are gray and chromium atoms are in dark blue. The average Si-Si and Cr-Si bond lengths for each cluster are shown beside the geometries in gray and dark blue respectively. Taken from Figure 1 of Abreu et al.<sup>116</sup>

Values of  $\Delta\text{Si}$ ,  $\Delta\text{Cr}$ , ADE, VDE, IP, HOMO-LUMO gap, and H BE were calculated as described in Section 4.3. The energies of the ground state structures of the cationic clusters and hydrogen-bound clusters shown in Figure B-6 and Figure B-7, respectively, were used for the calculation of the IP and H BE. Similarly, the energies of the anionic structures previously shown in Figure 4.2.2 were used for the calculation of ADE and VDE. The trends in these values are given in Figure 4.4.2. Table B-1 in Appendix B gives each of these values explicitly.



**Figure 4.4.2: Energetic Properties of Ground State  $\text{CrSi}_n$  ( $n=6-16$ ) Clusters.** (a) The silicon binding energy,  $\Delta\text{Si}$ , for  $n=7-16$ . (b) The chromium embedding energy,  $\Delta\text{Cr}$ . (c) The adiabatic and vertical detachment energy, ADE and VDE, respectively. ADE is shown as blue squares and VDE is shown as red circles. (d) The ionization potential, IP. (e) The HOMO-LUMO gap. (f) The hydrogen binding energy. The horizontal dotted line shows the binding energy per hydrogen atom of  $\text{H}_2$  as a reference. In (a)-(f), the x-axis is the number of silicon atoms. Data points corresponding to  $\text{CrSi}_{12}$  and  $\text{CrSi}_{14}$  are included to guide the eye. Adapted from Figure 2 of Abreu et al.<sup>116</sup>

The  $\Delta Si$  binding energies, presented in Figure 4.4.2(a), show that  $CrSi_{14}$  has the largest binding energy while  $CrSi_{12}$  has the second largest. The progression in  $\Delta Si$  is consistent with stability as observed in experiments; in the case of growth in an ion trap,  $CrSi_{12}$  stands out as a magic species,<sup>76</sup> while in the case of synthesis via laser vaporization, the larger clusters are prominent.<sup>69,70</sup>  $\Delta Cr$  shows a monotonic increase—the clusters become more stable as the metal is increasingly surrounded—with  $CrSi_{14}$  having a larger than trend embedding energy. Figure 4.4.2(c) shows the ADE and VDE.  $CrSi_{12}$  has the largest ADE and third largest VDE, both 3.05 eV. It is surprising that  $CrSi_{12}$  has a very high ADE because magic neutral species are expected to have low ADE. The IP shown in Figure 4.4.2(d) also reveals  $CrSi_{14}$  to have the highest IP, 7.59 eV, and  $CrSi_{12}$  to have the second highest, 7.43 eV. Figure 4.4.2(e) shows the HOMO–LUMO gap, the strongest signature of a closed electronic shell, for each cluster.  $CrSi_{12}$  has a relatively small HOMO–LUMO gap of 0.97 eV, while  $CrSi_{14}$  has the largest HOMO–LUMO gap of 1.48 eV.

To interpret the final criterion, the H BE shown in Figure 4.4.2(f), the binding energy of a hydrogen atom in  $H_2$  was also calculated; found to be 2.26 eV, it is shown as the dashed line in Figure 4.4.2(f). Clusters that bind H strongly are likely to remain hydrogenated, while those with weak H binding energies are likely to be pristine  $CrSi_n$  species.  $CrSi_{14}$  and  $CrSi_{15}$  are found to have quite low H binding energies, indicating that  $H_2$  has the energy to autodissociate.  $CrSi_{12}$  binds hydrogen with 2.35 eV, slightly too strongly to allow autodissociation, although it binds H much more weakly than  $n=7-9$ . The previously described results bring out two stable clusters, namely,  $CrSi_{12}$  and  $CrSi_{14}$ . The fact that the binding energies of  $CrSi_{12}$  are relatively large suggests it is thermodynamically stable; however, the electronic criteria of the HOMO–LUMO gap and electron detachment energy suggest that  $CrSi_{12}$  does not possess high electronic stability.

CrSi<sub>14</sub> appears to possess both electronic and thermodynamic stability. One would expect that a cluster that is stabilized by the 18-electron rule would be electronically stable, even if it did not have a particularly high thermodynamic stability.

#### 4.4.2 Molecular Orbital Analysis

To uncover the underlying electronic principles governing the energetic properties of CrSi<sub>12</sub>, a thorough analysis of the molecular orbitals was undertaken. All of the occupied orbitals are shown in Figure B-8 and Figure B-9, while unoccupied orbitals are shown in Figure B-10 in Appendix B. The MOs of CrSi<sub>12</sub> were first examined against the CNFEG model for a nearly free electron gas. By looking at the shape, symmetry, and nodes of the MOs, each was assigned a CNFEG model orbital designation, e.g., 1S or 2P. These designations are shown explicitly for each orbital pictured in Appendix B. In Figure 4.4.3, the CNFEG model orbital designations are given on the left-hand side, where S orbitals are shown in black; P, blue; D, red; F, green; and G, purple. This analysis reveals that a simple CNFEG model is inconsistent with the observed electronic structure. With 54 total electrons, the assigned CNFEG shell structure for CrSi<sub>12</sub> is  $|1S^2|1P^4|1P^2 1D^8|1F^8 1D^2 2S^2|1F^4 2P^6 2D^{12} 1G^4||1D^2|$ , with the  $|$  indicating distinct sets of orbitals with similar energies and the  $||$  indicating the line between filled and unfilled orbitals. The  $2D^{12}$  occupation occurs because of covalent bonding between the silicon cage and the Cr atom, demonstrating that a simple split-CNFEG model with charge transfer is unable to explain the electronic structure of the cluster.

Having shown that a CNFEG model, whether applied to the full cluster or centered only on the chromium atom, does not fit the electronic structure of CrSi<sub>12</sub>, the nature of the MOs in CrSi<sub>12</sub> were further analyzed to determine if the 18-electron rule applies. Most noticeably, the LUMO of CrSi<sub>12</sub> is the 3d<sub>z<sup>2</sup></sub> orbital of Cr, and an analysis of the filled orbitals reveals no other

significant contributions to MOs from  $3d_{z^2}$ . If the 18-electron rule did apply to  $\text{CrSi}_{12}$ , then all five 3d orbitals must be occupied. A fragment analysis was performed wherein the cluster was divided into Cr and  $\text{Si}_{12}$  fragments,<sup>127,128</sup> allowing states that contain appreciable contributions from Cr or  $\text{Si}_{12}$  sites to be identified. On the right-hand side of Figure 4.4.3, the MOs are classified by their fragment composition.

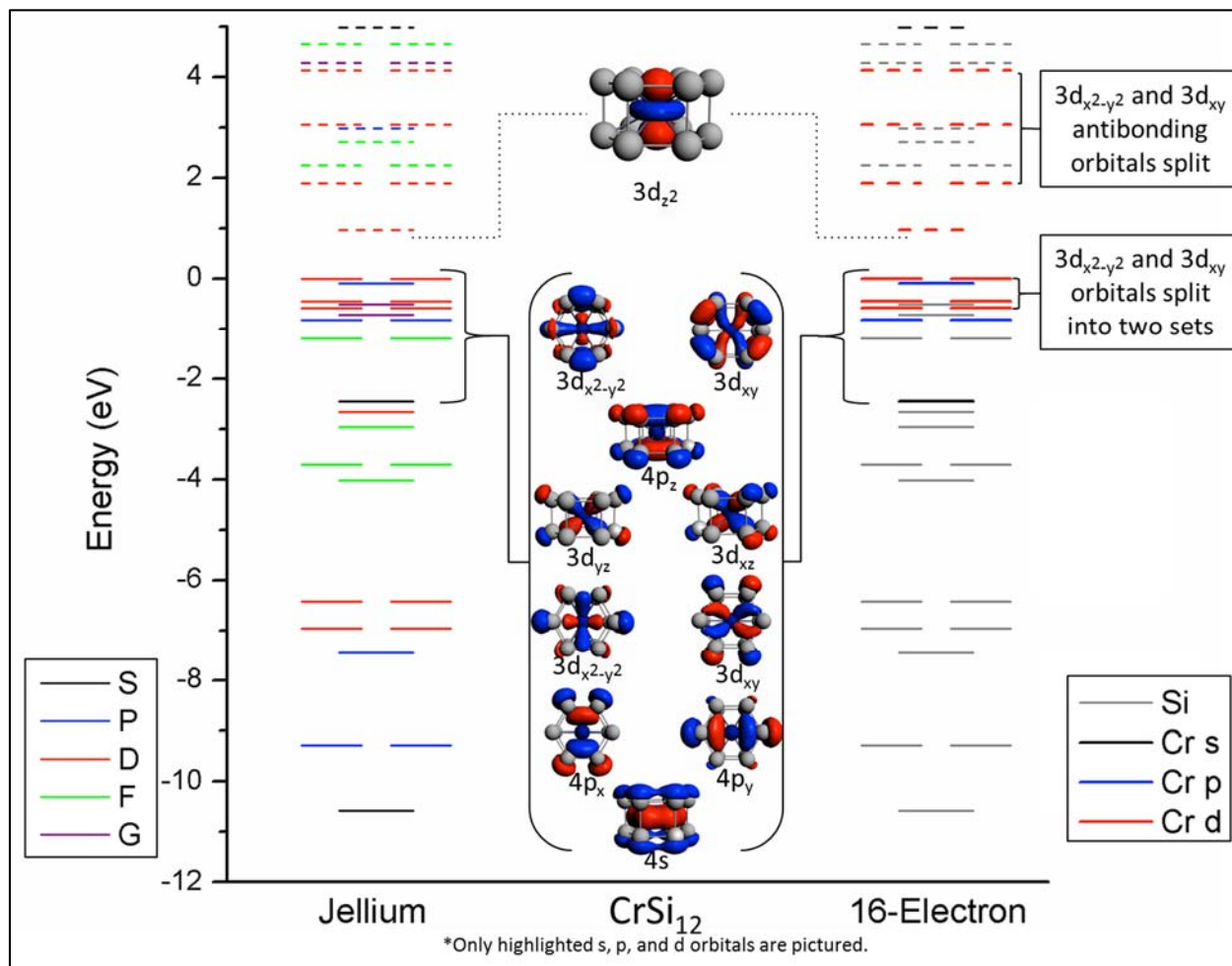


**Figure 4.4.3:  $\text{CrSi}_{12}$  Orbital Energy Levels and Selected Orbitals.** On the left hand, the orbital energy levels are assigned as S, P, D, F, or G delocalized orbitals as per the CNFEG (Jellium) model. On the right, the orbital energy levels are assigned based on orbital composition as predominantly silicon, shown in gray, or having chromium s, p, or d character. Occupied orbitals are shown as solid lines and unoccupied orbitals are shown with dashed lines. The orbitals pictured are those with high Cr character, and the contributing Cr orbital is noted. Adapted from Figure 3 of Abreu et al.<sup>116</sup>

Orbitals with predominantly Si<sub>12</sub> character are gray while orbitals possessing significant Cr character are shown in black, blue, and red, for 4s, 4p, and 3d orbitals, respectively. While it appears that there are six 3d orbitals in Figure 4.4.3, the 3d<sub>x<sup>2</sup>-y<sup>2</sup></sub> and 3d<sub>xy</sub> orbitals actually hybridize with the Si<sub>12</sub> cage and split into two sets of orbitals, each with about equal Cr 3d orbital character. Thus, this analysis shows that the 4s and 4p orbitals, as well as all the 3d orbitals except for 3d<sub>z<sup>2</sup></sub>, are filled. These orbitals are pictured in Figure 4.4.3. Thus, the Cr atom is found to have an electronic configuration of 4s<sup>2</sup>4p<sup>6</sup>3d<sup>8</sup>, indicating that the Cr atom has 16 effective valence electrons.

To understand why this cluster has an appreciable HOMO–LUMO gap with only 16 valence electrons, one must look to the geometric structure of the cluster. The hexagonal structure of the CrSi<sub>12</sub> is oblate with no silicon atoms along the primary axis of rotation. This causes a crystal-field-like splitting<sup>52</sup> of the 3d orbitals, with the 3d<sub>z<sup>2</sup></sub> orbital being pushed up in energy. Much like a square-planar transition metal complex, the cluster becomes electronically stable with 16 effective valence electrons rather than the previously expected 18 effective valence electrons. A similar crystal-field splitting marks the Cr 4p orbitals, although they are filled, with the 4p<sub>z</sub> being higher in energy than 4p<sub>x</sub> and 4p<sub>y</sub>. While the oblate D<sub>6h</sub> structure causes crystal-field splitting to give CrSi<sub>12</sub> a respectable HOMO–LUMO gap, the cluster is not characterized by a filled 3d electronic shell. This is the reason that CrSi<sub>12</sub> does not exhibit all of the electronic markers of a magic species.

While the 18-electron rule does not apply to CrSi<sub>12</sub>, which has been shown to have 16 effective valence electrons rather than 18, another candidate for 18-electron rule stability is CrSi<sub>14</sub>. As shown in the previous section, CrSi<sub>14</sub> has the largest HOMO–LUMO gap and ΔSi, making it the most stable cluster; so does the 18-electron rule apply to this magic cluster? To

answer this question, the same MO analysis was carried out for CrSi<sub>14</sub>, as was done for CrSi<sub>12</sub>. All of the occupied orbitals are shown in Figure B-11 and Figure B-12 and select unoccupied orbitals are shown in Figure B-13 in Appendix B. The cluster was split into Cr atom and Si<sub>14</sub> cage fragments in order to explore the makeup of each orbital, and determine the effective valence electrons on the Cr atom. The results of this are shown in Figure 4.4.4.

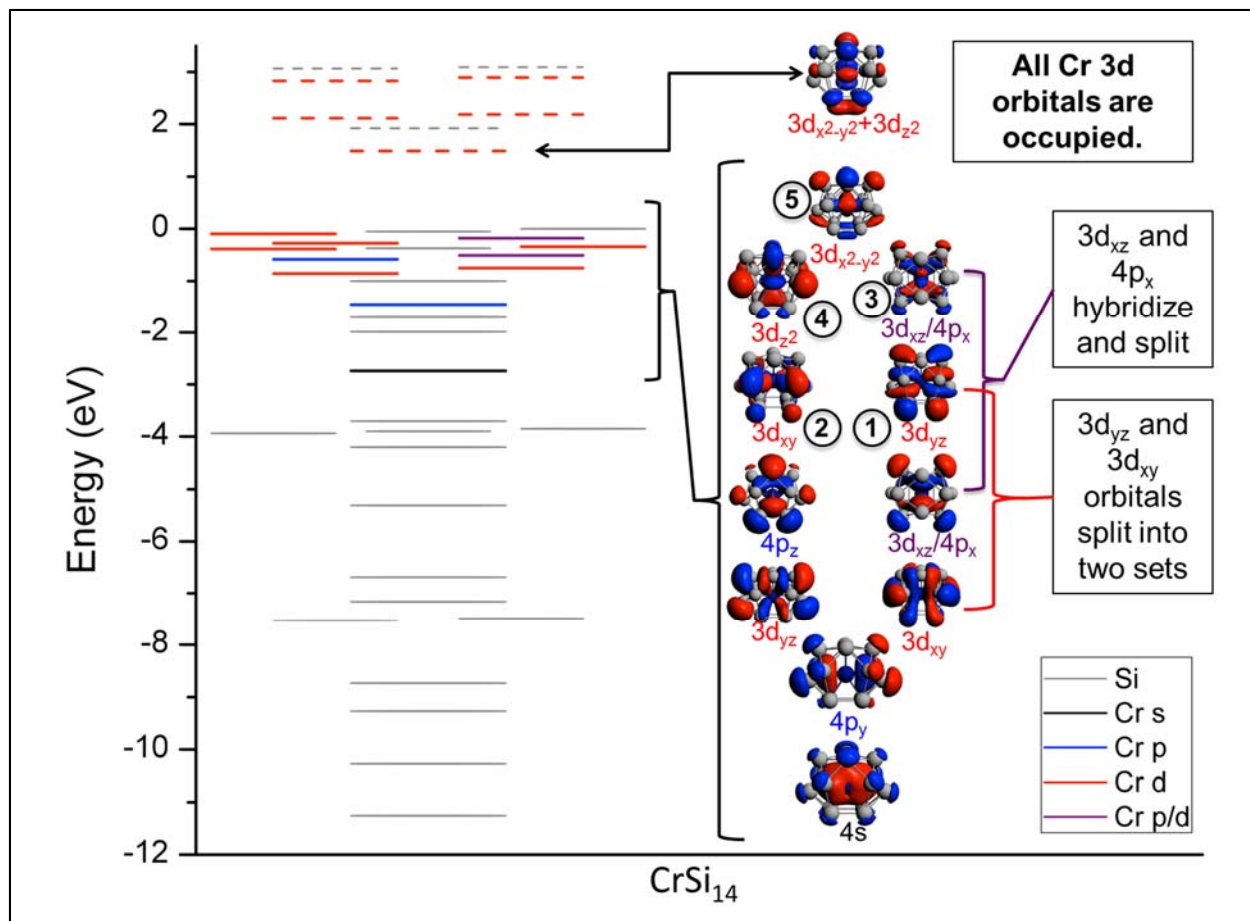


**Figure 4.4.4: CrSi<sub>14</sub> Orbital Energy Levels and Selected Orbitals.** The orbital energy levels of CrSi<sub>14</sub> are shown and are assigned based on orbital composition as predominantly silicon, shown in gray, or having chromium s, p, d, or p-d hybrid character, shown in black, blue, red, and purple, respectively. Occupied orbital energy levels are shown with solid lines, and unoccupied orbital energy levels are shown with dashed lines. The orbitals pictured are those with high Cr character, and the contributing Cr orbital is noted. Taken from Figure 4 of Abreu et al.<sup>116</sup>



On the left-hand side, the orbital energy levels are again colored by their composition, while on the right the MOs containing appreciable amounts of Cr character are pictured. The electronic structure of CrSi<sub>14</sub> is found to be 4s<sup>2</sup>3d<sup>10</sup>4p<sup>6</sup> with all five of the 3d orbitals being occupied. Due to the lower symmetry of CrSi<sub>14</sub> (C<sub>2v</sub>) compared to CrSi<sub>12</sub>, there is more hybridization between orbitals than in CrSi<sub>12</sub>. Most notably, there is significant hybridization between the 3d<sub>xz</sub> and the 4p<sub>x</sub> orbitals, resulting in two mixed orbitals. Additionally, the 3d<sub>xy</sub> and 3d<sub>yz</sub> orbitals hybridize with the Si<sub>14</sub> cage to produce two sets of orbitals each. The comparably more spherical shape of the Si<sub>14</sub> cage results in the 3d orbitals all being within 0.84 eV of each other and no dramatic crystal-field splitting is observed. The LUMO is a mixture of the 3d<sub>x<sup>2</sup>-y<sup>2</sup></sub> and 3d<sub>z<sup>2</sup></sub> orbitals, lying 1.48 eV above the HOMO. Thus, CrSi<sub>14</sub> has 18 effective valence electrons and follows the 18-electron rule.

In order to expand the MO analysis to the rest of the series, the remaining clusters were split into fragments and the resulting MO compositions were analyzed to determine the effective valence electrons on the Cr atom. Surprisingly, the results show that all clusters except for CrSi<sub>6</sub> have 18 effective valence electrons. Being a magnetic cluster with four unpaired electrons, CrSi<sub>6</sub> has an effective valence count of 14. To further characterize the electronic structure, the width of the 3d-bands – that is, the difference in energy between the lowest and highest energy orbitals encompassing all five of the 3d orbitals of Cr – was calculated for all clusters except CrSi<sub>6</sub>, since it has half-filled orbitals. The 3d-band width can be thought of as a measure of the local environment surrounding the metal; the narrower the band, the more spherically distributed the silicon atoms are around the Cr atom. Figure 4.4.5 shows the results of this analysis.

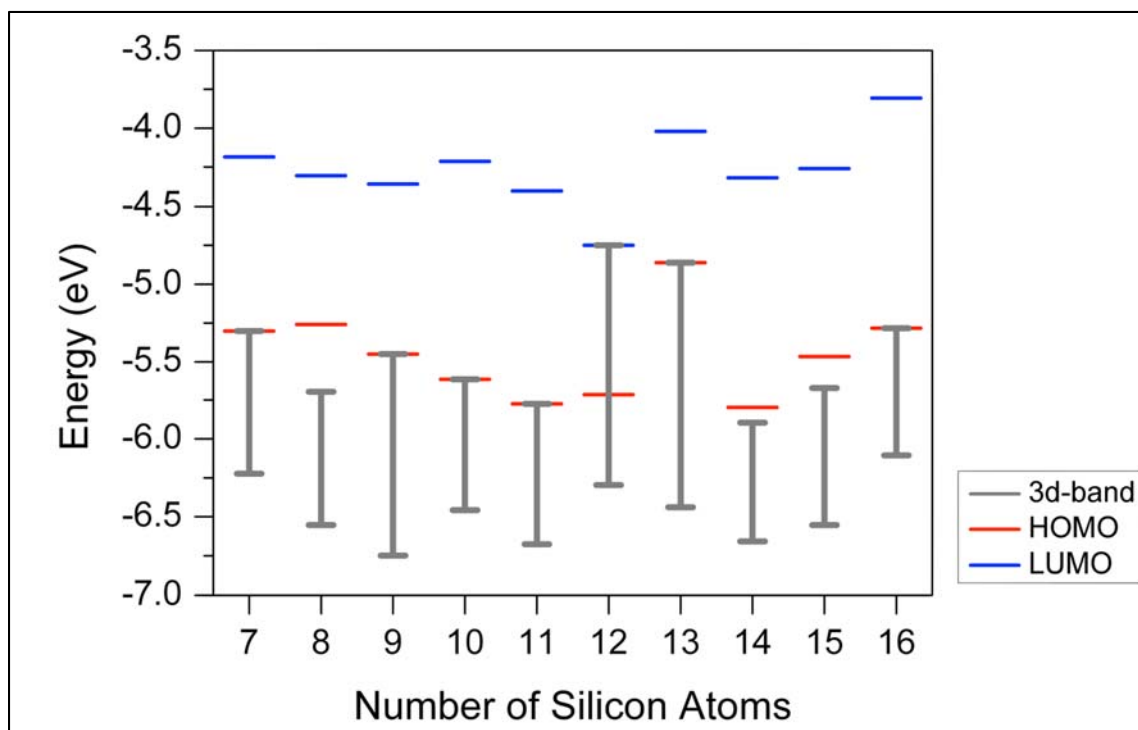


**Figure 4.4.5: The 3d-Bands of CrSi<sub>n</sub>.** The bands formed by the 3d orbitals of chromium are shown as vertical gray lines relative to the HOMO in red and the LUMO in blue for CrSi<sub>n</sub> (n=7-16). The absolute energy of the orbitals is given on the y-axis.

For most clusters, the 3d-band width is around 0.8 eV, but for CrSi<sub>12</sub> and CrSi<sub>13</sub>, this value jumps to about 1.6 eV. In the case of CrSi<sub>12</sub>, the crystal-field splitting of the 3d orbitals resulting in the unoccupied 3d<sub>z<sup>2</sup></sub> orbital being pushed up in energy has already been discussed. CrSi<sub>12</sub> is the only cluster for which the 3d-band encompasses an empty orbital. CrSi<sub>13</sub> has a geometry similar to CrSi<sub>12</sub>, being a capped distorted hexagonal prism of C<sub>3v</sub> symmetry. The MO analysis reveals that the electronic structure, in terms of the energies of the 3d orbitals, is very similar to that of CrSi<sub>12</sub>. Furthermore, the HOMO in CrSi<sub>13</sub> is the Cr 3d<sub>z<sup>2</sup></sub> orbital, and so the size of the 3d-band does not change upon addition of a thirteenth silicon atom. The clusters with the narrowest 3d-bands are CrSi<sub>14</sub>, CrSi<sub>15</sub>, and CrSi<sub>16</sub>, which are the three most spherical clusters in the series.

## 4.5 WSi<sub>n</sub> (n=6-16)

### 4.5.1 Energetics

The ground state structures of WSi<sub>n</sub> are shown in Figure 4.5.1. Higher energy isomers within 1.0 eV of the ground state are shown in Figure B-14, Figure B-15, and Figure B-16 in Appendix B. For the most part, the ground state structures resemble those of CrSi<sub>n</sub>, including the hexagonal prism structure of WSi<sub>12</sub>, although due to the greater size of tungsten compared to chromium the average Si-Si and TM-Si bond lengths are slightly longer. The most notable difference in geometry occurs for WSi<sub>6</sub>, in which the W atom occupies a central capping location rather than being part of the pentagon as was found for CrSi<sub>6</sub>. The magnetic moment of WSi<sub>6</sub>, like all the clusters in the WSi<sub>n</sub> series studied, is quenched, whereas CrSi<sub>6</sub> was found to be magnetic. Another difference in geometry can be seen for WSi<sub>13</sub>. Unlike the capped distorted hexagonal prism seen for CrSi<sub>13</sub>, WSi<sub>13</sub> is a distorted hexagonal antiprism, and the capping thirteenth atom bonds to only four of the six silicon atoms in the upper hexagon. Additionally, the symmetry of TMSi<sub>13</sub> is slightly reduced from C<sub>3v</sub> for CrSi<sub>13</sub> to C<sub>2v</sub> for WSi<sub>13</sub>. WSi<sub>15</sub> and WSi<sub>16</sub> also show slight differences in their ground state structures compared to their Cr-doped counterparts.

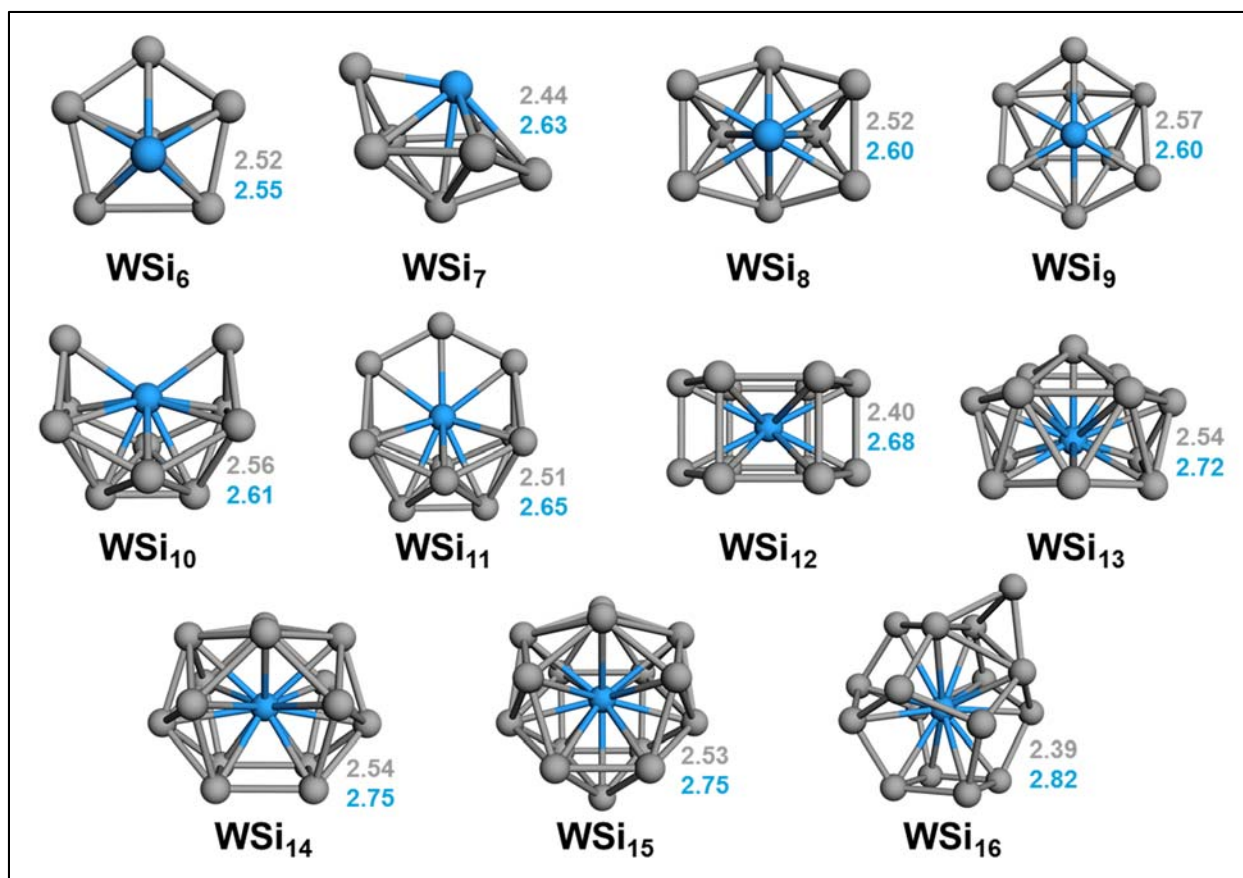


**Figure 4.5.1: Ground State Structures of WSi<sub>n</sub> (n=6-16).** Above shows the lowest energy structures of neutral WSi<sub>n</sub> (n=6-16). Tungsten atoms are shown in blue and silicon atoms are shown in grey. The average Si-Si and W-Si bond lengths are given next to each structure in gray and blue respectively.

The same energetic properties were calculated for WSi<sub>n</sub> as for CrSi<sub>n</sub> as described in Section 4.3. Again  $\Delta Si$  was calculated only for n=7-16, since the energy of the previous cluster size is needed for the calculation. The energies of the anionic structures, cationic structures, and hydrogen-bound structures shown in Figure B-17, Figure B-18, and Figure B-19 in Appendix B were used to calculate the ADE, VDE, IP,  $\Delta W$ , and H BE. The trends in the  $\Delta Si$ ,  $\Delta W$ , ADE, VDE, IP, HOMO-LUMO gap, and H BE for WSi<sub>n</sub> are given in Figure 4.5.2. Table B-2 in Appendix B explicitly lists each of these values.

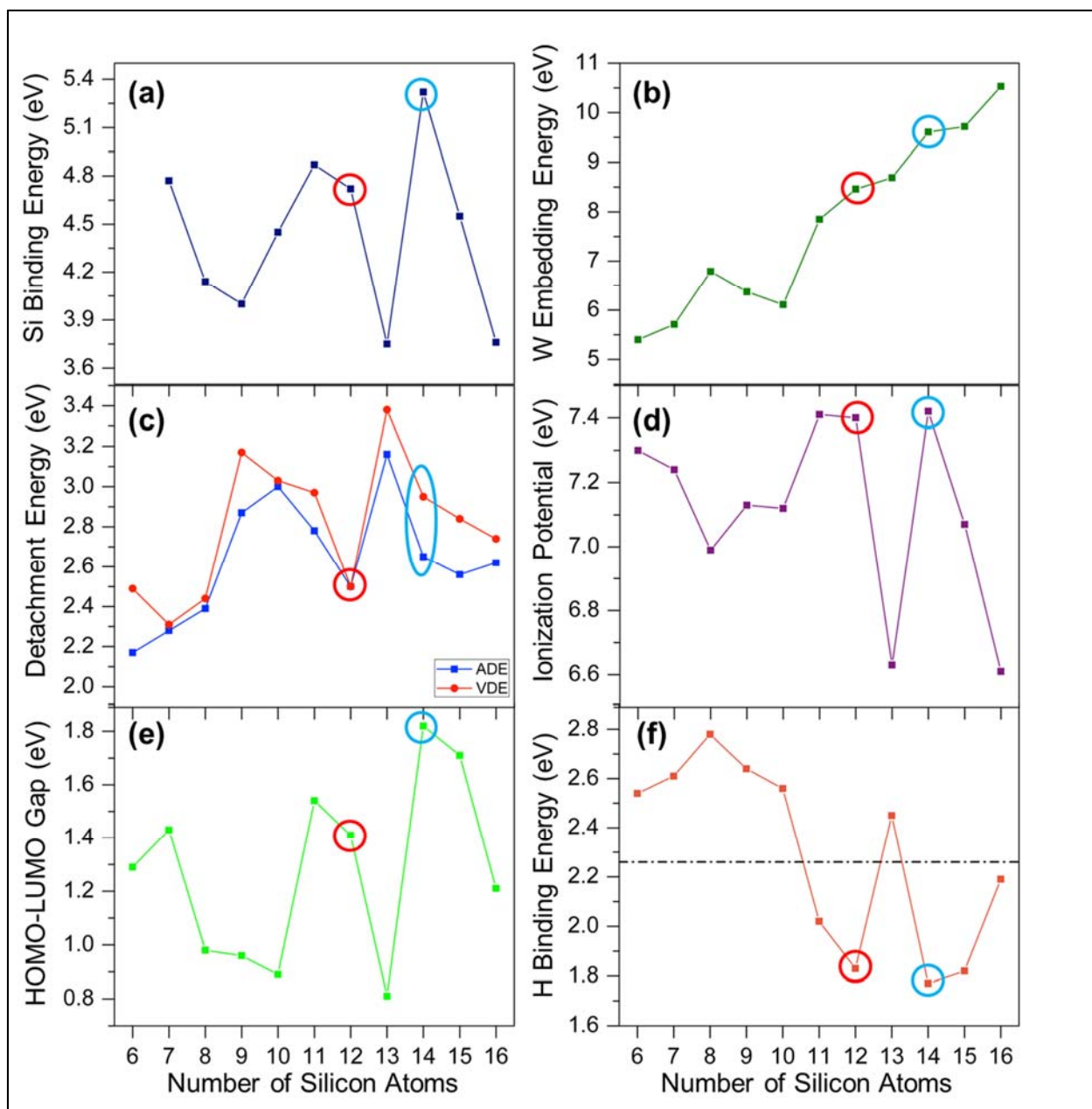


**Figure 4.5.2: Energetic Properties of  $WSi_n$  ( $n=6-16$ ) Ground States.** (a) The silicon binding energy,  $\Delta Si$ , for  $n=7-16$ . (b) The tungsten embedding energy,  $\Delta W$ . (c) The adiabatic and vertical detachment energy, ADE and VDE, respectively. ADE is shown as blue squares and VDE is shown as red circles. (d) The ionization potential, IP. (e) The HOMO-LUMO gap. (f) The hydrogen binding energy. The horizontal dotted line shows the binding energy per hydrogen atom of  $H_2$  as a reference. In (a)-(f), the x-axis is the number of silicon atoms. Data points corresponding to  $WSi_{12}$  and  $WSi_{14}$  are circled as a guide for the eye.

As can be seen in Figure 4.5.2(a), the silicon binding energies show notable differences from those of  $CrSi_n$ .  $WSi_7$  has a much higher  $\Delta Si$ , perhaps due to the differing ground state

geometry of  $\text{WSi}_6$ .  $\text{WSi}_{11}$  has a slightly higher  $\Delta\text{Si}$  at 4.87 eV than  $\text{WSi}_{12}$  at 4.72 eV, which is opposite of the case in the  $\text{CrSi}_n$  series.  $\text{WSi}_{14}$ , just like  $\text{CrSi}_{14}$ , has the highest  $\Delta\text{Si}$  in the series, 5.32 eV.  $\text{WSi}_{13}$  and  $\text{WSi}_{16}$  have the lowest  $\Delta\text{Si}$  values at 3.75 eV and 3.76 eV, respectively; compared to the  $\Delta\text{Si}$  of their Cr-doped counterparts, the  $\Delta\text{Si}$  of  $\text{WSi}_{13}$  increases by about 0.15 eV while that of  $\text{WSi}_{16}$  decreases by about the same amount. Overall,  $\Delta\text{Si}$  again indicates enhanced stability of  $\text{WSi}_{12}$  and  $\text{WSi}_{14}$ , and  $\text{WSi}_{11}$  gains some stability compared with  $\text{CrSi}_{11}$ . The trend in  $\Delta W$ , shown in Figure 4.4.2(b), appears nearly identical to the trend of  $\Delta\text{Cr}$ ; it generally increases monotonically with a slightly above average increase at  $\text{WSi}_{14}$ . Unlike the trend for  $\Delta\text{Cr}$ , that of  $\Delta W$  shows  $\text{WSi}_{12}$  to be slightly higher than the average increase as well.

A great difference can be seen between the energetic properties of the  $\text{CrSi}_n$  and  $\text{WSi}_n$  series in Figure 4.5.2(c), which shows the ADE and VDE trends for  $\text{WSi}_n$ . Unlike  $\text{CrSi}_{12}$ , which has the highest ADE and second highest VDE in the  $\text{CrSi}_n$  series, the ADE and VDE values of  $\text{WSi}_{12}$  are among the lowest in the  $\text{WSi}_n$  series. They still remain identical: both ADE and VDE are 2.50 eV. Low detachment energies are markers of magicity that were missing from the energetic description of  $\text{CrSi}_{12}$ , but are found in  $\text{WSi}_{12}$ . In the  $\text{WSi}_n$  series,  $\text{WSi}_{13}$  has the highest ADE and VDE, and  $\text{WSi}_9$  also shows high values of both, which was not the case for  $\text{CrSi}_9$ . The IPs, shown in Figure 4.5.2(d), generally show the same trend as those of  $\text{CrSi}_n$ , with  $\text{WSi}_{12}$ , 7.40 eV, and  $\text{WSi}_{14}$ , 7.42 eV, having the highest IPs and  $\text{WSi}_{13}$ , 6.63 eV, and  $\text{WSi}_{16}$ , 6.61 eV, having the lowest. The IP of  $\text{WSi}_{11}$ , however, increases slightly from that of  $\text{CrSi}_{11}$  to be about the same as that of  $\text{WSi}_{12}$ .

The trend in the HOMO-LUMO gaps of  $\text{WSi}_n$ , presented in Figure 4.5.2(e), shows some interesting differences when compared to that of  $\text{CrSi}_n$ . The gap of  $\text{WSi}_{10}$  is greatly reduced compared to  $\text{CrSi}_{10}$ —from 1.41 eV to 0.89 eV. This could be due to geometrical differences; the

bond lengths in  $\text{WSi}_{10}$  are greater than those in  $\text{CrSi}_{10}$ —the top Si-Si bond seen in  $\text{CrSi}_{10}$  stretches to the point that these silicon atoms are no longer bonded in  $\text{WSi}_{10}$ .  $\text{WSi}_{14}$  has the highest HOMO-LUMO gap in the series at 1.82 eV,  $\text{WSi}_{15}$  has the second highest at 1.71 eV, and  $\text{WSi}_{11}$  has the third highest at 1.54 eV. Surprisingly, the gap of  $\text{WSi}_{12}$  is 1.41 eV—a large increase from the 0.97 eV gap of  $\text{CrSi}_{12}$ . This is likely due to the crystal-field splitting of the 5d orbitals, which generally show greater splitting than 3d orbitals. Despite its differing geometry,  $\text{WSi}_{13}$ , just like  $\text{CrSi}_{13}$ , has the lowest HOMO-LUMO gap in the series at 0.81 eV. The gap of  $\text{WSi}_{15}$  is increased and that of  $\text{WSi}_{16}$  is decreased compared to their Cr-counterparts, an effect of the different ground state structures between the Cr-doped and W-doped  $\text{TMSi}_n$  clusters.

Finally, the hydrogen binding energies, shown in Figure 4.5.2(f), indicate that  $\text{WSi}_{11}$ ,  $\text{WSi}_{12}$ , and  $\text{WSi}_{14}$  through  $\text{WSi}_{16}$  have low enough H BEs that the hydrogen atoms will autodissociate, indicating that the dehydrogenated clusters are stable. This is another important change from the  $\text{CrSi}_n$  series, in which  $\text{CrSi}_{12}$  had a hydrogen binding energy high enough at 2.35 eV to indicate that hydrogen would not easily dissociate from the cluster. With the change to W, the H BE drops to 1.83 eV. Similarly, while  $\text{CrSi}_{14}$  had a low enough H BE, 2.06 eV, to indicate autodissociation of hydrogen, substituting W causes a further drop to 1.77 eV. The H BE results for  $\text{WSi}_n$  agree better with the experimental results of Hiura et al. than those of the  $\text{CrSi}_n$  series; they more clearly show that hydrogenation is greatly favored for clusters with six through ten silicon atoms, less favored for eleven silicon atoms, and finally, completely unfavorable with twelve silicon atoms.

Overall, the enhanced stability of  $\text{TMSi}_{14}$  is preserved upon substitution of Cr with W. With a large  $\Delta\text{Si}$ ,  $\Delta\text{W}$ , HOMO-LUMO gap, and IP, and a relatively low ADE, VDE, and H BE,  $\text{WSi}_{14}$  has all the markers of a magic cluster. Unexpectedly, the substitution of the transition

metal also results in greater stability for  $\text{TMSi}_{12}$ . In contrast to  $\text{CrSi}_{12}$ ,  $\text{WSi}_{12}$  shows all the markers of magic stability; it has a higher HOMO-LUMO gap, ADE and VDE about 0.50 eV lower than  $\text{CrSi}_{12}$ , and a H BE clearly indicative of hydrogen dissociation. The sometimes dramatically differing energetic results between  $\text{WSi}_{12}$  and  $\text{CrSi}_{12}$  may suggest that Cr does not behave entirely the same as W, despite having the same number of valence electrons.

#### 4.5.2 Molecular Orbital Analysis

In order to understand the bonding in  $\text{WSi}_n$ , and compare it to that found in  $\text{CrSi}_n$ , fragment analyses were performed on all clusters in the series and the composition of the MOs was examined. The MO analysis of  $\text{WSi}_{12}$  revealed that the  $5d_{z^2}$  orbital of W is unoccupied and serves as the LUMO of the cluster, just like the  $3d_{z^2}$  orbital of Cr in  $\text{CrSi}_{12}$ . Presumably, the crystal-field splitting of the 5d orbitals gives  $\text{WSi}_{12}$  magic stability despite its possessing only 16 effective valence electrons. As previously mentioned, the splitting is greater for 5d orbitals than for 3d orbitals, resulting in a larger HOMO-LUMO gap than  $\text{CrSi}_{12}$ . The MOs of  $\text{WSi}_{14}$  show much less hybridization than those of  $\text{CrSi}_{14}$ ; in fact, there is no hybridization between 5d orbitals and 6p orbitals. Still, all five 3d orbitals are filled and the W atom in  $\text{WSi}_{14}$  has a valence configuration of  $6s^25d^{10}6p^6$ , and hence follows the 18-electron rule.

The width of the 5d-bands was also calculated for each cluster in the series.  $\text{WSi}_6$ , which has no unpaired electrons unlike  $\text{CrSi}_6$ , was included. The results are shown in Figure 4.5.3 below. In general, the absolute energies of the HOMOs in the  $\text{WSi}_n$  series, and the start of the 5d-band, are lower in energy compared to those of the  $\text{CrSi}_n$  series. The trend in the 5d-band widths is similar to that of the 3d-band widths for  $\text{CrSi}_n$ , with narrower bands around 0.8 eV to 1.0 eV for most clusters and a large jump at  $\text{WSi}_{12}$ . A major difference arises at  $\text{WSi}_{13}$ . Due to its different geometry, the MOs of  $\text{WSi}_{13}$  are not akin to those of  $\text{WSi}_{12}$ , as was seen for  $\text{CrSi}_{13}$  and



CrSi<sub>12</sub>. The HOMO of WSi<sub>13</sub> is purely silicon in character, rather than being the 5d<sub>z<sup>2</sup></sub> orbital, so that the 5d-band does not extend to the HOMO. The 5d-band width for WSi<sub>14</sub> is, at 0.84 eV, almost exactly the same as that of CrSi<sub>14</sub>, and indicating a more spherical arrangement of silicon atoms around the W atom than found in WSi<sub>12</sub>.

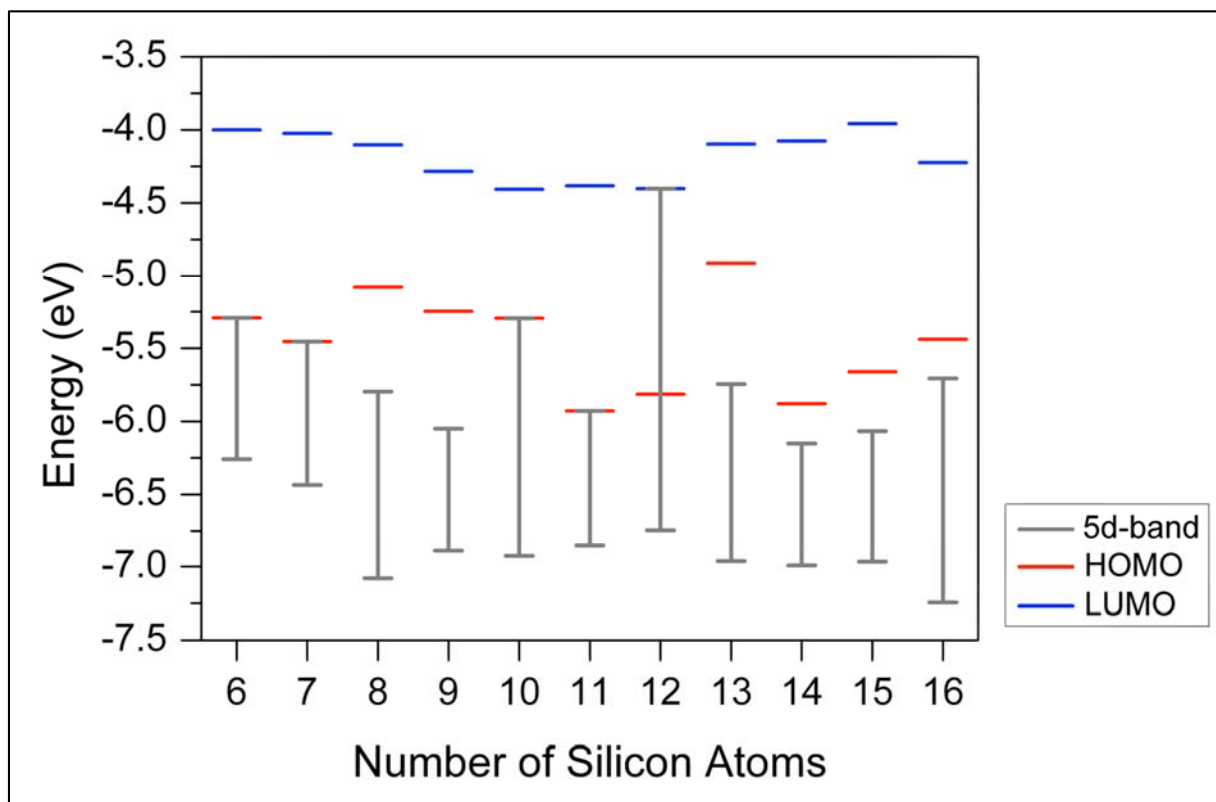


**Figure 4.5.3: The 5d-Bands of WSi<sub>n</sub>.** The bands formed by the 5d orbitals of tungsten are shown as vertical gray lines relative to the HOMO in red and the LUMO in blue for WSi<sub>n</sub> (n=6-16). The absolute energy of the orbitals is given on the y-axis.

## 4.6 Discussion

Based on the comparison of theoretically simulated photoelectron spectra with experimental results, the PBE functional was confirmed as an accurate choice for the study of TM-doped silicon clusters. Within this theoretical framework, the energetics of CrSi<sub>n</sub> showed that CrSi<sub>12</sub> and CrSi<sub>14</sub> were particularly stable clusters within the CrSi<sub>n</sub> (n=6-16) series. While CrSi<sub>14</sub> shows all the usual energetic markers of a magic cluster, CrSi<sub>12</sub> comes up short with only

a moderate HOMO-LUMO gap and a high ADE and VDE. This discrepancy was explained upon examining the molecular orbitals of  $\text{CrSi}_{12}$ . The  $3d_{z^2}$  orbital of Cr is unfilled, and makes up the LUMO of the entire cluster. The crystal-field splitting of the 3d orbitals in oblate  $D_{6h}$   $\text{CrSi}_{12}$  pushes the  $3d_{z^2}$  orbital up in energy, lending the cluster some magic properties despite possessing only 16 effective valence electrons. On the other hand,  $\text{CrSi}_{14}$  was revealed to follow the 18-electron rule with all 3d orbitals occupied. This pattern was also shown with  $\text{WSi}_n$ , although in the case of  $\text{WSi}_{12}$ , the crystal-field splitting of the 5d orbitals is much greater, leading to a larger HOMO-LUMO gap than seen in  $\text{CrSi}_{12}$ .  $\text{WSi}_{12}$  also showed lower values of ADE and VDE, and a very low hydrogen binding energy, giving it all the indicators of magicity. This may suggest that W, while possessing the same number of valence electrons, does not necessarily behave in the same manner as Cr in these clusters due to its differing size. These results also show that our intuition involving bonding from traditional chemistry does not always apply to clusters, which can exhibit non-electron precise bonding.

## 5 Conclusions

The main objective of the present work was to study the electronic principles that govern the stability and reactivity of two classes of clusters, namely ligated metal clusters and transition metal doped silicon clusters. Rules describing the electronic structure and reactivity patterns of clusters are important to the identification of stable species and appropriate methods of assembly that could be utilized in the building of nanoscale cluster-assembled materials. In the remainder of this chapter, the major findings for each type of cluster will be reviewed and its implications concerning electronic principles discussed.

The first study focused on aluminum clusters ligated with halogen atoms, specifically iodine atoms. Motivated by recent successes in stabilizing assemblies of metallic clusters through the addition of protecting ligands, this study questioned whether electron-withdrawing ligands such as iodine could also serve as activating species when attached to metal clusters. Previous studies on the reactivity of pure aluminum clusters showed that geometric defects cause irregularities in the charge density to manifest on the surface of the cluster, allowing for reaction with water or alcohols through complementary Lewis acid-base sites. The addition of ligands can also perturb the charge density of a cluster, perhaps resulting in similarly reactive sites. In the case of  $\text{Al}_{13}\text{I}_x^-$  ( $x=0-4$ ), the results showed that the addition of iodine ligands was not sufficient to induce reactivity with methanol due to the symmetrical charge distribution, which is maintained despite the addition of iodine. A higher energy isomer of  $\text{Al}_{13}\text{I}_2^-$  with the iodines attached to adjacent aluminum atoms, however, was reactive with methanol – the placement of the ligands resulted in complementary Lewis acid-base sites on the opposite side of the cluster. In the  $\text{Al}_{14}\text{I}_y^-$  ( $y=0-5$ ) series, clusters possessing more than one iodine atom react with methanol, but only at the ligated-atom site. This is especially interesting for the electronically closed-shell clusters

$\text{Al}_{14}\text{I}_3^-$  and  $\text{Al}_{14}\text{I}_5^-$ , neither of which reacts with oxygen. Furthermore, comparing the reactivity of the  $\text{Al}_{14}^-$  and  $\text{Al}_{14}\text{I}^-$  shows that the adatom must be ligated in order to react;  $\text{Al}_{14}^-$  reacts at other sites, but not at the bare adatom, while  $\text{Al}_{14}\text{I}^-$  will react with methanol at the ligated-adatom site. The stability of  $\text{Al}_{13}\text{I}_x^-$  species to methanol and reactivity of  $\text{Al}_{14}\text{I}_y^-$  species with methanol that was theoretically predicted by the work in this thesis was confirmed experimentally by the Castleman group at Penn State University.

The above results provide several insights into the reactivity of these clusters and the effect ligands have on reactivity in general. While the reactive higher energy isomer of  $\text{Al}_{13}\text{I}_2^-$  is unlikely to exist in experiment, this result showed that it is possible to induce such an active site on an unreactive cluster, such as  $\text{Al}_{13}^-$ , by the appropriate placement of ligands. From the  $\text{Al}_{14}\text{I}_y^-$  series, came the important result of the ligand-activated adatom – a geometric defect which alone is not an active site, but when ligated becomes reactive. Each of these ideas could be useful in the purposeful activation of other such clusters and in the design of cluster-assembled materials. Additionally, these results further demonstrate the differing mechanisms governing the reaction of these clusters with oxygen and protic species such as water and alcohols. Reactivity with oxygen is controlled by spin excitation energy, while reactivity with a protic environment is controlled by Lewis acid-base chemistry – specifically complementary active sites or ligand-activated adatoms whose strength and location can be modified by attaching ligands. For air stable cluster assemblies, one can use these to design clusters that are unreactive to air. On the other hand, for cluster assemblies with controlled reactive patterns, one can generate assemblies that can react with oxygen, protic environments, or both.

The second study examined the electronic principles that determine the stability of silicon clusters with an endohedral transition metal atom. Silicon is widely used in the electronics

industry and the possibility of producing cage-like silicon clusters encapsulating a transition metal atom, wherein the metal atom could retain its magnetic character, would be an important development. The use of transition metal doped silicon clusters is especially intriguing since the doping of bulk silicon with transition metal atoms beyond a few percent is difficult; cluster materials offer the unique possibility of changing the metal to silicon ratio by using designer clusters. Understanding the electronic principles that govern the stability of such silicon encapsulated transition metal clusters is the first step to develop these assemblies. The focus within this thesis was on  $\text{CrSi}_n$  ( $n=6-16$ ) clusters, and in particular  $\text{CrSi}_{12}$ . The stability of  $\text{CrSi}_{12}$  has previously been rationalized using both a split-CNFEG model and the 18-electron rule of transition metal chemistry; both involve Cr attaining an 18-electron shell closing by gaining one electron from each silicon atom in an electron-precise bonding scheme. The purpose of this study was to challenge both of these ideas with updated and more comprehensive calculations of energetic properties and through an extensive molecular orbital analysis of clusters of interest.

The energetic results for  $\text{CrSi}_n$  revealed  $\text{CrSi}_{12}$  to have only some of the traditional markers of a magic cluster, while  $\text{CrSi}_{14}$  was shown to possess all the markers. A comprehensive molecular orbital analysis showed that the CNFEG model, whether applied to the entire cluster or only to the chromium atom, did not accurately describe the electronic structure of  $\text{CrSi}_{12}$ , or explain its stability. Fragment analysis of the molecular orbitals of  $\text{CrSi}_{12}$  showed that the  $3d_{z^2}$  orbital of Cr is unfilled, and serves as the LUMO of the cluster. All other 3d orbitals are filled, as well as 4s and 4p, giving  $\text{CrSi}_{12}$  an effective valence count of 16. Due to the oblate structure of  $\text{CrSi}_{12}$ , its  $3d_{z^2}$  orbital is pushed up in energy relative to the others by crystal-field splitting. On the other hand,  $\text{CrSi}_{14}$  has all 3d orbitals filled, giving it an effective valence count of 18. Thus, while the 18-electron rule does not apply to  $\text{CrSi}_{12}$ , it does apply to  $\text{CrSi}_{14}$ . These results were,

for the most part, repeated in the  $WSi_n$  series. The crystal-field splitting in  $WSi_{12}$ , however, was much greater for the 5d orbitals of W than for the 3d orbitals of Cr. This leads to a very high HOMO-LUMO gap for  $WSi_{12}$  and a greater stability than seen for  $CrSi_{12}$ . The hydrogen binding energy for  $WSi_{12}$  matches well with the results of Hiura et al., which showed that unhydrogenated  $WSi_{12}^+$  is stable.

These results indicate that the metal-silicon bonds in these clusters are not electron-precise, as previously assumed and contrary to one's intuition from traditional chemistry. Most notably, the results of the molecular orbital analyses suggest that both the split-CNFEG view and the 18-electron rule are inaccurate or inadequate to describe the electronic structure of these clusters. Rather, the stability of  $TMSi_n$  is governed by crystal-field splitting of the d orbitals and by electron shell filling on the transition metal atom. This idea will have significance in the ongoing search for stable and usable silicon encapsulated transition metal clusters. The results also contribute to a conceptual understanding of the experimental results of Hiura et al; the absence of larger clusters in this experiment could be due to the fact that upon reaching twelve silicon atoms, the transition metal atom is completely interior and unavailable to react with silane further. Additionally, an incidental finding of this study was that the gradient-corrected functional PBE is sufficient for calculations on this class of clusters. This was done using time-dependent density functional theory to simulate the photoelectron spectra of anionic  $CrSi_n$  ( $n=6-12$ ) and comparing the results to recent experimental findings. Specifically, the PBE functional performed much more accurately than another popular functional used for these clusters, the hybrid B3LYP. These results provide a theoretical foundation for future studies, and lend confidence to the results given in this thesis.

Both ligated aluminum clusters and silicon encapsulated transition clusters remain important areas of study within the cluster field. Continuing work on iodized aluminum cluster reactivity includes using smaller  $Al_nI_m^-$  clusters as substrates; for example,  $Al_7^-$  with iodine ligands is currently underway. The possibility of breaking other types of bonds is also of interest. It was already mentioned that pure aluminum clusters can break a carbonyl bond, but this has yet to be extended to ligated clusters. Comparable studies of  $TMSi_n$  continue with different dopant atoms, including manganese and iron, and a similar analysis of  $TMSi_{16}$  clusters where (TM=V, Sc, Ti) would also be interesting, since these clusters show enhanced stability in experiments. Because most of the clusters studied in this thesis had a quenched magnetic moment, future studies will be undertaken that include doping with two transition metal atoms, which will more likely result in magnetic clusters, a major goal of designing silicon encapsulated transition metal clusters.

# Appendix A

**Table A-1: Orbitals Used in Plotting the Frontier Orbital Density of  $\text{Al}_{13}\text{I}_x^-$  ( $x=0-4$ ).**

Cluster	Occupied Orbitals	Unoccupied Orbitals
$\text{Al}_{13}^-$	HOMO, HOMO-1, HOMO-3, HOMO-5, HOMO-7, HOMO-9, HOMO-11	LUMO, LUMO+1, LUMO+3, LUMO+5, LUMO+7
$\text{Al}_{13}\text{I}^-$	HOMO	LUMO, LUMO+1, LUMO+3, LUMO+5, LUMO+7
$\text{Al}_{13}\text{I}_2^-$	HOMO, HOMO-1	LUMO, LUMO+1
$\text{Al}_{13}\text{I}_2^-_{\text{adj}}$	HOMO	LUMO
$\text{Al}_{13}\text{I}_3^-$	HOMO	LUMO+1, LUMO+3, LUMO+5
$\text{Al}_{13}\text{I}_4^-$	HOMO, HOMO-1	LUMO, LUMO+1, LUMO+3

The above table gives the occupied and unoccupied orbitals used to plot the occupied and unoccupied frontier orbital density, respectively. For those that list more than one orbital, the orbitals listed are nearly degenerate (within 0.008 eV). Occupied orbitals are given in relation to the highest occupied molecular orbital (HOMO) and unoccupied orbitals are given in relation to the lowest unoccupied molecular orbital (LUMO).

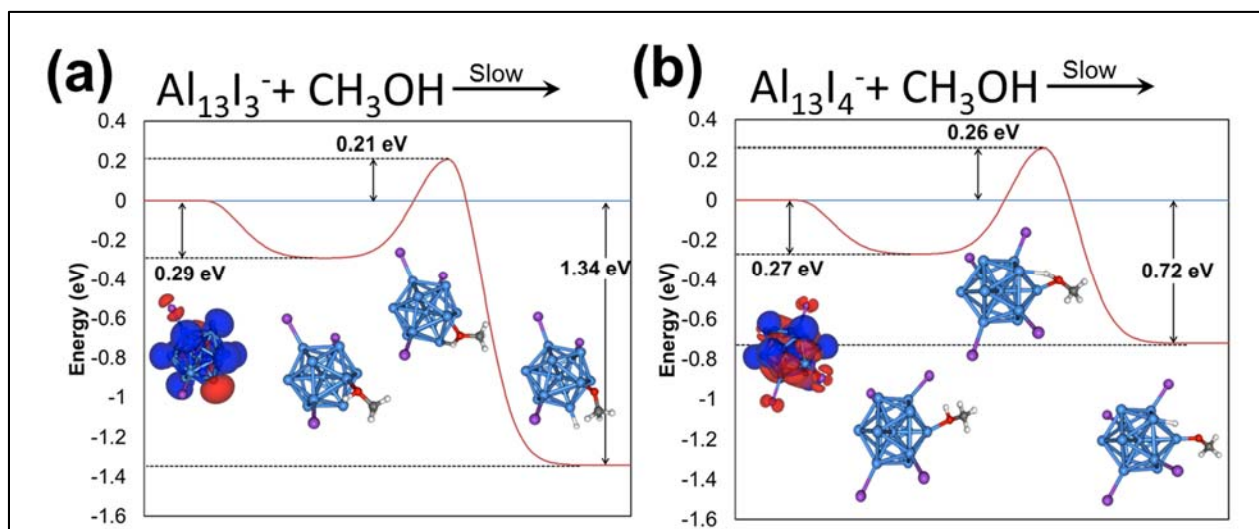


**Figure A-1: Lowest Energy Reaction Pathways of  $\text{Al}_{13}\text{I}_3^-$  and  $\text{Al}_{13}\text{I}_4^-$  with Methanol.** The above figure further demonstrates the reactive trends found in  $\text{Al}_{13}\text{I}^-$  and  $\text{Al}_{13}\text{I}_2^-$  in their ground states. The lowest energy reaction pathways of (a)  $\text{Al}_{13}\text{I}_3^-$  and (b)  $\text{Al}_{13}\text{I}_4^-$  with methanol are shown. The interpolated reaction pathway is shown as a red line, and the absolute values of  $E_B$ ,  $E_T$ , and  $E_R$  are indicated. The occupied (red) and unoccupied (blue) frontier orbital charge densities are shown on the ground state structure, and the geometries of the methanol-bound state, transition state, and final state are pictured with aluminum in blue, iodine in purple, oxygen in red, carbon in gray, and hydrogen in white. Figure adapted from Figure 2 of Ref. 114.



**Table A-2: Orbitals used in Plotting the Frontier Orbital Density of Al<sub>14</sub>I<sub>y</sub><sup>-</sup> (y=0-5).**

<b>Cluster</b>	<b>Occupied Orbitals</b>	<b>Unoccupied Orbitals</b>
Al <sub>14</sub> <sup>-</sup>	HOMO	LUMO+1
Al <sub>14</sub> I <sup>-</sup>	HOMO	LUMO
Al <sub>14</sub> I <sub>2</sub> <sup>-</sup>	HOMO	LUMO+1
Al <sub>14</sub> I <sub>3</sub> <sup>-</sup>	HOMO	LUMO, LUMO+1
Al <sub>14</sub> I <sub>4</sub> <sup>-</sup>	HOMO	LUMO+1, LUMO+3
Al <sub>14</sub> I <sub>5</sub> <sup>-</sup>	HOMO	LUMO

The above table gives the occupied and unoccupied orbitals used to plot the occupied and unoccupied frontier orbital density, respectively. For those that list more than one orbital, the orbitals listed are nearly degenerate (within 0.008 eV). Occupied orbitals are given in relation to the highest occupied molecular orbital (HOMO) and unoccupied orbitals are given in relation to the lowest unoccupied molecular orbital (LUMO). Note that in comparison to the Al<sub>13</sub>I<sub>x</sub><sup>-</sup> series, there is less orbital degeneracy in the Al<sub>14</sub>I<sub>y</sub><sup>-</sup> series, due to its lowered symmetry.

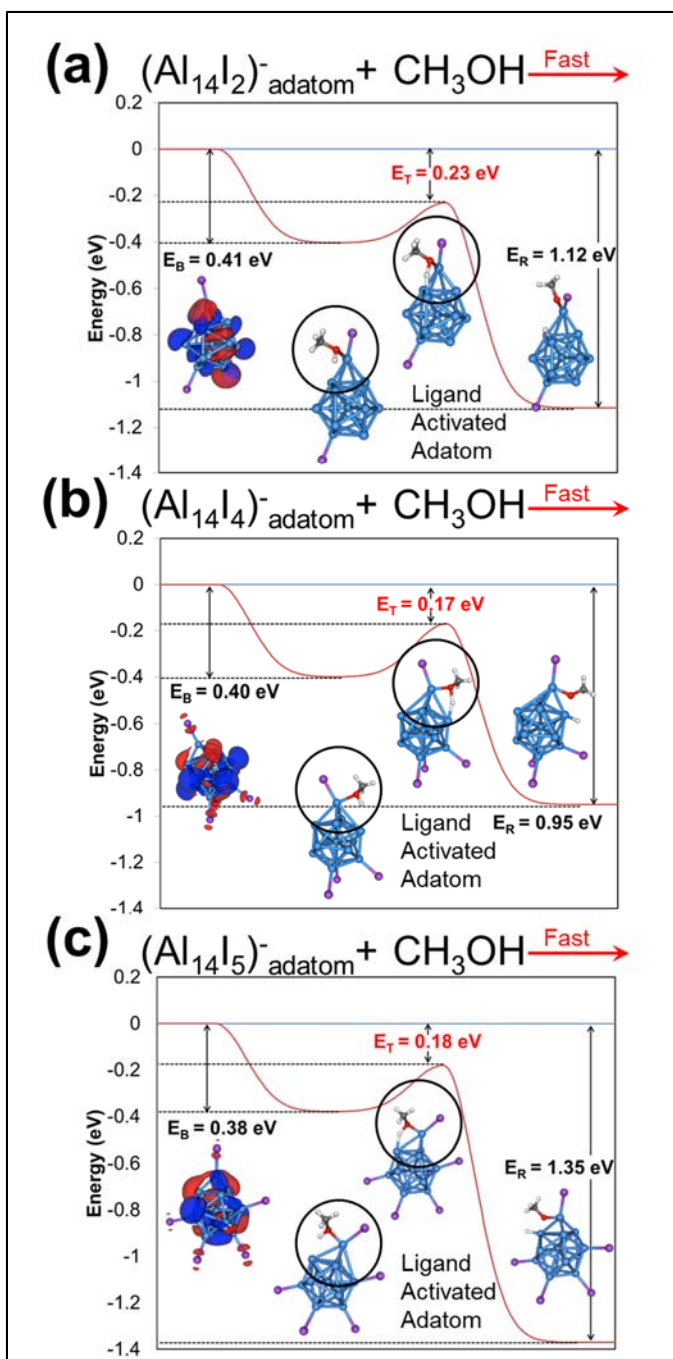


**Figure A-2: Lowest Energy Reaction Pathways of  $\text{Al}_{14}\text{I}_2^-$ ,  $\text{Al}_{14}\text{I}_4^-$ , and  $\text{Al}_{14}\text{I}_5^-$  with Methanol.** The figure shows the reaction pathway at the ligated adatom for (a)  $\text{Al}_{14}\text{I}_2^-$ , (b)  $\text{Al}_{14}\text{I}_4^-$ , and (c)  $\text{Al}_{14}\text{I}_5^-$ . This was the only site at which these clusters reacted with methanol. The interpolated reaction pathway is shown as a red line, and the absolute values of  $E_B$ ,  $E_T$ , and  $E_R$  are indicated. The occupied (red) and unoccupied (blue) frontier orbital charge densities are shown on the ground state structure, and the geometries of the methanol-bound state, transition state, and final state are pictured with aluminum in blue, iodine in purple, oxygen in red, carbon in gray, and hydrogen in white. Figure adapted from Figure 2 of Ref. 114.

## Appendix B

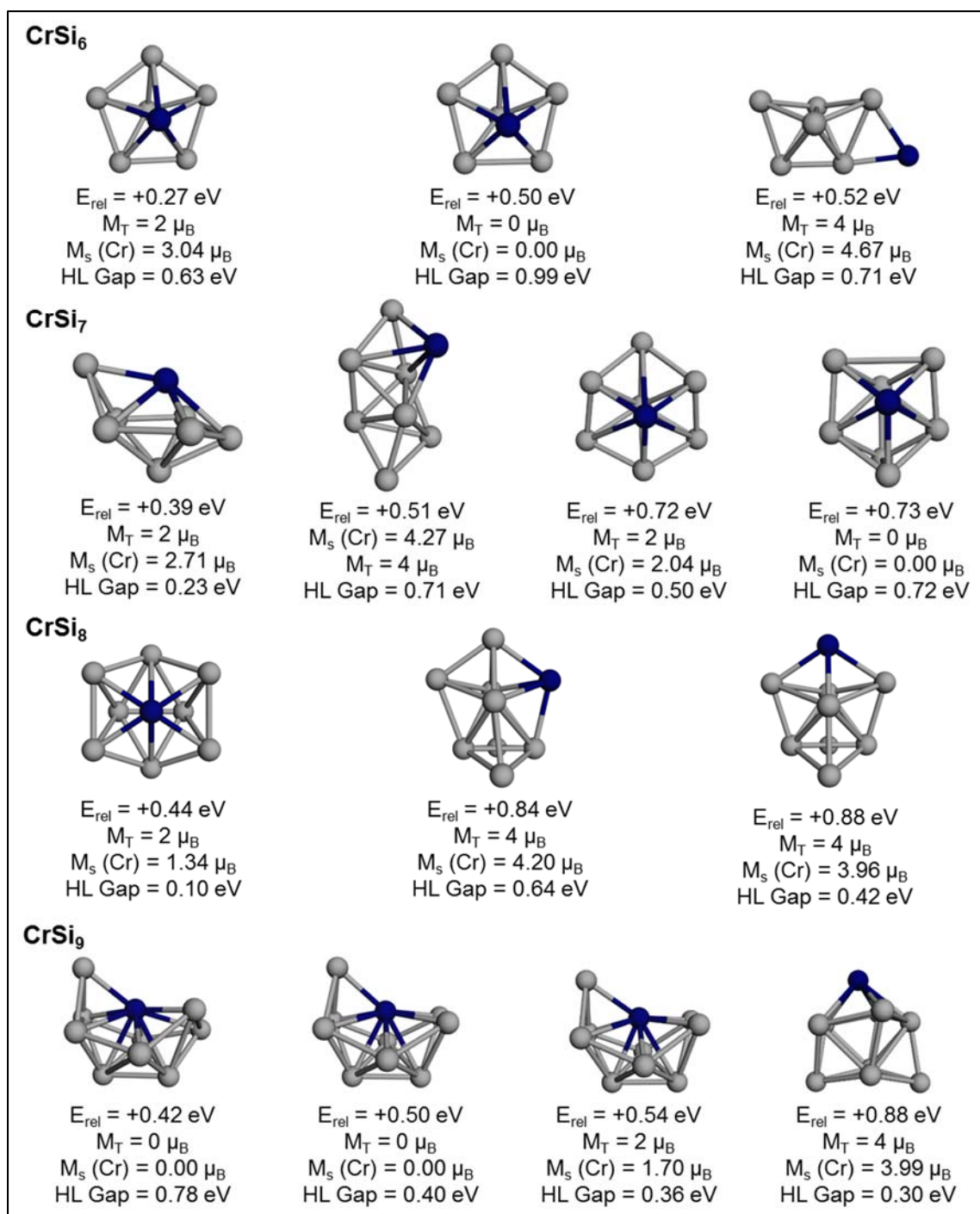


**Figure B-1: Higher Energy Isomers of CrSi<sub>n</sub> (n=6-9).** The higher energy isomers within 1.0 eV of the ground state are shown, with silicon atoms in gray and chromium atoms are shown in dark blue. The energies,  $E_{\text{rel}}$ , are given relative to the corresponding ground states shown in Figure 4.2.1. The total magnetic moment,  $M_{\text{T}}$ , local magnetic moment on the chromium atom,  $M_{\text{Cr}}$ , and HOMO-LUMO gap are given for each cluster.

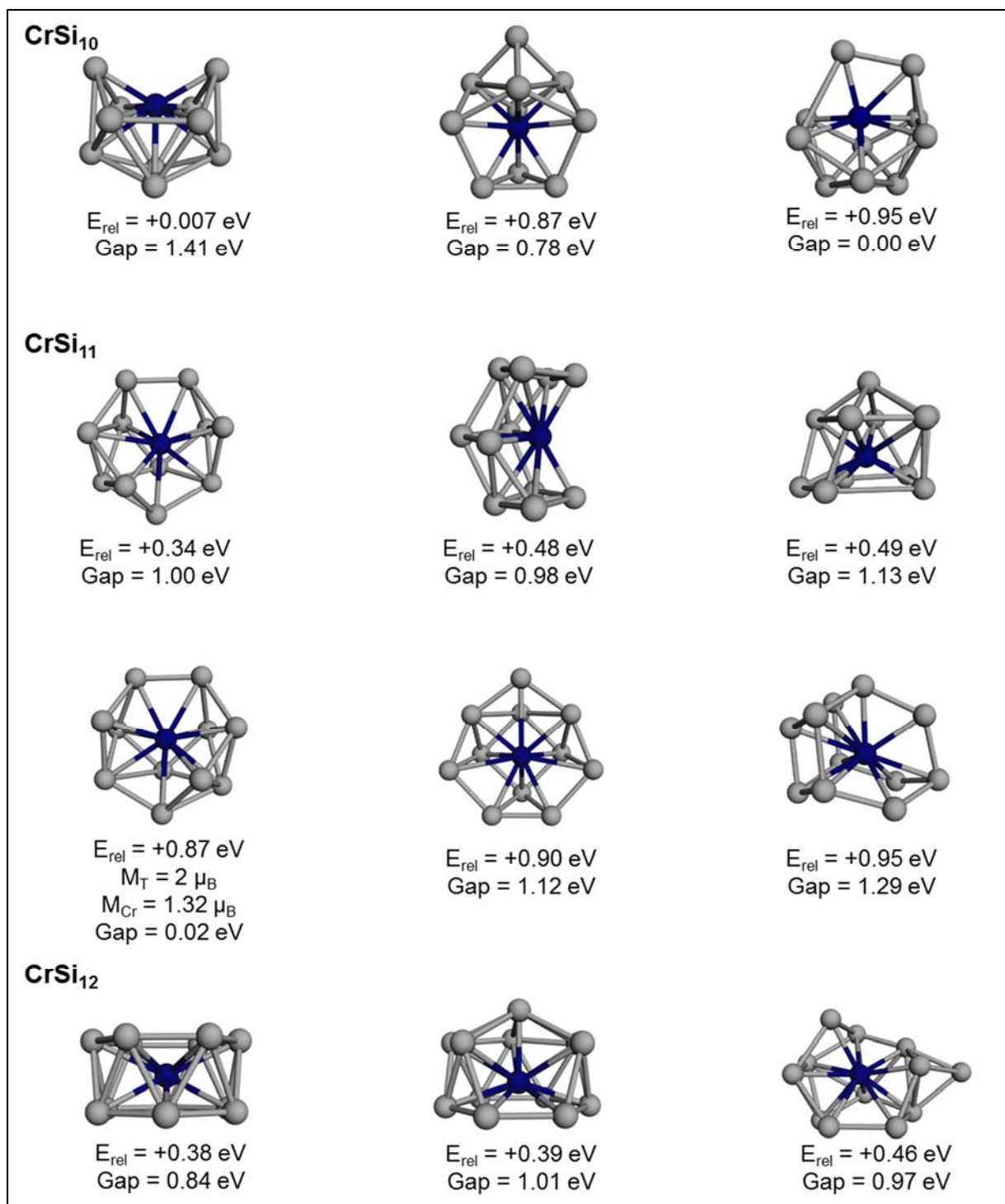


**Figure B-2: Higher Energy Isomers of CrSi<sub>n</sub> (n=10-12).** The higher energy isomers within 1.0 eV of the ground state are shown, with silicon atoms in gray and chromium atoms are shown in dark blue. The energies,  $E_{\text{rel}}$ , are given relative to the corresponding ground states shown in Figure 4.2.1. The total magnetic moment,  $M_{\text{T}}$ , local magnetic moment on the chromium atom,  $M_{\text{Cr}}$ , and HOMO-LUMO gap are given for each cluster.

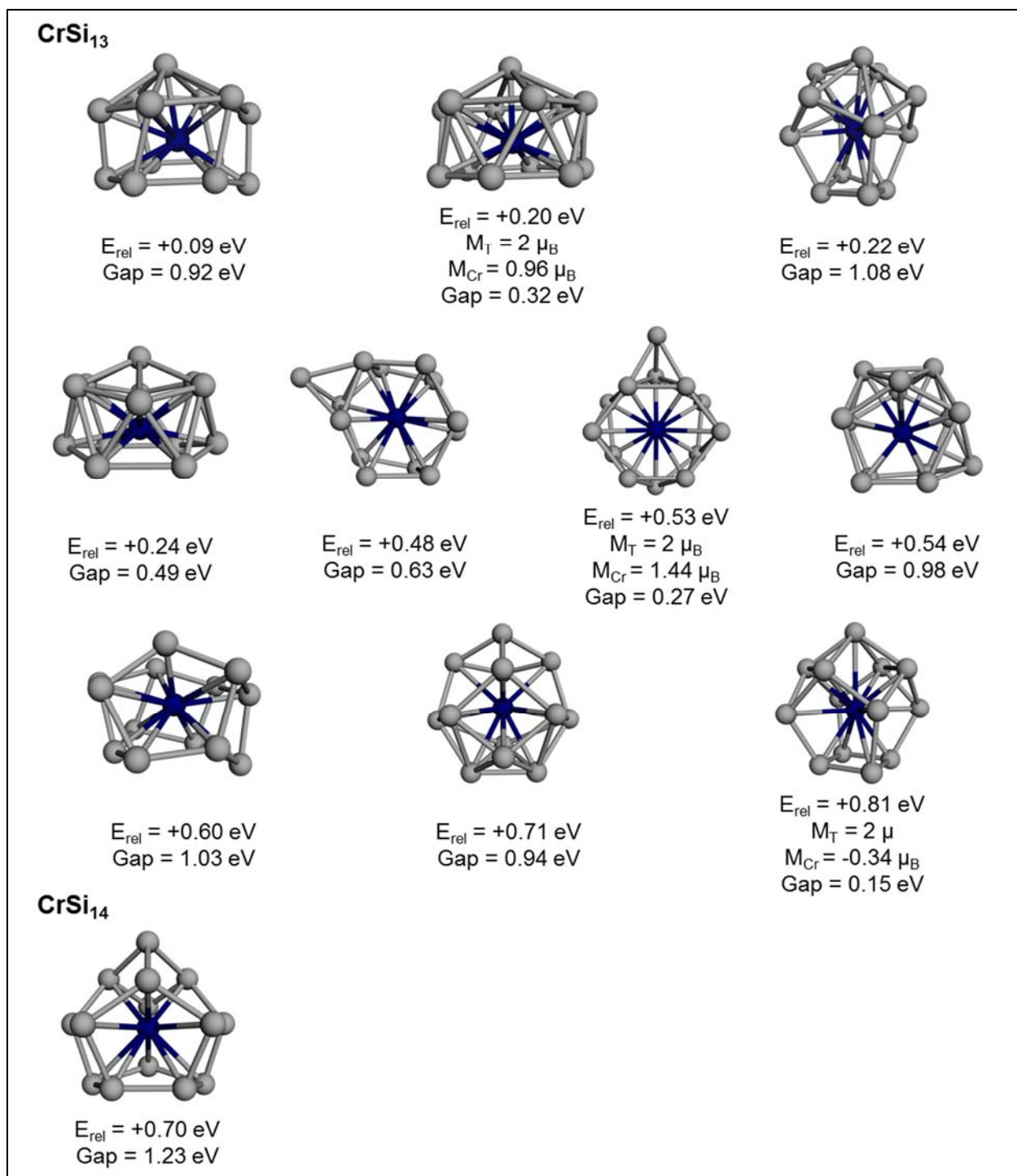


**Figure B-3: Higher Energy Isomers of CrSi<sub>13</sub> and CrSi<sub>14</sub>.** The higher energy isomers within 1.0 eV of the ground state are shown, with silicon atoms in gray and chromium atoms are shown in dark blue. The energies,  $E_{\text{rel}}$ , are given relative to the corresponding ground states shown in Figure 4.2.1. The total magnetic moment,  $M_{\text{T}}$ , local magnetic moment on the chromium atom,  $M_{\text{Cr}}$ , and HOMO-LUMO gap are given for each cluster.

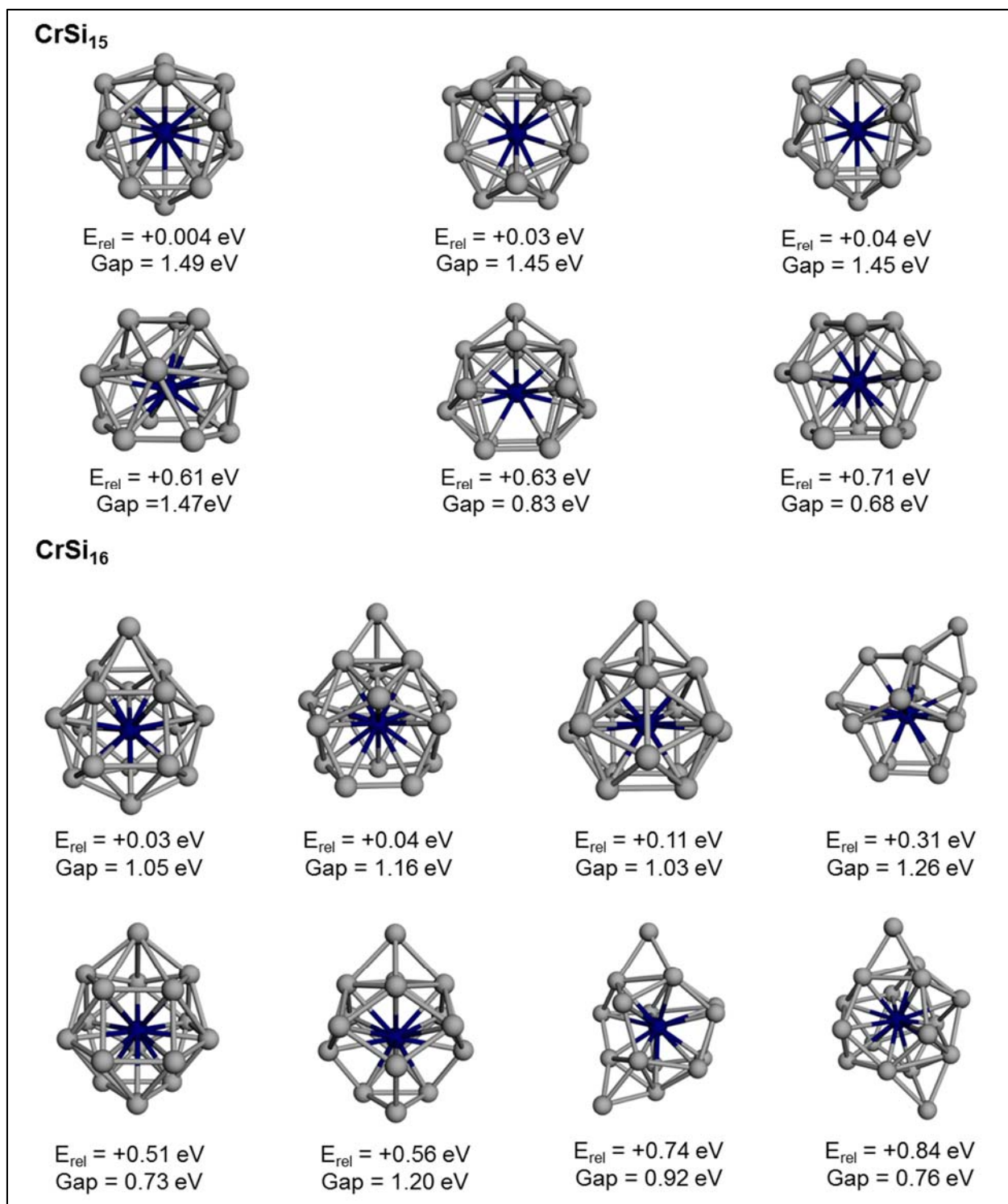


**Figure B-4: Higher Energy Isomers of CrSi<sub>15</sub> and CrSi<sub>16</sub>.** The higher energy isomers within 1.0 eV of the ground state are shown, with silicon atoms in gray and chromium atoms are shown in dark blue. The energies,  $E_{rel}$ , are given relative to the corresponding ground states shown in Figure 4.2.1. The total magnetic moment,  $M_T$ , local magnetic moment on the chromium atom,  $M_{Cr}$ , and HOMO-LUMO gap are given for each cluster.

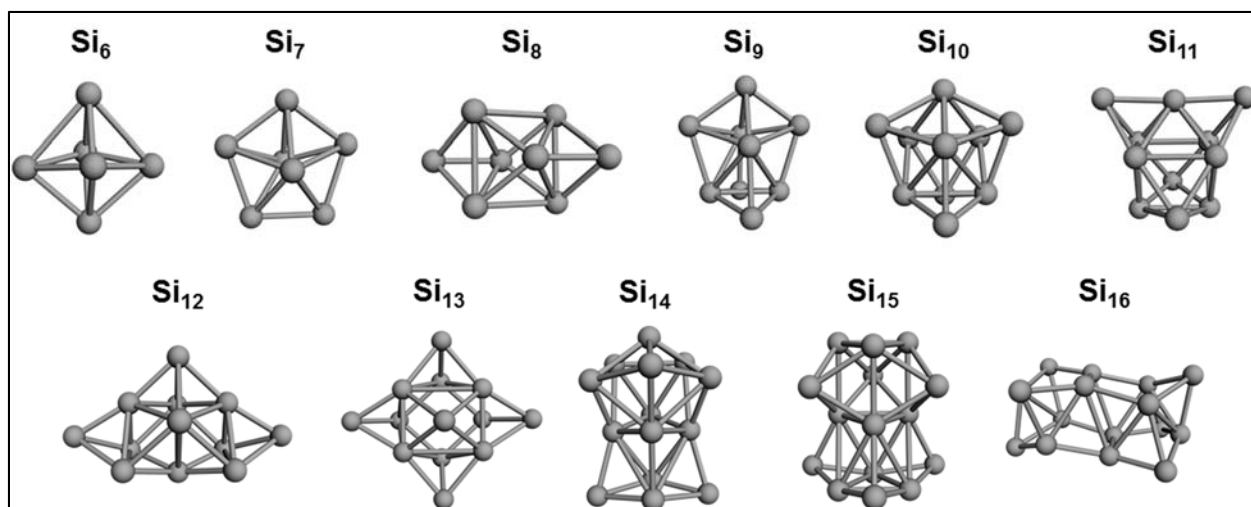


**Figure B-5: Ground State Geometries of Pure Silicon Clusters.** The lowest energy isomers of  $\text{Si}_n$  ( $n=6-16$ ) are shown. The energies of these isomers were used in calculating the Cr embedding energy.

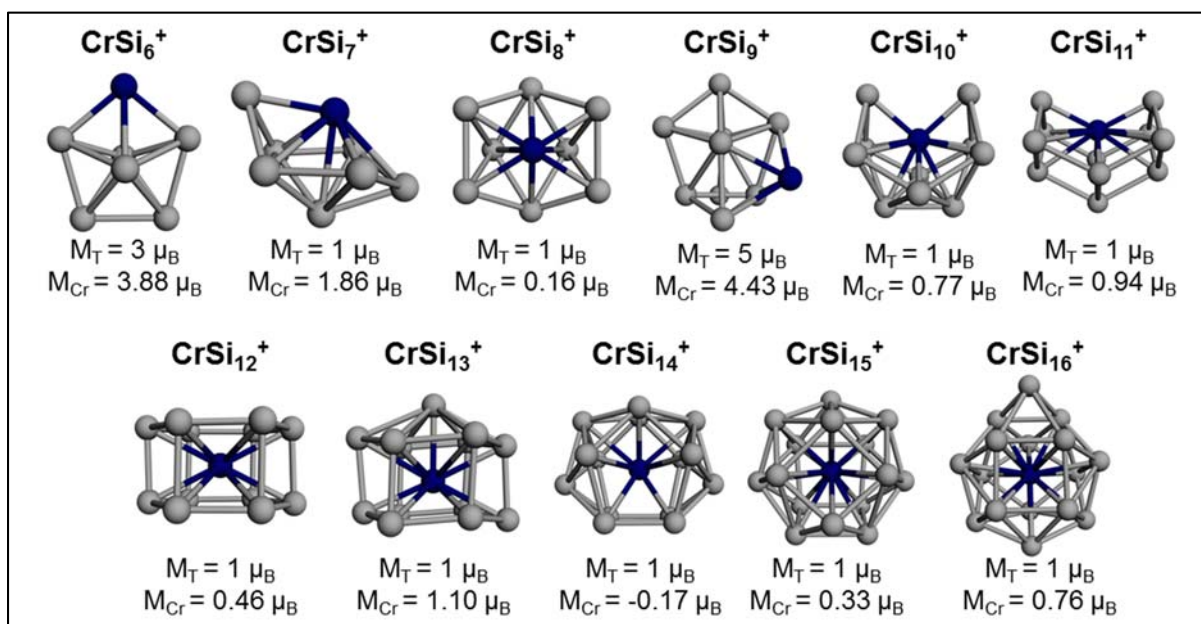


**Figure B-6:  $\text{CrSi}_n$  Cation Ground States.** The lowest energy structures of  $\text{CrSi}_n^+$  for  $n=6-16$ . The energy of these structures was used in the calculation of the ionization potentials. The total magnetic moment and the local magnetic moment on Cr are shown for each cluster. Figure adapted from Supplemental Information of Ref \*\*.

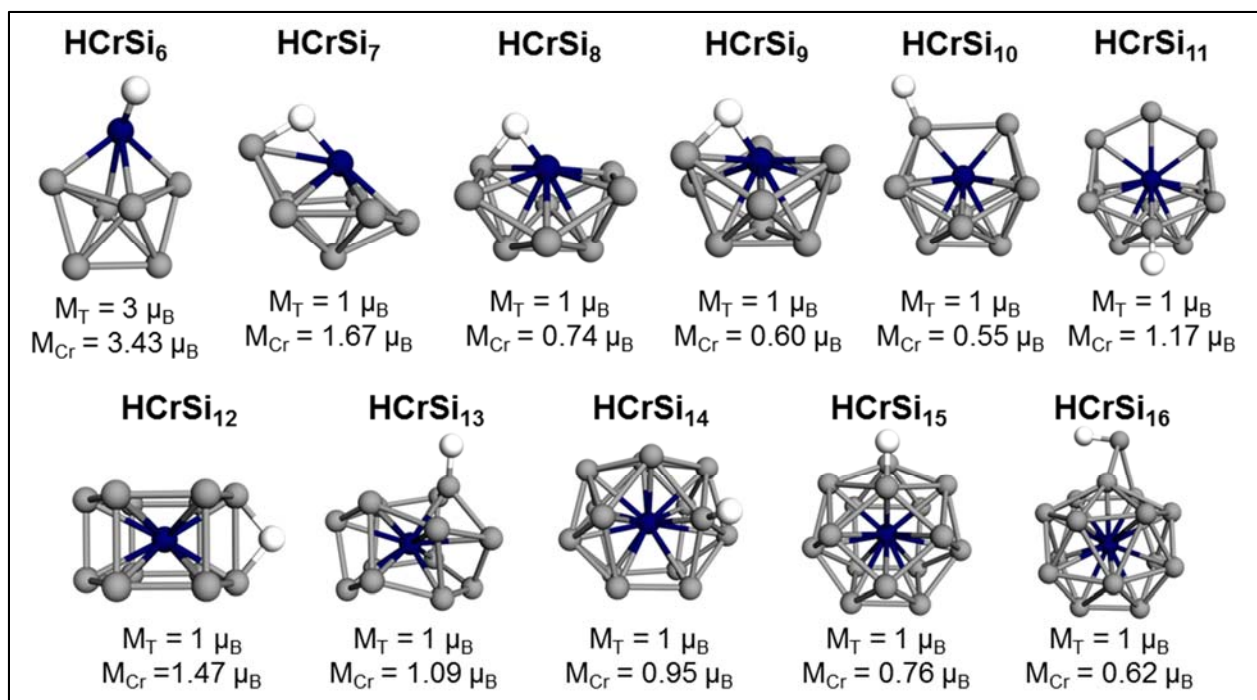


**Figure B-7: Hydrogen Bound CrSi<sub>n</sub> Ground States.** The lowest energy structures of HCrSi<sub>n</sub> for n=6-16. Silicon atoms are gray, chromium atoms are dark blue, and hydrogen atoms are white. The energies of these structures was used to calculate the hydrogen binding energy. The total magnetic moment and the local magnetic moment on Cr are given. Figure adapted from Figure S5 of Ref. \*\*.

**Table B-1: Calculated Properties of CrSi<sub>n</sub> (n=6-16).**

# Si atoms	HOMO-LUMO	$\Delta_{Si}$	$\Delta_{Cr}$	VDE	ADE	IP	H BE
6	0.86	--	2.22	2.93	2.54	6.81	2.26
7	1.12	4.05	1.81	2.49	2.44	7.22	2.6
8	0.95	4.33	3.07	2.62	2.54	7.17	2.52
9	1.09	4.3	2.96	2.8	2.67	7.29	2.54
10	1.41	4.38	2.63	2.83	2.66	7.35	2.23
11	1.37	4.26	3.77	2.88	2.77	7.29	2.25
12	0.97	4.55	4.2	3.05	3.05	7.43	2.35
13	0.84	3.91	4.59	3.31	2.93	6.4	2.42
14	1.48	5.04	5.23	2.92	2.81	7.59	2.06
15	1.21	4.35	5.39	2.86	2.75	7.06	1.97
16	1.48	3.56	5.74	3.14	2.6	6.24	2.15

The above table gives the numerical values used to generate the graphs in Figure 4.4.2, including the HOMO-LUMO gap, silicon binding energy, chromium embedding energy, vertical and adiabatic detachment energies, ionization potential, and hydrogen binding energy. All values are given in eV.



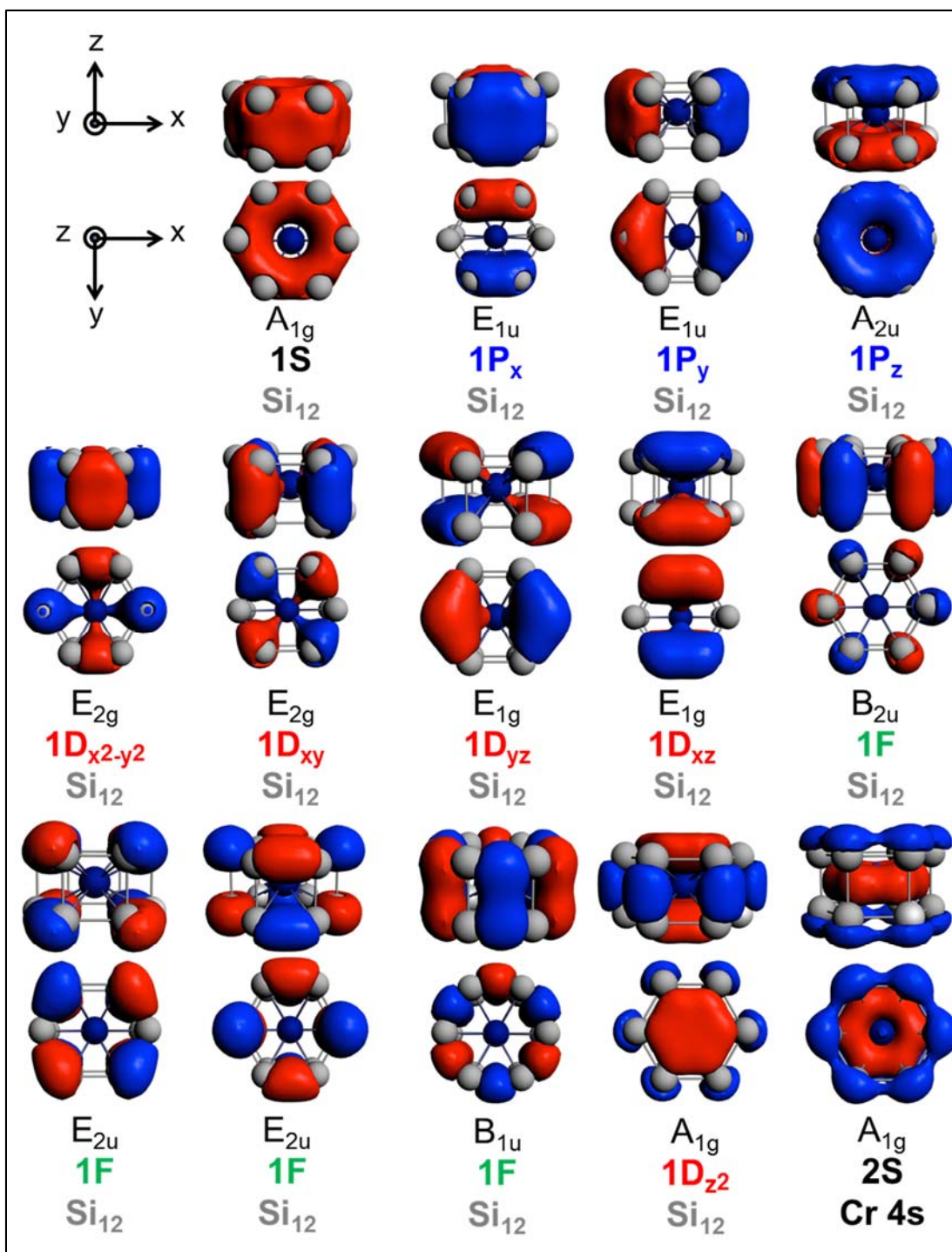


**Figure B-8: Occupied Molecular Orbitals of  $\text{CrSi}_{12}$  (1).** Side and top views of the first fourteen occupied orbitals of  $D_{6h}$   $\text{CrSi}_{12}$ . The symmetry label, CNFEG model orbital designation, and chromium/silicon character designation are given below the images.

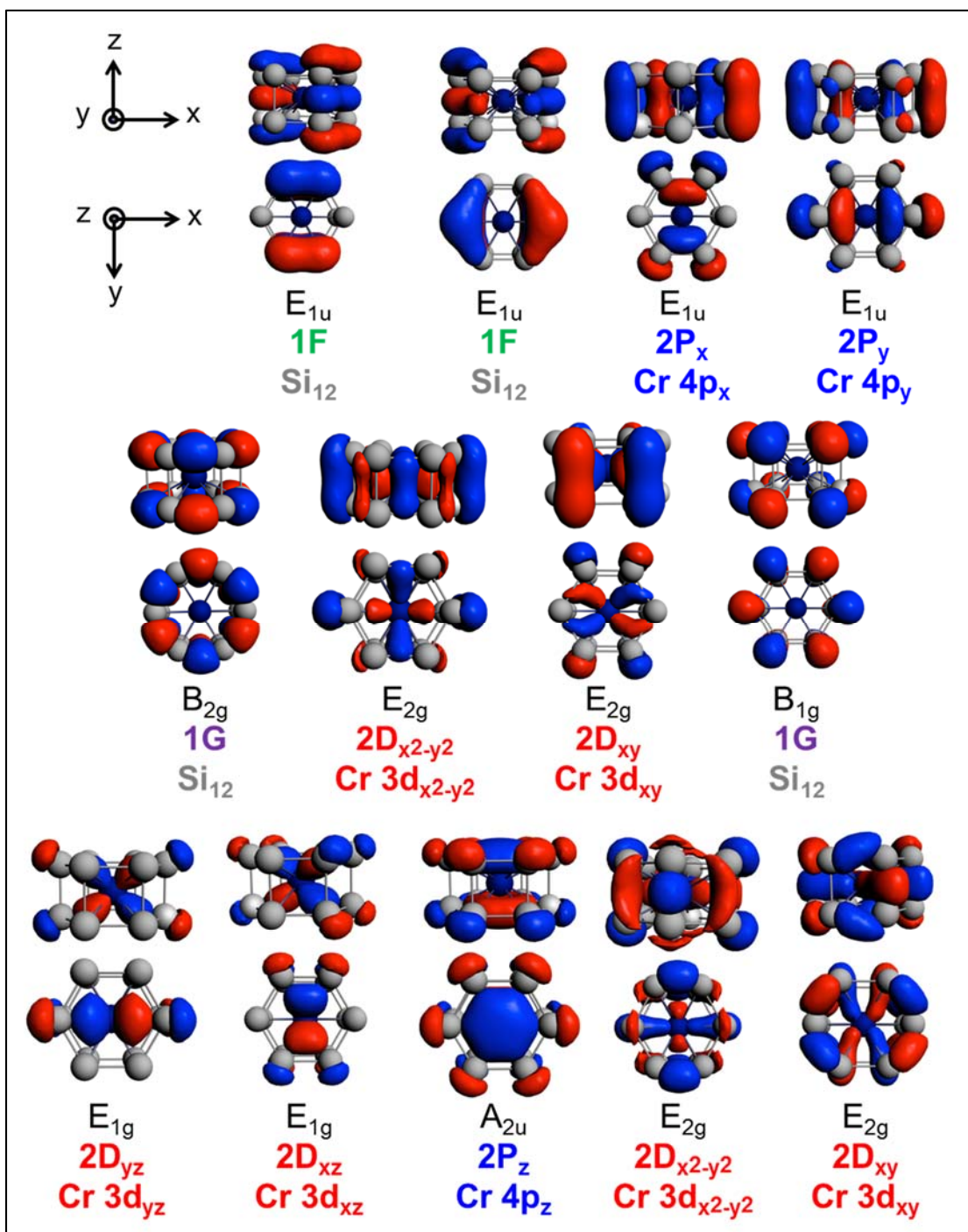


**Figure B-9: Occupied Molecular Orbitals of  $\text{CrSi}_{12}$  (2).** Side and top views of the remaining thirteen occupied orbitals of  $D_{6h}$   $\text{CrSi}_{12}$ . The symmetry label, CNFEG model orbital designation, and chromium/silicon character designation are indicated below the images.

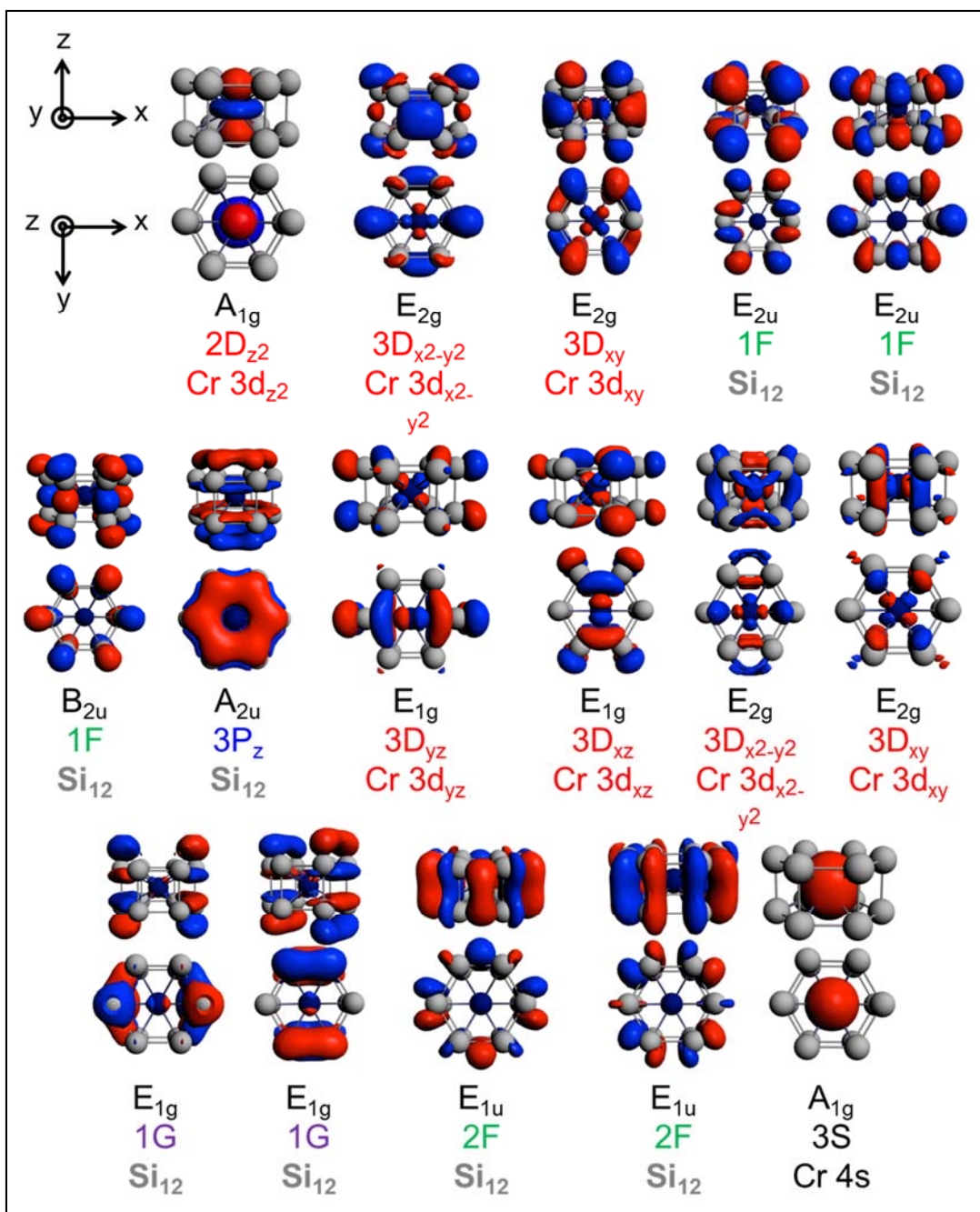


**Figure B-10: Unoccupied Molecular Orbitals of CrSi<sub>12</sub>.** Side and top views of the sixteen lowest energy unoccupied orbitals of D<sub>6h</sub> CrSi<sub>12</sub>. The symmetry label, CNFEG model orbital designation, and the chromium/silicon character designation are indicated under the images.

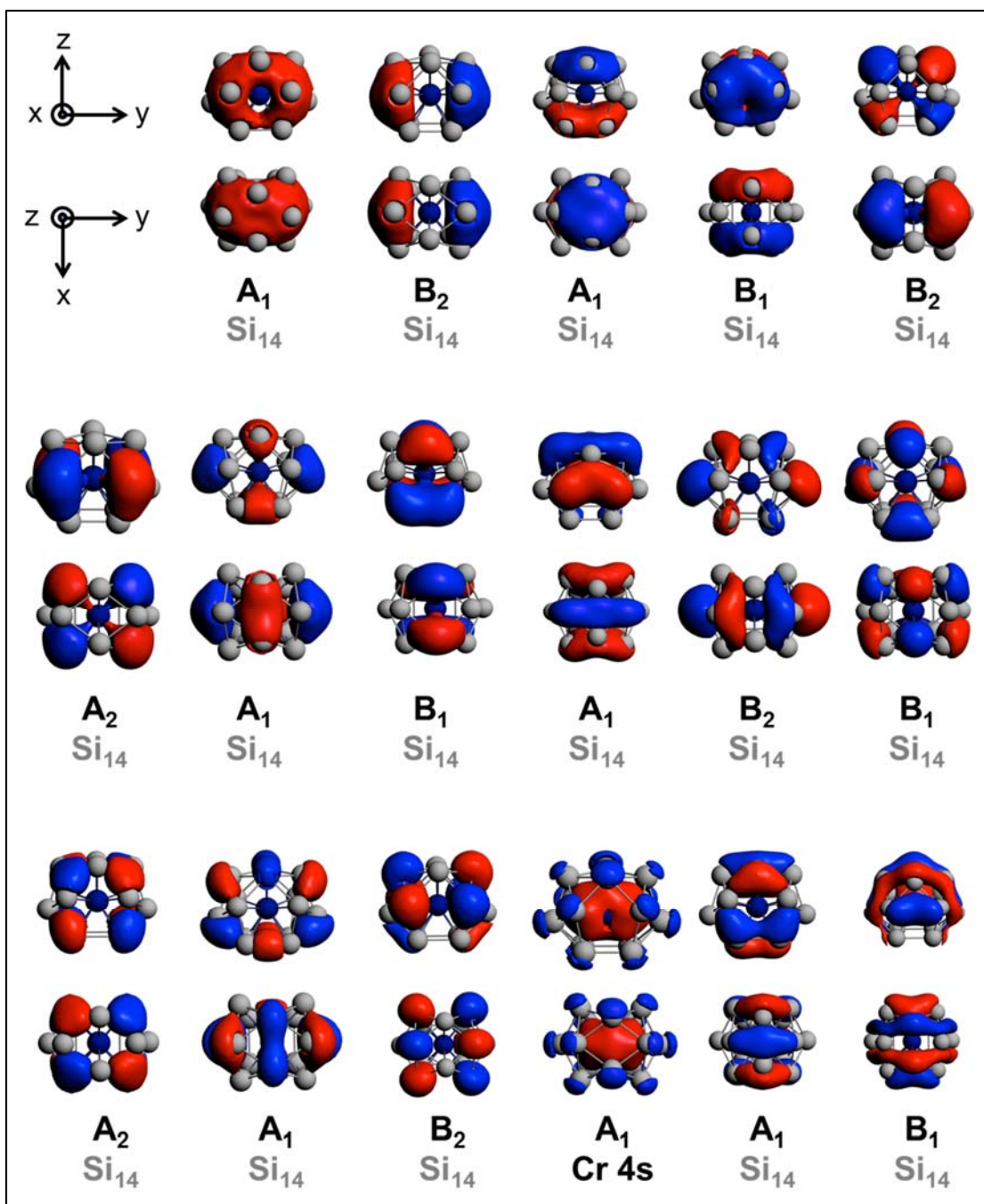


**Figure B-11: Occupied Molecular Orbitals of  $\text{CrSi}_{14}$  (1).** Side and top views of the first seventeen occupied orbitals of  $C_{2v}$   $\text{CrSi}_{14}$ . Symmetry labels and chromium/silicon designations are given.

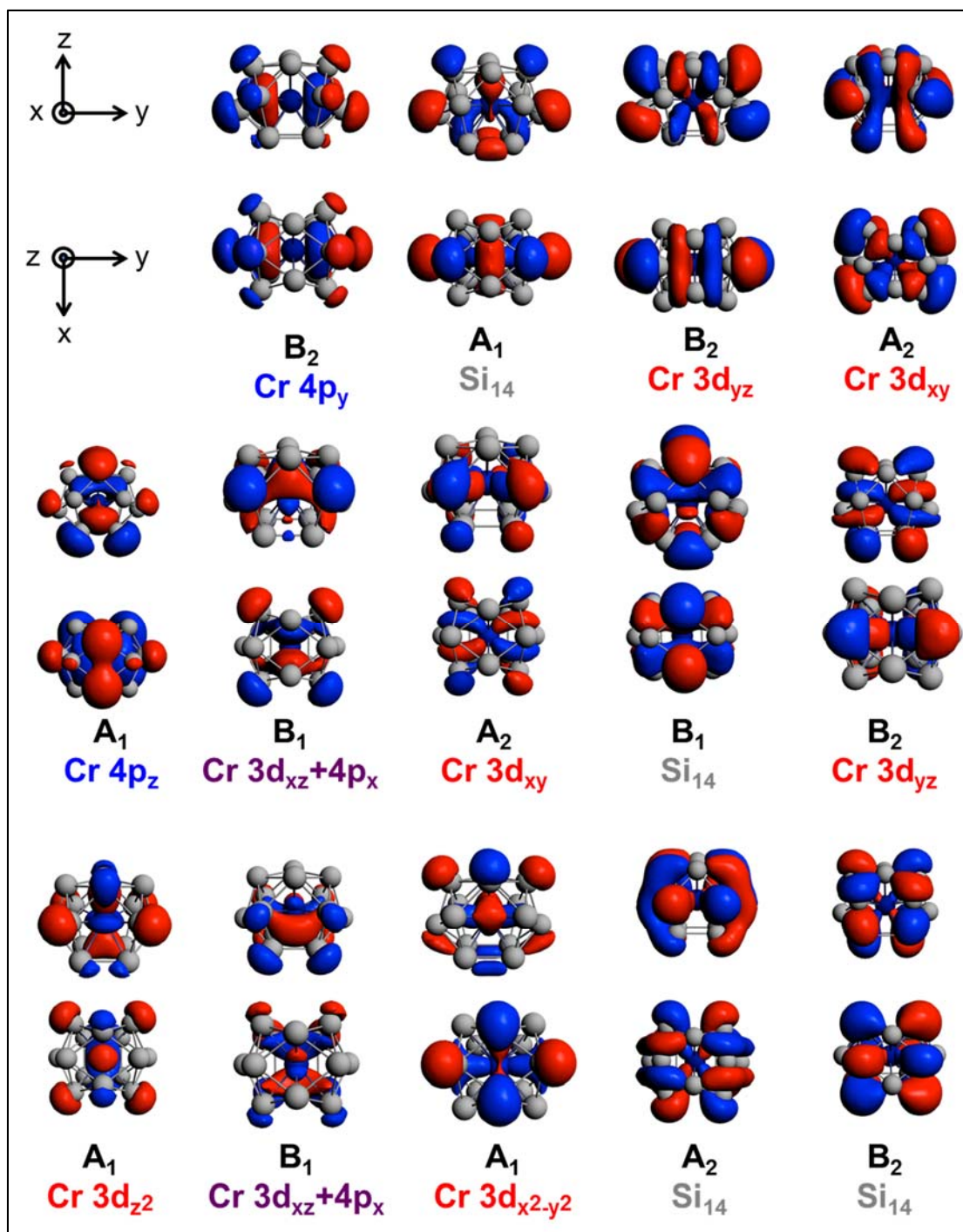


**Figure B-12: Occupied Molecular Orbitals of  $\text{CrSi}_{14}$  (2).** Side and top views of the first seventeen occupied orbitals of  $\text{C}_{2v}$   $\text{CrSi}_{14}$ . Symmetry labels and chromium/silicon designations are given.

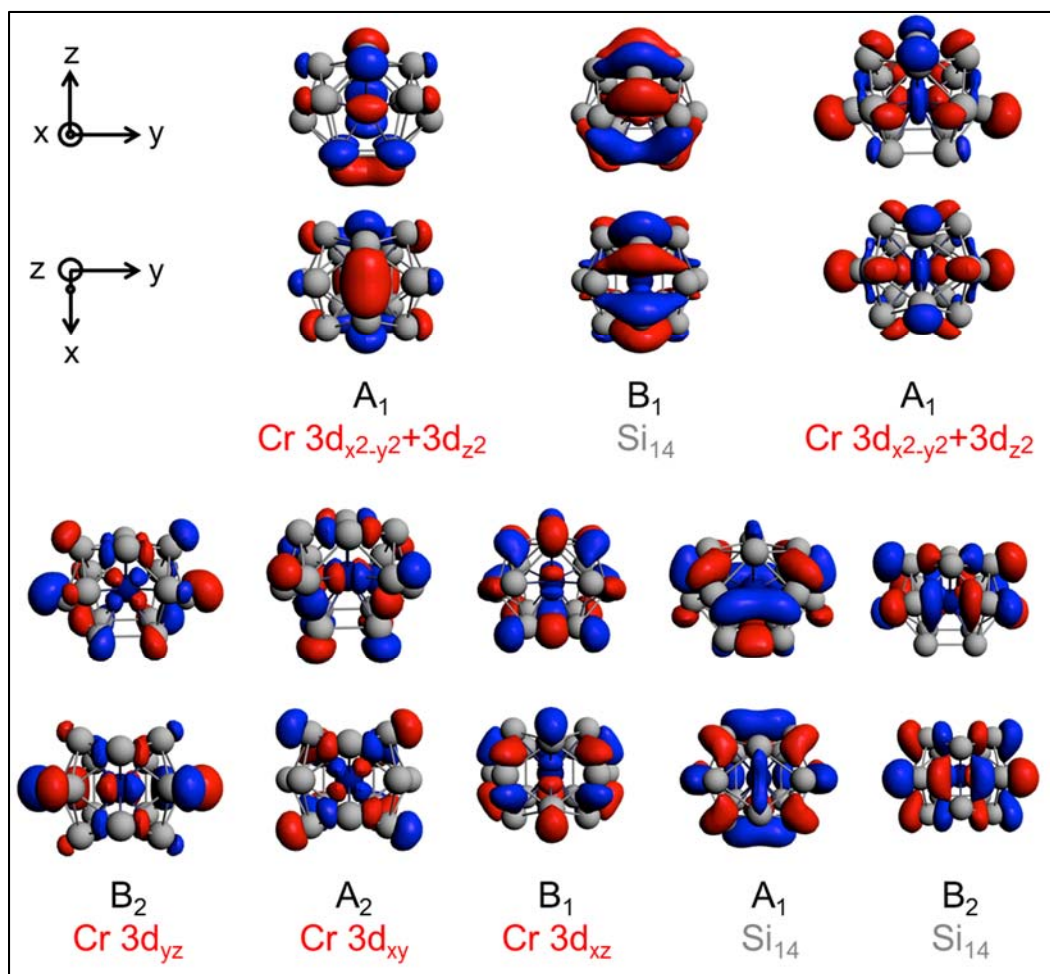


**Figure B-13: Unoccupied Molecular Orbitals of  $\text{CrSi}_{14}$ .** Side and top views of the first eight unoccupied molecular orbitals of  $C_{2v}$   $\text{CrSi}_{14}$ . The symmetry label and chromium/silicon character designation are included.

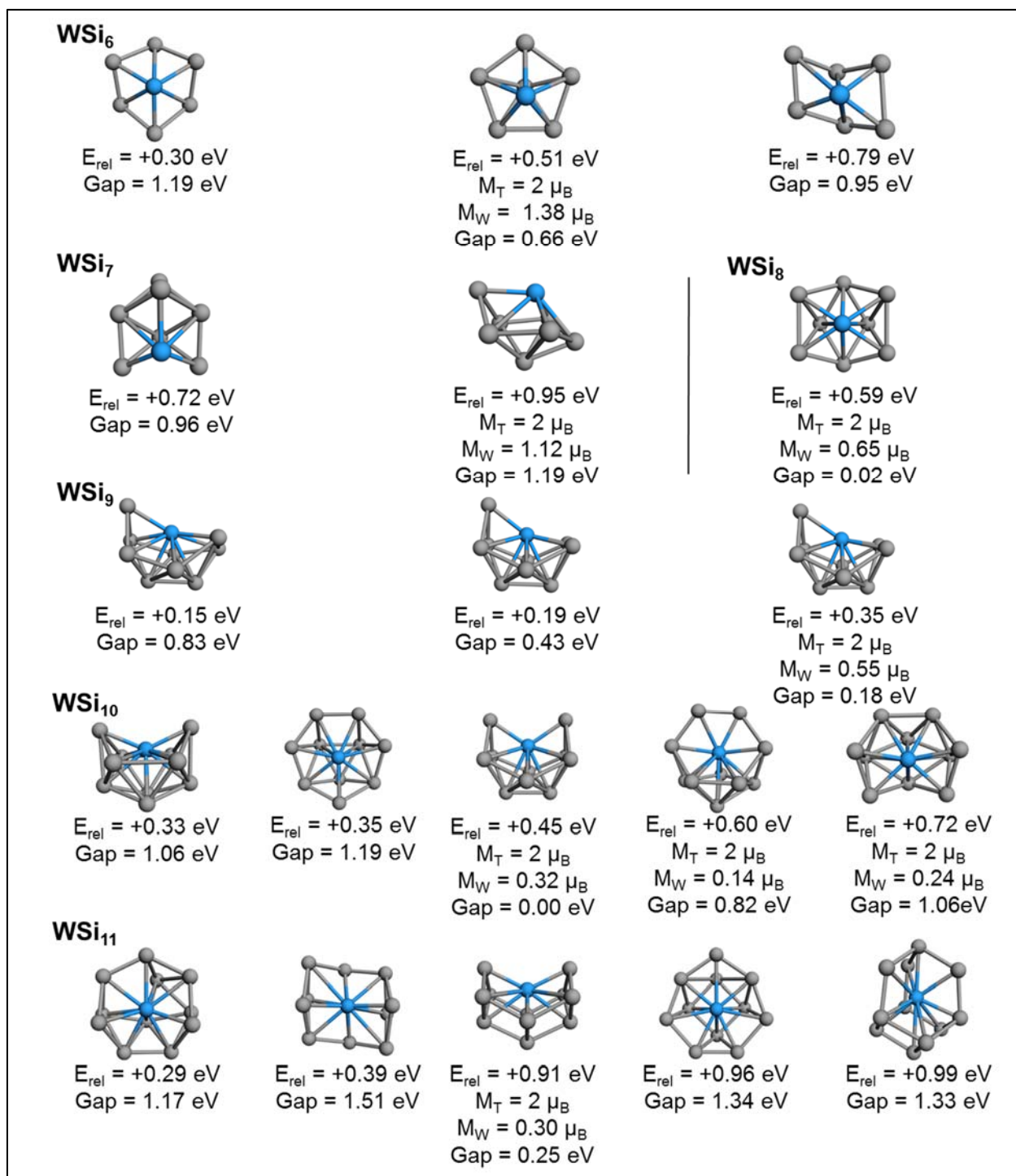


**Figure B-14: Higher Energy Isomers of WSi<sub>n</sub> (n=6-11).** Structures within 1.0 eV of the ground state given in Figure 4.5.1 are shown with silicon in gray and tungsten in blue. The energy is given relative to the ground state. For those geometries with a non-zero magnetic moment, the total magnetic moment,  $M_T$ , and local magnetic moment on tungsten,  $M_W$ , are given. HOMO-LUMO gaps are given for all geometries.

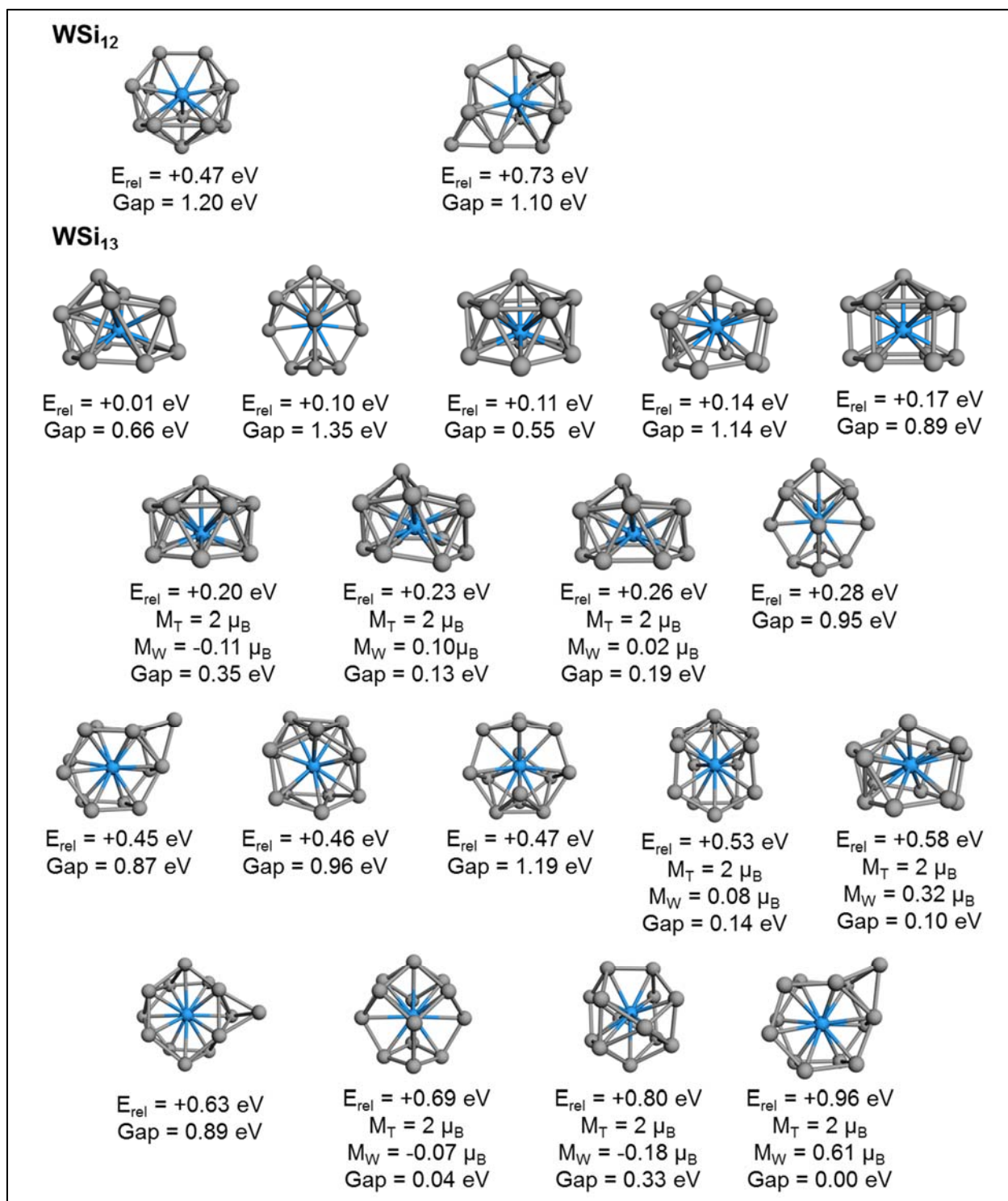


**Figure B-15: Higher Energy Isomers of WSi<sub>n</sub> (n=12, 13).** Structures within 1.0 eV of the ground state shown in Figure 4.5.1 are shown with silicon in gray and tungsten in blue. The energy is given relative to the ground state. For those geometries with a non-zero magnetic moment, the total magnetic moment,  $M_T$ , and local magnetic moment on tungsten,  $M_W$ , are given. HOMO-LUMO gaps are given for all geometries.



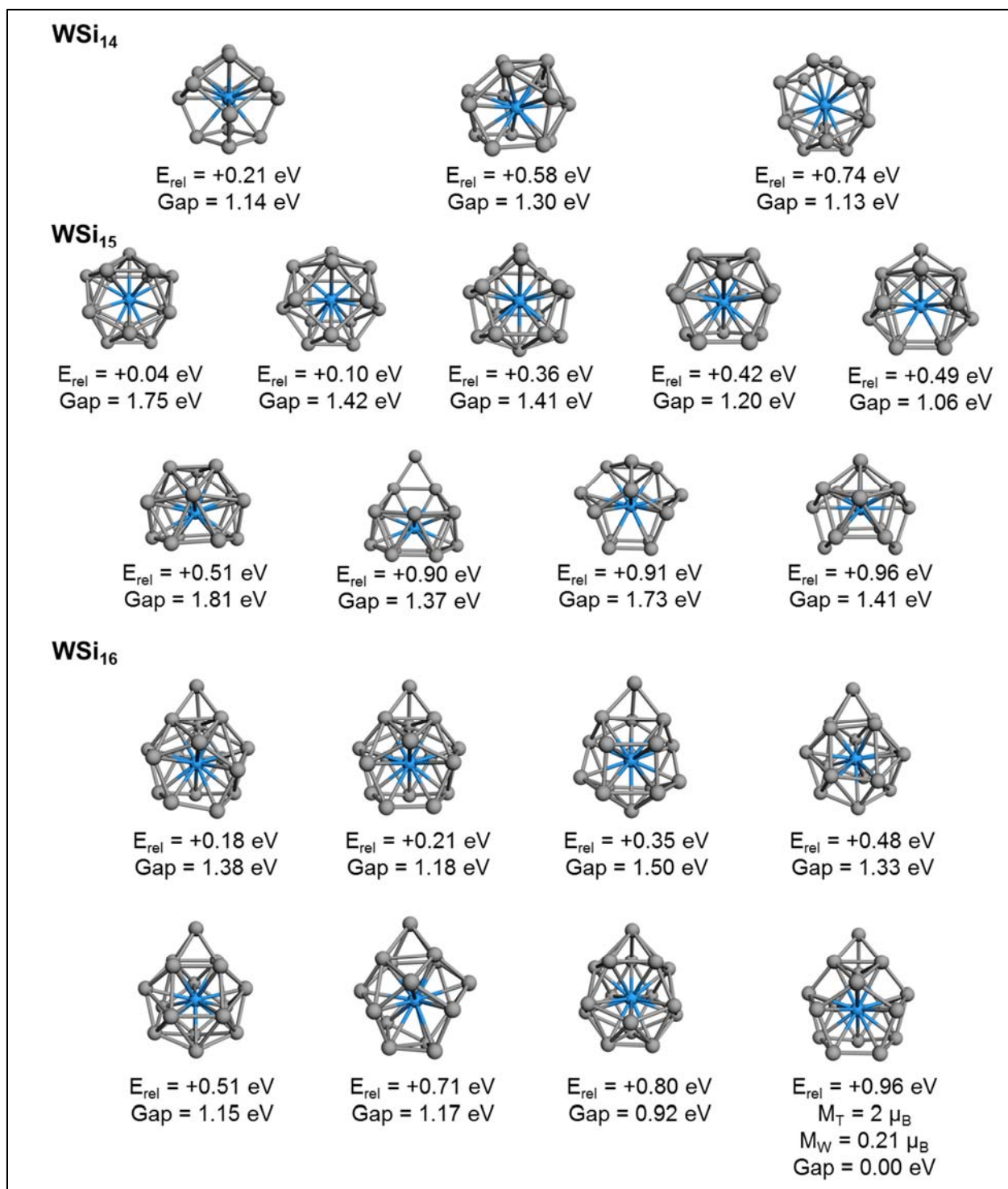


**Figure B-16: Higher Energy Isomers of WSi<sub>n</sub> (n=14-16).** Structures within 1.0 eV of the ground state shown in Figure 4.5.1 are shown with silicon in gray and tungsten in blue. The energy is given relative to the ground state. For those geometries with a non-zero magnetic moment, the total magnetic moment,  $M_{\text{T}}$ , and local magnetic moment on tungsten,  $M_{\text{W}}$ , are given. HOMO-LUMO gaps are given for all geometries.

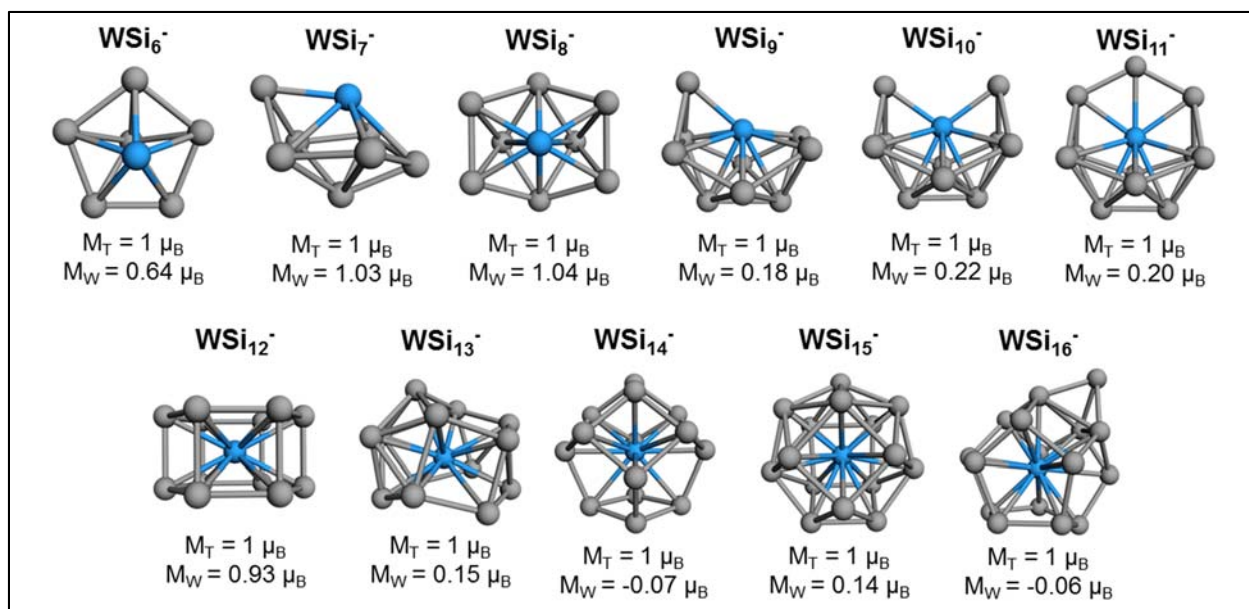


**Figure B-17: Anionic Ground States of WSi<sub>n</sub> (n=6-16).** The structures of the lowest-energy WSi<sub>n</sub><sup>-</sup> anions are shown with silicon in gray and tungsten in blue. The total magnetic moment and local moment on tungsten are given. The total energies of these clusters were used to calculate the adiabatic detachment energy.

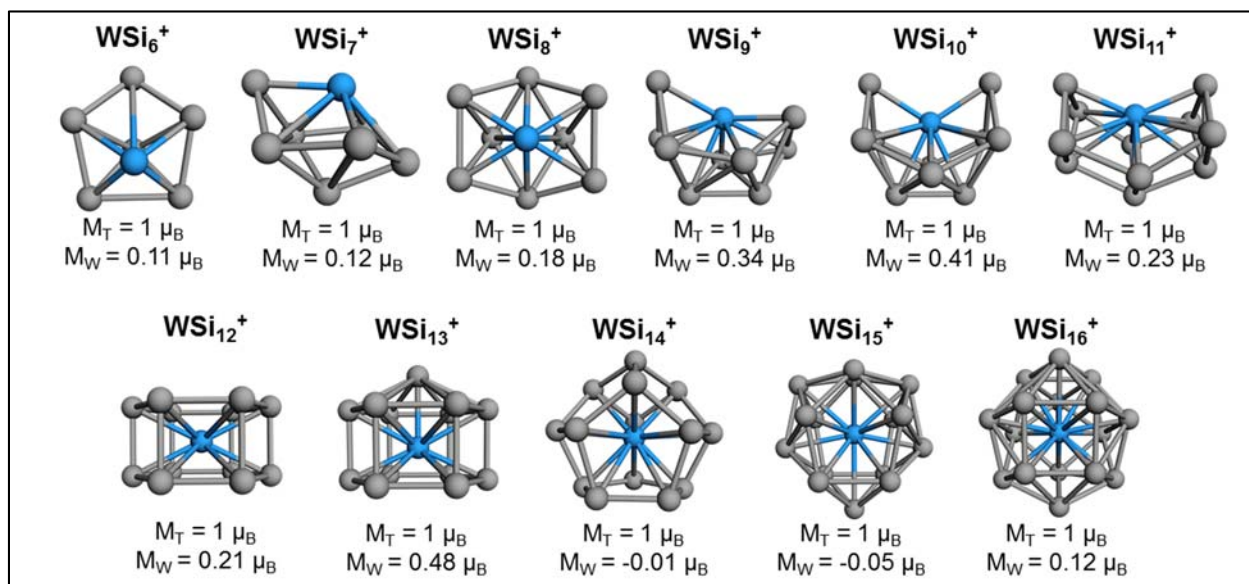


**Figure B-18: Ground State Structures of WSi<sub>n</sub> (n=6-16) Cations.** The lowest-energy structures of WSi<sub>n</sub><sup>+</sup> are shown with silicon in gray and tungsten in blue. The total magnetic moment and local moment on tungsten are given. The energies of these structures were used to calculate the ionization potential for each neutral cluster.

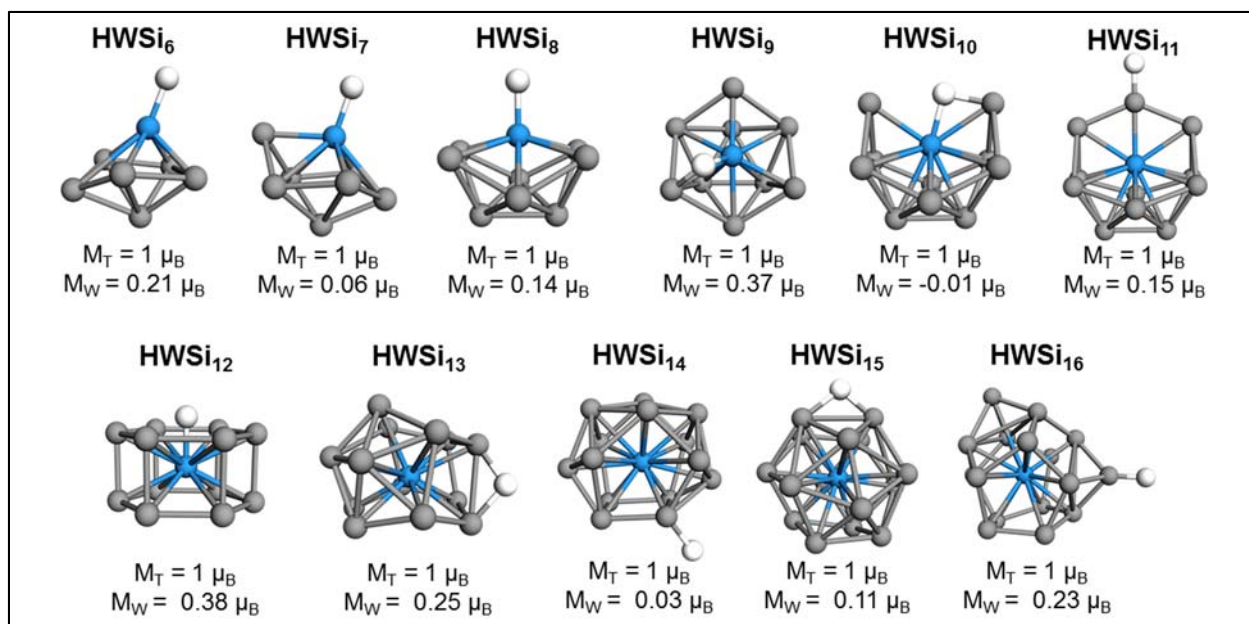


**Figure B-19: Lowest-Energy Hydrogen-Bound  $WSi_n$  ( $n=6-16$ ) Clusters.** The lowest-energy structures of hydrogen-bound  $WSi_n$  clusters are shown about with silicon in gray, tungsten in blue, and hydrogen in white. The total magnetic moment and local moment on tungsten are given for each cluster. The total energies of these structures were used in the calculations of the hydrogen binding energy.

**Table B-2: Calculated Properties of  $WSi_n$  ( $n=6-16$ ).**

# Si Atoms	$\Delta Si$	$\Delta W$	ADE	VDE	IP	HOMO-LUMO	H BE
6		5.40	2.17	2.49	7.30	1.29	2.54
7	4.77	5.71	2.28	2.31	7.24	1.43	2.61
8	4.14	6.79	2.39	2.44	6.99	0.98	2.78
9	4.00	6.37	2.87	3.17	7.13	0.96	2.64
10	4.45	6.11	3.00	3.03	7.12	0.89	2.56
11	4.87	7.85	2.78	2.97	7.41	1.54	2.02
12	4.72	8.46	2.50	2.50	7.40	1.41	1.83
13	3.75	8.69	3.16	3.38	6.63	0.81	2.45
14	5.32	9.61	2.65	2.95	7.42	1.82	1.77
15	4.55	9.72	2.56	2.84	7.07	1.71	1.82
16	3.76	10.53	2.62	2.74	6.61	1.21	2.19

The above table gives the numerical values used to generate the graphs in Figure 4.5.2, including the HOMO-LUMO gap, silicon binding energy, tungsten embedding energy, vertical and adiabatic detachment energies, ionization potential, and hydrogen binding energy. All values are given in eV.

## References

1. Rao, B. K. & Jena, P. Evolution of the electronic structure and properties of neutral and charged aluminum clusters: A comprehensive analysis. *J. Chem. Phys.* **111**, 1890 (1999).
2. Reddy, B. V., Khanna, S. N. & Dunlap, B. I. Giant magnetic moments in 4d clusters. *Phys. Rev. Lett.* **70**, 3323–3326 (1993).
3. Cox, A. J., Louderback, J. G. & Bloomfield, L. A. Experimental observation of magnetism in rhodium clusters. *Phys. Rev. Lett.* **71**, 923–926 (1993).
4. Pederson, M. R., Reuse, F. & Khanna, S. N. Magnetic transition in  $Mn_n$  ( $n=2-8$ ) clusters. *Phys. Rev. B* **58**, 5632–5636 (1998).
5. Nayak, S. . & Jena, P. Anomalous magnetism in small Mn clusters. *Chem. Phys. Lett.* **289**, 473–479 (1998).
6. Sanchez, A. *et al.* When Gold Is Not Noble: Nanoscale Gold Catalysts. *J. Phys. Chem. A* **103**, 9573–9578 (1999).
7. Leuchtner, R. E., Harms, A. C. & Castleman, A. W. Thermal Metal Cluster Anion Reactions - Behavior of Aluminum Clusters with Oxygen. *J. Chem. Phys.* **91**, 2753–2754 (1989).
8. Leuchtner, R. E., Harms, A. C. & Castleman, A. W. Aluminum cluster reactions. *J. Chem. Phys.* **94**, 1093 (1991).
9. Reber, A. C., Khanna, S. N., Roach, P. J., Woodward, W. H. & Castleman, A. W. Spin Accommodation and Reactivity of Aluminum Based Clusters with O<sub>2</sub>. *J. Am. Chem. Soc.* **129**, 16098–16101 (2007).
10. Khanna, S.N. & Castleman, A.W. *Quantum phenomena in clusters and nanostructures*. (Springer, 2003).

11. Alonso, J. A. *Structure And Properties Of Atomic Nanoclusters*. (World Scientific Publishing Company, 2005).
12. Billas, I. M. L., Châtelain, A. & de Heer, W. A. Magnetism from the Atom to the Bulk in Iron, Cobalt, and Nickel Clusters. *Science* **265**, 1682–1684 (1994).
13. Castleman, A. W. & Khanna, S. N. "Superatoms: building blocks of new materials." *The Chemical Physics of Solid Surfaces* **12**, 409-425 (Elsevier, 2007).
14. Sattler, K. *Cluster Assembled Materials*. (CRC Press, 1996).
15. P. Jena. *Clusters And Nano-assemblies Physical And Biological Systems*. (World Scientific Publishing Company, 2005).
16. Khanna, S. N. & Jena, P. Assembling crystals from clusters. *Phys. Rev. Lett.* **69**, 1664–1667 (1992).
17. Khanna, S. N. & Jena, P. Atomic clusters: Building blocks for a class of solids. *Phys. Rev. B* **51**, 13705–13716 (1995).
18. H.W. Kroto, J.R. Heath, S.C. O'Brien, R.F. Curl & R.E. Smalley. C<sub>60</sub>: Buckminsterfullerene. *Nature* **318**, 162–163 (1985).
19. Kroto, H. The Stability of the Fullerenes C<sub>n</sub> with n = 24, 28, 32, 36, 50, 60 and 70. *Nature* **329**, 529–531 (1987).
20. Hebard, A. F. *et al.* Superconductivity at 18 K in potassium-doped C<sub>60</sub>. *Nature* **350**, 600–601 (1991).
21. Yamanaka, S., Hotehama, K. & Kawaji, H. Superconductivity at 25.5 K in electron-doped layered hafnium nitride. *Nature* **392**, 580–582 (1998).
22. Claridge, S. A. *et al.* Cluster-Assembled Materials. *ACS Nano* **3**, 244–255 (2009).

23. Bühl, M. & Hirsch, A. Spherical Aromaticity of Fullerenes. *Chem. Rev.* **101**, 1153–1184 (2001).
24. Bolskar, R. D. Gadofullerene MRI contrast agents. *Nanomed.* **3**, 201–213 (2008).
25. Khanna, S. N. & Jena, P. Designing ionic solids from metallic clusters. *Chem. Phys. Lett.* **219**, 479–483 (1994).
26. Liu, F., Mostoller, M., Kaplan, T., Khanna, S. N. & Jena, P. Evidence for a new class of solids. First-principles study of  $K(Al_{13})$ . *Chem. Phys. Lett.* **248**, 213–217 (1996).
27. Ashman, C. *et al.*  $(Ba_{12})Cs$ : a cluster-assembled solid. *Phys. Rev. B* **55**, 15868–15873 (1997).
28. Khanna, S. N., Rao, B. K. & Jena, P. Electronic signature of the magicity and ionic bonding in  $Al_{13}X$  ( $X=Li-K$ ) clusters. *Phys. Rev. B* **65**, 125105 (2002).
29. Rao, B. K., Khanna, S. N. & Jena, P. Isomers of  $Al_{13}$  clusters and their interaction with alkali atoms. *Phys. Rev. B* **62**, 4666–4671 (2000).
30. Gutsev, G. L., Khanna, S. N. & Jena, P. Unambiguous assignment of the ground state of a nearly degenerate cluster. *Phys. Rev. B* **62**, 1604–1606 (2000).
31. Reber, A. C., Khanna, S. N. & Castleman, A. W. Superatom Compounds, Clusters, and Assemblies: Ultra Alkali Motifs and Architectures. *J. Am. Chem. Soc.* **129**, 10189–10194 (2007).
32. Mandal, S. *et al.*  $[As_7M(CO)_3]_3^-$   $M = Cr, Mo, W$ : Bonding and Electronic Structure of Cluster Assemblies with Metal Carbonyls. *J. Phys. Chem. C* **115**, 23704–23710 (2011).
33. Reber, A. C., Ugrinov, A., Sen, A., Qian, M. & Khanna, S. N. Helical and linear  $[K(As_{11})]_2^-$  chains: Role of solvent on the conformation of chains formed by Zintl anions. *Chem. Phys. Lett.* **473**, 305–311 (2009).

34. Castleman, A. W. & Khanna, S. N. Clusters, Superatoms, and Building Blocks of New Materials. *J. Phys. Chem. C* **113**, 2664–2675 (2009).
35. Häkkinen, H. & Manninen, M. How ‘Magic’ is a Magic Metal Cluster? *Phys. Rev. Lett.* **76**, 1599–1602 (1996).
36. Roach, P. J., Woodward, W. H., Castleman, A. W., Reber, A. C. & Khanna, S. N. Complementary Active Sites Cause Size-Selective Reactivity of Aluminum Cluster Anions with Water. *Science* **323**, 492–495 (2009).
37. Reber, A. C., Khanna, S. N., Roach, P. J., Woodward, W. H. & Castleman, A. W. Reactivity of Aluminum Cluster Anions with Water: Origins of Reactivity and Mechanisms for H<sub>2</sub> Release. *J. Phys. Chem. A* **114**, 6071–6081 (2010).
38. Reber, A. C., Roach, P. J., Woodward, W. H., Khanna, S. N. & Castleman, A. W. Edge-Induced Active Sites Enhance the Reactivity of Large Aluminum Cluster Anions with Alcohols. *J. Phys. Chem. A* **116**, 8085–8091 (2012).
39. Bergeron, D. E., Castleman, A. W., Morisato, T. & Khanna, S. N. Formation of Al<sub>13</sub>I<sup>-</sup>: Evidence for the Superhalogen Character of Al<sub>13</sub>. *Science* **304**, 84–87 (2004).
40. Bergeron, D. E., Roach, P. J., Castleman, A. W., Jones, N. O. & Khanna, S. N. Al Cluster Superatoms as Halogens in Polyhalides and as Alkaline Earths in Iodide Salts. *Science* **307**, 231–235 (2005).
41. Knight, W. D. *et al.* Electronic shell structure and abundances of sodium clusters. *Phys. Rev. Lett.* **52**, 2141–2143 (1984).
42. Ekardt, W. Work function of small metal particles: Self-consistent spherical jellium-background model. *Phys. Rev. B* **29**, 1558–1564 (1984).

43. Knight, W. D. *et al.* Alkali metal clusters and the jellium model. *Chem. Phys. Lett.* **134**, 1–5 (1987).
44. Jahn, H. A. & Teller, E. Stability of Polyatomic Molecules in Degenerate Electronic States. I. Orbital Degeneracy. *Proc. R. Soc. Lond. Ser. Math. Phys. Sci. 1934-1990* **161**, 220–235 (1937).
45. Clemenger, K. Ellipsoidal shell structure in free-electron metal clusters. *Phys. Rev. B* **32**, 1359–1362 (1985).
46. Nilsson, S. G. *Kgl Dan. Videnske Vidensk. Selsk. Mat Fys Medd* **29**, (1955).
47. De Heer, W. A. The physics of simple metal clusters: experimental aspects and simple models. *Rev. Mod. Phys.* **65**, 611–676 (1993).
48. Knight, W. D., de Heer, W. A., Clemenger, K. & Saunders, W. A. Electronic shell structure in potassium clusters. *Solid State Commun.* **53**, 445–446 (1985).
49. Katakuse, I. *et al.* Mass distributions of negative cluster ions of copper, silver, and gold. *Int. J. Mass Spectrom. Ion Process.* **74**, 33–41 (1986).
50. Zheng, W.-J., Thomas, O. C., Lippa, T. P., Xu, S.-J. & Bowen, K. H. The ionic  $\text{KAl}_{13}$  molecule: A stepping stone to cluster-assembled materials. *J. Chem. Phys.* **124**, 144304 (2006).
51. Jones, N. O. *et al.* Structural, electronic, and chemical properties of multiply iodized aluminum clusters. *J. Chem. Phys.* **124**, 154311 (2006).
52. Reveles, J. U., Khanna, S. N., Roach, P. J. & Castleman, A. W. Multiple valence superatoms. *Proc. Natl. Acad. Sci.* **103**, 18405–18410 (2006).
53. Shichibu, Y. *et al.* Biicosahedral Gold Clusters  $[\text{Au}_{25}(\text{PPh}_3)_{10}(\text{SC}_n\text{H}_{2n+1})_5\text{Cl}_2]^{2+}$  ( $n = 2-18$ ): A Stepping Stone to Cluster-Assembled Materials. *J. Phys. Chem. C* **111**, 7845–7847 (2007).



54. Jadzinsky, P. D., Calero, G., Ackerson, C. J., Bushnell, D. A. & Kornberg, R. D. Structure of a Thiol Monolayer-Protected Gold Nanoparticle at 1.1 Å Resolution. *Science* **318**, 430–433 (2007).
55. Heaven, M. W., Dass, A., White, P. S., Holt, K. M. & Murray, R. W. Crystal Structure of the Gold Nanoparticle  $[N(C_8H_{17})_4][Au_{25}(SCH_2CH_2Ph)_{18}]$ . *J. Am. Chem. Soc.* **130**, 3754–3755 (2008).
56. Zhu, M., Aikens, C. M., Hollander, F. J., Schatz, G. C. & Jin, R. Correlating the Crystal Structure of A Thiol-Protected  $Au_{25}$  Cluster and Optical Properties. *J. Am. Chem. Soc.* **130**, 5883–5885 (2008).
57. Lopez-Acevedo, O., Tsunoyama, H., Tsukuda, T., Hannu Häkkinen & Aikens, C. M. Chirality and Electronic Structure of the Thiolate-Protected  $Au_{38}$  Nanocluster. *J. Am. Chem. Soc.* **132**, 8210–8218 (2010).
58. Moreno, M., Ibañez, F. J., Jasinski, J. B. & Zamborini, F. P. Hydrogen Reactivity of Palladium Nanoparticles Coated with Mixed Monolayers of Alkyl Thiols and Alkyl Amines for Sensing and Catalysis Applications. *J. Am. Chem. Soc.* **133**, 4389–4397 (2011).
59. Nimmala, P. R. & Dass, A.  $Au_{36}(SPh)_{23}$  Nanomolecules. *J. Am. Chem. Soc.* **133**, 9175–9177 (2011).
60. Walter, M. *et al.* A unified view of ligand-protected gold clusters as superatom complexes. *Proc. Natl. Acad. Sci.* **105**, 9157–9162 (2008).
61. Akola, J. *et al.* Thiolate-Protected  $Au_{25}$  Superatoms as Building Blocks: Dimers and Crystals. *J. Phys. Chem. C* **114**, 15986–15994 (2010).

62. Briant, C. E. *et al.* Synthesis and X-ray structural characterization of the centred icosahedral gold cluster compound  $[\text{Au}_{13}(\text{PMe}_2\text{Ph})_{10}\text{Cl}_2](\text{PF}_6)_3$ ; the realization of a theoretical prediction. *J. Chem. Soc. Chem. Commun.* 201–202 (1981).
63. Pettibone, J. M. & Hudgens, J. W. Synthetic Approach for Tunable, Size-Selective Formation of Monodisperse, Diphosphine-Protected Gold Nanoclusters. *J. Phys. Chem. Lett.* **1**, 2536–2540 (2010).
64. Shafai, G., Hong, S., Bertino, M. & Rahman, T. S. Effect of Ligands on the Geometric and Electronic Structure of  $\text{Au}_{13}$  Clusters. *J. Phys. Chem. C* **113**, 12072–12078 (2009).
65. Bergeron, D. E., Jr, A. W. C., Morisato, T. & Khanna, S. N. Formation and properties of halogenated aluminum clusters. *J. Chem. Phys.* **121**, 10456–10466 (2004).
66. Jiang, D. & Walter, M. The halogen analogs of thiolated gold nanoclusters. *Nanoscale* **4**, 4234–4239 (2012).
67. Woodward, W. H., Reber, A. C., Smith, J. C., Khanna, S. N. & Castleman, A. W. Carbonyl Bond Cleavage by Complementary Active Sites. *J. Phys. Chem. C* **117**, 7445–7450 (2013).
68. Kumar, V. *Nanosilicon*, 114–148 (Elsevier, 2008).
69. Beck, S. M. Studies of silicon cluster–metal atom compound formation in a supersonic molecular beam. *J. Chem. Phys.* **87**, 4233–4234 (1987).
70. Beck, S. M. Mixed metal–silicon clusters formed by chemical reaction in a supersonic molecular beam: Implications for reactions at the metal/silicon interface. *J. Chem. Phys.* **90**, 6306–6312 (1989).
71. Kumar, V. & Kawazoe, Y. Metal-Encapsulated Fullerenelike and Cubic Caged Clusters of Silicon. *Phys. Rev. Lett.* **87**, (2001).

72. Kumar, V. & Kawazoe, Y. Magic behavior of  $\text{Si}_{15}\text{M}$  and  $\text{Si}_{16}\text{M}$  (M=Cr, Mo, and W) clusters. *Phys. Rev. B* **65**, (2002).
73. Kawamura, H., Kumar, V. & Kawazoe, Y. Growth behavior of metal-doped silicon clusters  $\text{Si}_n\text{M}$  (M=Ti,Zr,Hf;n=8–16). *Phys. Rev. B* **71**, (2005).
74. Sun, Z., Oyanagi, H., Uchida, N., Miyazaki, T. & Kanayama, T. Structure determination of W-capsulated Si cage clusters by x-ray absorption fine structure spectra. *J. Phys. -Appl. Phys.* **42**, 015412 (2009).
75. Janssens, E. *et al.* Argon Physisorption as Structural Probe for Endohedrally Doped Silicon Clusters. *Phys. Rev. Lett.* **99**, 063401 (2007).
76. Hiura, H., Miyazaki, T. & Kanayama, T. Formation of Metal-Encapsulating Si Cage Clusters. *Phys. Rev. Lett.* **86**, 1733–1736 (2001).
77. Miyazaki, T., Hiura, H. & Kanayama, T. Topology and energetics of metal-encapsulating Si fullerene-like cage clusters. *Phys. Rev. B* **66**, 121403 (2002).
78. Pandey, R., Rao, B. K., Jena, P. & Blanco, M. A. Electronic Structure and Properties of Transition Metal–Benzene Complexes. *J. Am. Chem. Soc.* **123**, 7744–7744 (2001).
79. Khanna, S., Rao, B. & Jena, P. Magic Numbers in Metallo-Inorganic Clusters: Chromium Encapsulated in Silicon Cages. *Phys. Rev. Lett.* **89**, (2002).
80. Zheng, W., Nilles, J. M., Radisic, D. & Bowen, K. H. Photoelectron spectroscopy of chromium-doped silicon cluster anions. *J. Chem. Phys.* **122**, 071101–071101–4 (2005).
81. Sen, P. & Mitas, L. Electronic structure and ground states of transition metals encapsulated in a  $\text{Si}_{12}$  hexagonal prism cage. *Phys. Rev. B* **68**, 155404 (2003).
82. Ulises Reveles, J. & Khanna, S. Nearly-free-electron gas in a silicon cage. *Phys. Rev. B* **72**, (2005).

83. He, J., Wu, K., Liu, C. & Sa, R. Stabilities of 3d transition-metal doped Si<sub>14</sub> clusters. *Chem. Phys. Lett.* **483**, 30–34 (2009).
84. Guo, L., Zhao, G., Gu, Y., Liu, X. & Zeng, Z. Density-functional investigation of metal-silicon cage clusters MSi<sub>n</sub> (M = Sc, Ti, V, Cr, Mn, Fe, Co, Ni, Cu, Zn; n=8-16). *Phys. Rev. B* **77**, (2008).
85. Atkins, Peter *et al.* *Inorganic Chemistry*. (W.H. Freeman and Company, 2006).
86. Jensen, W. B. The Origin of the 18-Electron Rule. *J. Chem. Educ.* **82**, 28 (2005).
87. Pyykkö, P. Understanding the eighteen-electron rule. *J. Organomet. Chem.* **691**, 4336–4340 (2006).
88. Khanna, S. N., Rao, B. K., Jena, P. & Nayak, S. K. Stability and magnetic properties of iron atoms encapsulated in Si clusters. *Chem. Phys. Lett.* **373**, 433–438 (2003).
89. Kawamura, H., Kumar, V. & Kawazoe, Y. Growth, magic behavior, and electronic and vibrational properties of Cr-doped Si clusters. *Phys. Rev. B* **70**, (2004).
90. Ulises Reveles, J. & Khanna, S. N. Electronic counting rules for the stability of metal-silicon clusters. *Phys. Rev. B* **74**, 035435 (2006).
91. Uchida, N., Miyazaki, T. & Kanayama, T. Stabilization mechanism of Si<sub>12</sub> cage clusters by encapsulation of a transition-metal atom: A density-functional theory study. *Phys. Rev. B* **74**, 205427 (2006).
92. Koyasu, K., Akutsu, M., Mitsui, M. & Nakajima, A. Selective Formation of MSi<sub>16</sub> (M = Sc, Ti, and V). *J. Am. Chem. Soc.* **127**, 4998–4999 (2005).
93. Bowser, J. R. *Inorganic Chemistry*. (Brooks/Cole, 1993).

94. Roach, P. J., Woodward, W. H., Reber, A. C., Khanna, S. N. & Castleman, A. W. Crystal field effects on the reactivity of aluminum-copper cluster anions. *Phys. Rev. B* **81**, 195404 (2010).
95. Luo, Z. *et al.* Spin Accommodation and Reactivity of Silver Clusters with Oxygen: The Enhanced Stability of  $\text{Ag}_{13}^-$ . *J. Am. Chem. Soc.* **134**, 18973–18978 (2012).
96. Luo, Z., Grover, C. J., Reber, A. C., Khanna, S. N. & Castleman, A. W. Probing the Magic Numbers of Aluminum–Magnesium Cluster Anions and Their Reactivity toward Oxygen. *J. Am. Chem. Soc.* **135**, 4307–4313 (2013).
97. Born, M. & Oppenheimer, R. Zur quantentheorie der molekeln. *Ann. Phys.* **389**, 457–484 (1927).
98. Koch, W. & Holthausen, M. C. *A Chemist's Guide to Density Functional Theory*. (Wiley-VCH, 2001).
99. Hohenberg, P. & Kohn, W. Inhomogeneous electron gas. *Phys. Rev.* **136**, B864 (1964).
100. Kohn, W. & Sham, L. Self-Consistent Equations Including Exchange and Correlation Effects. *Phys. Rev.* **140**, 1133–& (1965).
101. Perdew, J. P., Burke, K. & Ernzerhof, M. Generalized gradient approximation made simple. *Phys. Rev. Lett.* **77**, 3865 (1996).
102. Perdew, J. P., Burke, K. & Ernzerhof, M. Generalized Gradient Approximation Made Simple [Phys. Rev. Lett. 77, 3865 (1996)]. *Phys. Rev. Lett.* **78**, 1396–1396 (1997).
103. Becke, A. D. A new mixing of Hartree–Fock and local density-functional theories. *J. Chem. Phys.* **98**, 1372 (1993).
104. Becke, A. D. Density-functional thermochemistry. III. The role of exact exchange. *J. Chem. Phys.* **98**, 5648 (1993).

105. Jackson, K. & Pederson, M. R. Accurate forces in a local-orbital approach to the local-density approximation. *Phys. Rev. B* **42**, 3276–3281 (1990).
106. Pederson, M. R. & Jackson, K. A. Variational mesh for quantum-mechanical simulations. *Phys. Rev. B* **41**, 7453–7461 (1990).
107. Porezag, D. & Pederson, M. R. Optimization of Gaussian basis sets for density-functional calculations. *Phys. Rev. A* **60**, 2840–2847 (1999).
108. Guerra, C. F., Snijders, J. G., Te Velde, G. & Baerends, E. J. Towards an order-N DFT method. *Theor. Chem. Acc.* **99**, 391–403 (1998).
109. Te Velde, G. *et al.* Chemistry with ADF. *J. Comput. Chem.* **22**, 931–967 (2001).
110. *ADF2013*. (SCM, Theoretical Chemistry). at <<http://www.scm.com>>
111. Stephens, P. J., Devlin, F. J., Chabalowski, C. F. & Frisch, M. J. Ab Initio Calculation of Vibrational Absorption and Circular Dichroism Spectra Using Density Functional Force Fields. *J. Phys. Chem.* **98**, 11623–11627 (1994).
112. Van Gisbergen, S. J. A., Snijders, J. G. & Baerends, E. J. Implementation of time-dependent density functional response equations. *Comput. Phys. Commun.* **118**, 119–138 (1999).
113. Rosa, A. *et al.* Electronic Spectra of M(CO)<sub>6</sub> (M = Cr, Mo, W) Revisited by a Relativistic TDDFT Approach. *J. Am. Chem. Soc.* **121**, 10356–10365 (1999).
114. Hirata, S. & Head-Gordon, M. Time-dependent density functional theory within the Tamm–Dancoff approximation. *Chem. Phys. Lett.* **314**, 291–299 (1999).
115. Abreu, M. B., Powell, C., Reber, A. C. & Khanna, S. N. Ligand-Induced Active Sites: Reactivity of Iodine-Protected Aluminum Superatoms with Methanol. *J. Am. Chem. Soc.* **134**, 20507–20512 (2012).

116. Abreu, M. B., Reber, A. C. & Khanna, S. N. Does the 18-Electron Rule Apply to CrSi<sub>12</sub>? *J. Phys. Chem. Lett.* **5**, 3492–3496 (2014).
117. Hagelberg, F., Xiao, C. & Lester, W. Cagelike Si<sub>12</sub> clusters with endohedral Cu, Mo, and W metal atom impurities. *Phys. Rev. B* **67**, (2003).
118. Lu, J. & Nagase, S. Structural and Electronic Properties of Metal-Encapsulated Silicon Clusters in a Large Size Range. *Phys. Rev. Lett.* **90**, (2003).
119. Kong, X., Xu, H.-G. & Zheng, W. Structures and magnetic properties of CrSi<sub>n</sub><sup>-</sup> (n = 3–12) clusters: Photoelectron spectroscopy and density functional calculations. *J. Chem. Phys.* **137**, 064307 (2012).
120. Li, J. *et al.* Structures and magnetic properties of Si<sub>n</sub>Mn (n = 1–15) clusters. *J. Chem. Phys.* **130**, 164514–164514–9 (2009).
121. Ho, K.-M. *et al.* Structures of medium-sized silicon clusters. *Nature* **392**, 582–585 (1998).
122. Rohlffing, C. M. & Raghavachari, K. A theoretical study of small silicon clusters using an effective core potential. *Chem. Phys. Lett.* **167**, 559–565 (1990).
123. Raghavachari, K. & McMichael Rohlffing, C. Electronic structures of the negative ions Si<sub>2</sub><sup>-</sup>–Si<sub>10</sub><sup>-</sup>: Electron affinities of small silicon clusters. *J. Chem. Phys.* **94**, 3670–3678 (1991).
124. Belkhir, M. A., Mahtout, S., Belabbas, I. & Samah, M. Structure and electronic property of medium-sized silicon clusters. *Phys. E Low-Dimens. Syst. Nanostructures* **31**, 86–92 (2006).
125. Nigam, S., Majumder, C. & Kulshreshtha, S. K. Structural and electronic properties of Si<sub>n</sub>, Si<sub>n</sub><sup>+</sup>, and AlSi<sub>n-1</sub> (n=2–13) clusters: Theoretical investigation based on ab initio molecular orbital theory. *J. Chem. Phys.* **121**, 7756 (2004).

126. Iwamatsu, M. Global geometry optimization of silicon clusters using the space-fixed genetic algorithm. *J. Chem. Phys.* **112**, 10976 (2000).
127. Pedicini, A. F., Reber, A. C. & Khanna, S. N. The effect of sulfur covalent bonding on the electronic shells of silver clusters. *J. Chem. Phys.* **139**, 164317 (2013).
128. Gamboa, G. U., Reber, A. C. & Khanna, S. N. Electronic subshell splitting controls the atomic structure of charged and neutral silver clusters. *New J. Chem.* **37**, 3928–3935 (2013).